William & Mary
CHARTERED 1693

W&M ScholarWorks

Dissertations, Theses, and Masters Projects

Theses, Dissertations, & Master Projects

2006

Optical characterization of ferromagnetic heterostructure *interfaces and thin films

Haibin Zhao
College of William & Mary - Arts & Sciences

Follow this and additional works at: https://scholarworks.wm.edu/etd

Part of the Condensed Matter Physics Commons, Electromagnetics and Photonics Commons, and the Optics Commons

Recommended Citation

Zhao, Haibin, "Optical characterization of ferromagnetic heterostructure *interfaces and thin films" (2006). *Dissertations, Theses, and Masters Projects.* Paper 1539623494.
https://dx.doi.org/doi:10.21220/s2-fe5w-vy69

This Dissertation is brought to you for free and open access by the Theses, Dissertations, & Master Projects at W&M ScholarWorks. It has been accepted for inclusion in Dissertations, Theses, and Masters Projects by an authorized administrator of W&M ScholarWorks. For more information, please contact scholarworks@wm.edu.

OPTICAL CHARACTERIZATION OF FERROMAGNETIC HETEROSTRUCTURE INTERFACES AND THIN FILMS

A Dissertation

Presented to

The Faculty of the Department of Applied Science

The College of William and Mary in Virginia

In Partial Fulfillment

Of the Requirements for the Degree of

Doctor of Philosophy

By

Haibin Zhao

February 2006

Reproduced with permission of the copyright owner. Further reproduction prohibited without permission.

APPROVAL SHEET

This dissertation is submitted in partial fulfillment of
the requirements for the degree of

Doctor of Philosophy

Haibin Zhao

Approved by the Committee, February 2006

Gunter Lüpke, Chair

Robert L. Vold

William J. Kossler

Anne C. Reilly

Reproduced with permission of the copyright owner. Further reproduction prohibited without permission.

TABLE OF CONTENTS

Page

Acknowledgements vi

List of Tables vii

List of Figures viii

Abstract xiii

1 Introduction 2

1.1 Semiconductor-based magnetoelectronics 2

1.2 Spin injection 7

1.3 Spin transport across interface 10

1.4 Magnetization switching and dynamics 12

1.5 Scope of this dissertation 13

2 Experimental techniques 16

2.1 Magneto-optical Kerr effect (MOKE) 16

2.2 Magnetization induced second harmonic generation (MSHG) 20

2.2.1 Nonlinear magnetic susceptibility 20

2.2.2 Experimental considerations 25

2.3 Time-resolved MOKE and MSHG spectroscopy 31

2.3.1 Laser induced magnetization precession 31

2.3.2 Experimental setup 35

Reproduced with permission of the copyright owner. Further reproduction prohibited without permission.

2.4 Internal Photo-emission (IPE) 38

3 Interface magnetization reversal and magnetic anisotropy in Fe/AlGaAs 42

3.1 Introduction 42

3.2 Interface magnetization reversal and magnetic anisotropy in Fe/AlGaAs (001) .. 44

3.3 Interface magnetization reversal and magnetic anisotropy in Fe/AlGaAs (110) .. 52

3.4 Interface magnetization reversal in Fe/AlO/AlGaAs 56

4 Time-resolved studies of spin precession in Fe/AlGaAs (001) 59

4.1 Introduction 59

4.2 Interface magnetization precession 61

4.3 Bulk magnetization precession 69

4.3.1 Uniform magnetization precession in 10-nm Fe (001) film 69

4.3.2 Spin wave excitation in 50-nm Fe (001) film 75

5 Time-resolved spin precession in manganite films 82

5.1 Introduction 82

5.2 Magnetization precession and magnetic anisotropy in LCMO films 87

5.2.1 Strained LCMO/STO heterostructure 89

5.2.2 Strain free LCMO/NGO heterostucture 92

5.3 Magnetization precession and magnetic anisotropy in LSMO films 98

6 Band-Offsets at $CdCr_2Se_4$-(AlGa)As and $CdCr_2Se_4$-ZnSe Interfaces 104

6.1 Introduction 104

6.2 Crystallographic, electronic and magnetic structure of $CdCr_2Se_4$ 106

6.3 Sample preparation 108

6.4 Band offsets at $CdCr_2Se_4$–(AlGa)As and $CdCr_2Se_4$–ZnSe interfaces 110

Reproduced with permission of the copyright owner. Further reproduction prohibited without permission.

7 Conclusions **115**

Bibliography **118**

Vita **127**

Reproduced with permission of the copyright owner. Further reproduction prohibited without permission.

ACKNOWLEDGEMENTS

I am truly grateful to everyone who has directly or indirectly supported and helped me complete this dissertation. First and foremost, I would like to thank my advisor, Professor Gunter Lüpke, for his encouragement, advice and mentoring throughout my doctoral studies at the College of William and Mary. This dissertation would not have been possible without his support and guidance.

Special appreciation goes to Dr. Berend Jonker and his group members – Aubrey Hanbicki and Connie Li *et al* at Naval Research Laboratory in Washington, DC. I am deeply indebted to them for providing us state-of-art devices and high quality samples. I also benefited greatly from their inspired visions and suggestions.

I owe special thank to Prof. Qi Li and her group members from Pennsylvania State University for providing us high quality manganite films. I truly appreciate Prof. Anne Reilly and her group members for supporting me at labs.

My sincere gratefulness goes to my lab mates: Yuhang Ren, Shuyan Zhang, Baozhou Sun, Diyar Talbayev, Andrea Lucarelli, Hailong Huang and Keoki Seu. I appreciate all their friendships and their collective encouragement to finish this dissertation. I have enjoyed every moment that we have worked together. In particular, I would like to thank Shuyan Zhang and Yuhang Ren for teaching me many things about life.

I would also like to express my appreciation to my doctoral dissertation committee members: Dr. Robert Vold of Applied Science, Dr. William Kossler and Dr. Anne Reilly of Physics for their comments and suggestions during the course of completing this dissertation.

I must thank Eddie and Grace for their love and help during my stay in Williamsburg. I enjoy all the delicious food they cooked and appreciate their teaching about life.

Finally, I wish to express my gratitude to my parents – Fangxin Zhao, Aizhen Fang, and my sister – Cuiyu Zhao. Their constant love, encouragement and support have always been the source of my strength and motivation. Anything I have been able to accomplish is a tribute to them.

Reproduced with permission of the copyright owner. Further reproduction prohibited without permission.

LIST OF TABLES

Page

2.1 The Fresnel coefficients of p-polarized light incident on a magnetic film for the polar, longitudinal, and transverse MOKE. 19

2.2 MSHG susceptibility tensor elements in Fe/AlGaAs (001) structure. 22

2.3 MSHG susceptibility tensor elements in Fe/AlGaAs (110) structure. 24

2.4 Azimuthal amplitudes in the fits to the rotational MSHG intensity curves by Eq. (2.13) for Fe/AlGaAs (001). 30

4.1 Anisotropy field values deduced from fits to the field dependence of the precession frequency at the interface and in the bulk in Fe/AlGaAs(001). 64

5.1 Anisotropy field values deduced from fits to the field dependence of the precession frequency in the LCMO/STO film. 91

5.2 Anisotropy field values deduced from fits to the field dependence of the precession frequency in LCMO/NGO films. 100 nm* sample – measurements in Fig. 5.4. 60 nm, 100 nm, and 150 nm samples – measurements in Fig. 5.5. 95

5.3 Anisotropy field values deduced from fits to the field dependence of the precession frequency in LSMO films. 102

Reproduced with permission of the copyright owner. Further reproduction prohibited without permission.

LIST OF FIGURES

Page

1.1 A schematic representation of the density of electronic states that are available to electrons in a normal metal, and in a ferromagnetic metal whose majority spin states are completely filled. E denotes the electron energy; E_F is the Fermi level; N(E) denotes the density of states. 3

1.2 Spin-polarized field effect transistor scheme. V_g is the gate voltage. 6

2.1 Geometries of longitudinal, transverse, and polar Kerr effects. 18

2.2 Schematic MSHG experimental geometry: sample rotates azimuthally in the applied magnetic field in longitudinal magneto-optical configuration. The notations p and s denote the polarizations parallel and perpendicular to the incident plane of reflection, respectively. 25

2.3 Rotational SHG intensity curves from 10 nm Fe (001) film for different polarization combinations. The axis along 0° corresponds to the hard [1-10] direction in the bulk Fe. 26

2.4 Longitudinal nonlinear magneto-optical effect in a 10-nm Fe film on AlGaAs (001) for different analyzer angles. The incident light is s polarized, and SHG pass through the analyzer set at angle α with respect to the s-polarized direction. The experimental data are shown by circles and the best fits by Eq. (2.13) are shown by solid lines. 28

2.5 Asymmetry A as a function of the analyzer angle α for magnetization along [1-10] direction of Fe/AlGaAs (001) for s polarized incident light. Solid line is the best fit according to Eq. (2.12). 29

2.6 Precession of magnetization in the effective magnetic field. 32

2.7 Coordinate system used for calculating the magnetization precession frequency in a ferromagnetic thin film. 33

2.8 Sketch of the time-resolved MOKE setup. 35

2.9 Schematic diagram of transient MOKE signal detection in TRMOKE

Reproduced with permission of the copyright owner. Further reproduction prohibited without permission.

experiments. The top and bottom panels indicate the pulsed photocurrent from the detector and signal after gated integrator and boxcar averager. 36

2.10 Sketch of time-resolved MSHG setup. 37

2.11 Schematic of internal photoemission from a Fermi surface to a conduction band of a semiconductor. Φ is the energy barrier across the interface. 39

2.12 Experimental setup for band offset measurement of semiconductor heterostructures. 40

2.13 The OPA wavelengths vs BBO tuning position. 41

3.1 Interface structure for the As-terminated Fe/GaAs (001). 43

3.2 Longitudinal MSHG, (a) – (d), and MOKE, (e) – (h), *M-H* loops from 10-nm Fe (001) film with the field applied along the principal crystallographic axes [110], [1-10], [010], and [100], respectively. The squares (triangles) indicate increasing (decreasing) magnetic field. The coercive fields are listed in each panel. 46

3.3 (a) *M-H* loop for one-jump switching; (b) *M-H* loop for two-jump switching; and (c) sequence of the two-jump process. The numbers relate the steps in the sequence to the corresponding feature in the *M-H* loop. 47

3.4 Variation of in-plane magnetization orientation with distance from the interface according to Eq. (3.1). 50

3.5 Longitudinal MSHG, (a) and (b), and MOKE, (c) and (d), *M-H* loops from the 50-nm Fe film capped with a 5 nm Cr layer with the field applied along the hard-easy [110] and hard-hard [1-10] axes, respectively. The squares (triangles) indicate increasing (decreasing) magnetic field. 51

3.6 The in-plane anisotropy energy density at zero field according to Eq. (3.3) for Fe (110) films with different anisotropy ratio $r=K_u/K_1$. 54

3.7 Longitudinal MSHG and MOKE, *M-H* loops from 10-nm Fe (110) film with the field applied along the principal crystallographic axes [001], [1-10], [1-11], and [-111], respectively. The coercive fields are listed in each panel. 55

3.8 Longitudinal MSHG and MOKE *M-H* loops in Fe/Al_2O_3/AlGaAs (001) film with the field applied along the principal crystallographic axes [110], [1-10], [010], and [100], respectively. The squares (circles) indicate increasing (decreasing) magnetic field. The coercive fields are listed in each panel. 57

Reproduced with permission of the copyright owner. Further reproduction prohibited without permission.

4.1 (a) Time-resolved MSHG experimental configuration and (b) transient MSHG signal after laser excitation with a magnetic field H=560 Oe applied along [1-10] direction in a 10-nm Fe film on AlGaAs (001). The inset shows the Fourier transformation. (c) Interface precession frequency at different magnetic fields along [1-10] direction. 62

4.2 Interface and bulk precession frequency versus applied magnetic field in Fe/AlGaAs (001). The solid lines are the fits by Eq. (4.1). 64

4.3 (a) Interface *M-H* loop taken by static MSHG measurement. (b) Interface magnetization precession at H = 72 Oe. Black and red curves are taken with field sweeping up or down, respectively. Dashed blue curve shows bulk magnetization precession at 72 Oe with field sweeping up. (c) Bulk *M-H* loop taken by static MOKE measurement. (d) Bulk magnetization precessions at fields of 47 Oe, 72 Oe and 188 Oe. Black and red curves are taken with field sweeping up or down, respectively. 66

4.4 (a) TR-MOKE experimental configuration with longitudinal geometry, (b) Schematic diagram of the coherent excitation process of the uniform magnetization precession, (c) Transient Kerr signal and (d) Fourier transforms of (c) after picosecond excitation of a 10-nm thick epitaxial Fe film with magnetic field H = 560 Oe applied along [110], [100] and [1-10] directions. 70

4.5 (a) Precession amplitude; (b) frequency as a function of sample orientation at magnetic field H = 560 Oe in a 10-nm Fe film. The dashed line is a guide to the eye. 72

4.6 (a) Precession frequency versus applied magnetic field along [100] and [1-10] axes in a 10-nm Fe film. The solid line is a fit by Eq. (4.1) and (4.3). (b) Gilbert damping parameter α versus applied magnetic field along [100] and [1-10] directions. 74

4.7 (a) Transient Kerr signal after picosecond excitation of a 50-nm thick epitaxial Fe film with magnetic field applied along [110], (b) Fourier transforms of (a), and (c) precession frequency versus magnetic field. The solid lines are fits by Eq. (4.5). 76

4.8 (a) Transient Kerr signal after picosecond excitation of a 50-nm thick epitaxial Fe film with magnetic field of 560 Oe applied along different directions, and (b) precession frequency versus magnetic field. The solid lines are fit by Eq. (4.5). 80

5.1 Crystal structure of doped manganites: $LA_{1-x}RE_xMnO_3$. Each manganese atom is surrounded by six oxygen atoms to form a regular MnO_6 octahedron. The six oxygen atoms occupy the faces of a cube. Between the octahedral, at

Reproduced with permission of the copyright owner. Further reproduction prohibited without permission.

the corner of the cubes, lies a mixture of trivalent rare earth (LA) and divalent alkaline earth (RE) cations. 83

5.2 (a) Geometry of the pump-probe measurement with applied magnetic field. (b) Magnetization precession as measured by TR-MOKE in the 60-nm LCMO/NGO film at T = 20 K and $\delta = 45^{o}$. 88

5.3 Field dependence of precession frequency in LCMO/STO. Solid lines are calculated using the expressions given by Eq. (5.2), (5.3) and (5.4) with effective fields given in Table 5.1 and *g*-factor of 1.98. (a) Applied magnetic field is in plane. $\delta = 0^{o}$ and $\delta = 45^{o}$ orientations correspond to the field along the in-plane tetragonal easy-axis and along the in-plane tetragonal hard axis, respectively. δ is defined in Fig. 5.2. (b) Applied magnetic field is almost normal to the film and lies in the *Y-Z* plane, with *Y* being the tetragonal easy axis. 90

5.4 Field dependence of precession frequency in LCMO/NGO, in the 100 nm* sample in Table 5.2. Solid lines are calculated using the expressions given by Eq. (5.2), (5.6) and (5.7) with the effective fields given in Table 5.2 and *g*-factor of 1.98. (a) Applied magnetic field is in plane. The $\delta = 45^{o}$, $\delta = 90^{o}$, and $\delta = 135^{o}$ orientations correspond to the field along the in-plane uniaxial easy-axis, at 45° to the easy axis, and along the in-plane uniaxial hard axis, respectively. δ is defined in Fig. 5.2. (b) Applied magnetic field is almost normal to the film and lies in the *Y- Z* plane, with *Y* being the uniaxial easy axis. 93

5.5 Field dependence of precession frequency in LCMO/NGO, in the 60 nm, 100 nm, and 150 nm samples in Table 5.2. Solid lines are calculated using the expressions given in the Eq. (5.2) and (5.6) with effective fields given in Table 5.2 and *g*-factor of 1.98. Applied magnetic field is in plane. In each panel $\delta = 45^{o}$, $\delta = 90^{o}$, and $\delta = 135^{o}$ orientations correspond to the field along the in-plane uniaxial easy-axis, at 45° to the easy axis, and along the in-plane uniaxial hard axis, respectively. δ is defined in Fig. 5.2. 97

5.6 (a) Geometry of the pump-probe measurement in the applied magnetic field. (b) Magnetization precession as seen by TR-MOKE in LSMO/NGO at T=170K and B=0.5T. 98

5.7 Field dependence of precession frequency in LSMO/NGO for different temperatures. 99

5.8 Field dependence of precession frequency in LSMO films on different substrates: NGO (squares), STO (triangles), and LAO (diamonds). Solid lines are the fits to the corresponding data points. 101

6.1 Model of the crystal structure of bulk $CdCr_2Se_4$. Chromium atoms occupy

Reproduced with permission of the copyright owner. Further reproduction prohibited without permission.

octahedral sites defined by selenium ligands; one such octahedron is explicitly shown. 106

6.2 Energy gap of $CdCr_2Se_4$ versus temperature. Dashed line assumed extrapolation for paramagnetic state. 107

6.3 Theoretical densities of states (DOS) of bulk $CdCr_2Se_4$ calculated within LDA. The inset shows the density of states near the bandgap. Minority spin states dominate the conduction-band edge. 108

6.4 (a) IPE spectra at room temperature from unbiased ZnSe/GaAs heterojunctions. (b) The band alignment across the heterointerface. 109

6.5 IPE spectra at room temperature from unbiased heterojunctions: (a) $CdCr_2Se_4$/AlGaAs, and (b) $CdCr_2Se_4$/GaAs. The insets show the cross section of the LED and the band alignment. 111

6.6 (a) IPE spectrum from the unbiased $CdCr_2Se_4$/ZnSe heterojunction at room temperature. The inset shows the cross section of the LED. (b) QW luminescence spectrum at T=10 K. 113

Reproduced with permission of the copyright owner. Further reproduction prohibited without permission.

ABSTRACT

This thesis presents optical characterizations of interfaces in ferromagnetic heterostructures and thin films used for spin polarized electronic devices. In these experiments, femtosecond laser spectroscopies are exploited to investigate the interface magnetization reversal, spin precession, and band offset, which are crucial in determining the performances of spintronic devices.

First, magnetization-induced second-harmonic-generation (MSHG) is applied to study interface magnetism in a hybrid structure containing a noncentrosymmetric semiconductor - Fe/AlGaAs. The reversal process of Fe interface layer magnetization is compared with the bulk magnetization reversal. In Fe/AlGaAs (001), the interface magnetization is found to be decoupled from the bulk magnetization based on the different switching characteristics – single step switching occurs at the interface layer, whereas two-jump switching occurs in the bulk. In contrast, the interface layer in Fe/AlGaAs (110) is rigidly coupled with the bulk Fe, indicating a strong impact of electronic structure on the magnetic interaction despite the same chemical composition. Furthermore, a time-resolved MSHG study demonstrates a coherent interface magnetization precession in Fe/AlGaAs (001), implying the feasibility of fast precessional control of interfacial spin. The interface magnetization precession exhibits a higher frequency and opposite phase for a given applied field compared to the bulk magnetization precession.

Second, uniform magnetization precession in the $La_{0.67}Ca_{0.33}MnO_3$ (LCMO) and $La_{0.67}Sr_{0.33}MnO_3$ (LSMO) films grown on different substrates are investigated by time-resolved magneto-optic Kerr effect. The parameters of magnetic anisotropy are determined from the field dependence of the precession frequency. The strain-free LCMO films grown on $NdGaO_3$ exhibit a uniaxial in-plane anisotropy induced by the tilting of the oxygen octahedra in $NdGaO_3$. An easy-plane magnetic anisotropy is found in the tensile-strained films grown on $SrTiO_3$, whereas the compressive-strained film grown on $LaAlO_3$ exhibits an easy normal-to-plane axis.

Third, a table-top internal photoemission system is developed to measure the band offsets across semiconductor heterointerfaces by utilizing an optical parametric amplifier as the bright light source. The conduction band offsets ΔE_c = 660 meV and 530 meV at the $CdCr_2Se_4$-GaAs and $CdCr_2Se_4$-ZnSe interfaces are determined from the threshold energies of the photocurrent spectrum. The band offset is shown to be reduced by engineering the interface bonding and stoichiometry.

Reproduced with permission of the copyright owner. Further reproduction prohibited without permission.

OPTICAL CHARACTERIZATION OF FERROMAGNETIC HETEROSTRUCTURE INTERFACES AND THIN FILMS

Reproduced with permission of the copyright owner. Further reproduction prohibited without permission.

Chapter 1

Introduction

1.1 Semiconductor based magnetoelectronics

Electrons possess electric charge as well as intrinsic angular momentum (or spin). Until recently, however, the spin of the electron was ignored in mainstream charge-based semiconductor electronics. A new technology called spintronics (spin-based electronics) has recently emerged, where it is not the electron charge but the electron spin that carries information. Spintronics combines standard microelectronics with spin-dependent effects, promising access to new technologies such as quantum computation and quantum communication [1-3]. Advantages of spintronic devices compared with conventional electronics would be their nonvolatility, increased data processing speed, decreased electric power consumption, and increased integration densities.

The basic action in spin-polarized devices is based on spin-polarized transport, which will occur naturally in any material for which there is an imbalance of the spin populations at the Fermi level. This imbalance commonly occurs in ferromagnetic (FM) metals because the density of states distribution for spin-up and spin-down electrons is often nearly identical, but they are shifted in energy with respect to each other due to exchange splitting (Fig. 1.1). This shift results in an unequal filling of the bands, which is the source of the net magnetic moment for these materials, and it also causes the spin-up

Reproduced with permission of the copyright owner. Further reproduction prohibited without permission.

and spin-down carriers at the Fermi level to be unequal in number, character, and mobility. This inequality can produce a net spin polarization in carrier transport.

The first step on the road to utilization of the spin-dependent transport was the discovery of Giant Magnetoresistance (GMR) in 1988 [4]. GMR is observed in artificial thin-film materials composed of alternate ferromagnetic and nonmagnetic layers. The resistance of the material is lowest when the magnetic moments in the ferromagnetic layers are aligned and highest when they are anti-aligned. These materials operate at room temperature and exhibit substantial changes in resistivity when subjected to relatively small magnetic fields (100 to 1000 Oe). Applications of this remarkably simple effect include magnetic field sensors, read heads, galvanic isolators, and nonvolatile magnetic random access memory (MRAM).

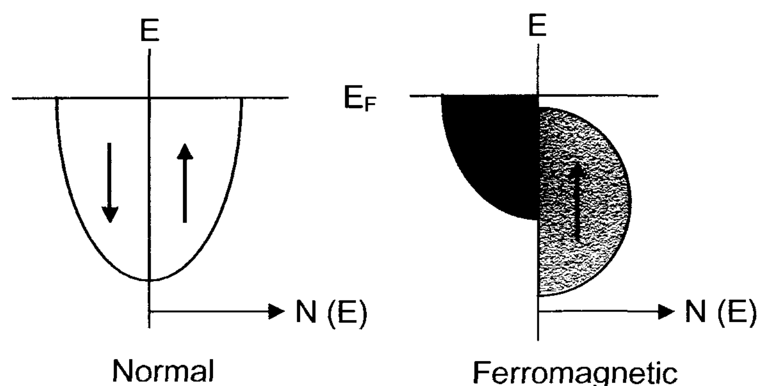

Fig. 1.1: A schematic representation of the density of electronic states that are available to electrons in a normal metal, and in a ferromagnetic metal whose majority spin states are completely filled. E denotes the electron energy; E_F is the Fermi level; N(E) denotes the density of states. [2]

A successful commercial application is spin-valve-based read heads in hard drives. A spin valve structure is composed of two ferromagnetic layers separated by a

Reproduced with permission of the copyright owner. Further reproduction prohibited without permission.

nonmagnetic metal. One of the two magnetic layers is pinned, i.e, the magnetization of this layer is relatively insensitive to a moderate external magnetic field. In contrast, the magnetization in the second layer can be reversed by application of a small magnetic field. Basically, the magnetic configuration can be switched between parallel and antiparallel configuration by a field of only a few Oersted, so that a large change of resistance (~10 %) can be induced by a very small field. The spin valve-based read heads have led to an increase of the density of stored information by almost two orders of magnitude. It might however be hard to go beyond the 100 Gbit/in^2 of today's prototypes with conventional spin valves. A further increase of read head sensitivity and information density in hard discs will likely be achieved with magnetic tunnel junctions (MTJs) [5] where the current is perpendicular to the planes (CPP).

More recent work has been focused on the integration of MTJs in integrated circuits to function like a static semiconductor RAM chip with the added feature that the data are retained with power off. Potential advantages of MRAM compared with silicon electrically erasable programmable read-only memory (EEPROM) and flash memory are 1000 times faster write times, no wearout with write cycling (EEPROM and flash wear out with about 1 million write cycles), and lower energy for writing. MRAM data access times are about 1/10,000 that of hard disk drives.

While metallic spin devices provide new ways to store and read information in hard discs, tapes or MRAM, semiconductor-based spintronics may offer many new avenues and opportunities which are inaccessible to metal-based structures. This is due to the characteristics for which semiconductors are so well known: the existence of a bandgap which can often be tuned over a significant range in ternary compounds, the

Reproduced with permission of the copyright owner. Further reproduction prohibited without permission.

accompanying optical properties on which a vast optoelectronic industry is based, and the ability to readily control carrier concentrations and transport characteristics via doping, gate voltages and band offsets. Coupling the spin degree of freedom in modern electronics may add substantially more functionality and capability to semiconductor devices. In such devices, a magnetic state can be transformed into an optical signal and vice versa, and the manipulation of spins presents some advantages in terms of speed and required power over the transport of charge in conventional electronics. Furthermore, semiconductor-based spintronics could combine storage, detection, logic, and communication capabilities on a single chip to produce a multifunctional device that could replace several components.

A number of semiconductor-based spin dependent devices have been proposed and discussed. One of the earliest devices proposed by Datta and Das [6] is the spin-polarized field effect transistor (spin-FET) shown in Fig. 1.2. Spin-polarized electrons are injected from a ferromagnetic pad into an inversion layer formed at the heterojunction providing a very high mobility two-dimensional electron gas channel, free of spin flip scattering events. The electric field in this layer induces a spin-orbit effect on the carriers drifting parallel to the interface, which causes the spins of the carriers to precess. The spin precession can be altered by applying a gate voltage to increase or decrease the effective electric field. When these carriers reach the ferromagnetic drain contact, they will be transmitted or reflected with some probability depending on the alignment of the carriers spin with respect to the magnetization vector in the drain pad, thus permitting the modulation of the current passing through the device.

Reproduced with permission of the copyright owner. Further reproduction prohibited without permission.

Other semiconductor spintronic devices proposed in the literature include: light emitting diodes (Spin-LEDs), tunable optical isolator, resonant tunneling diodes (Spin-RTDs), gated spin coherent devices, and quantum bits (Qubits) for quantum computing. Some degree of success has been achieved in each of these devices. However, more significant progress toward a practical device has been hampered by the lack of one or more of the components essential to the intended operation.

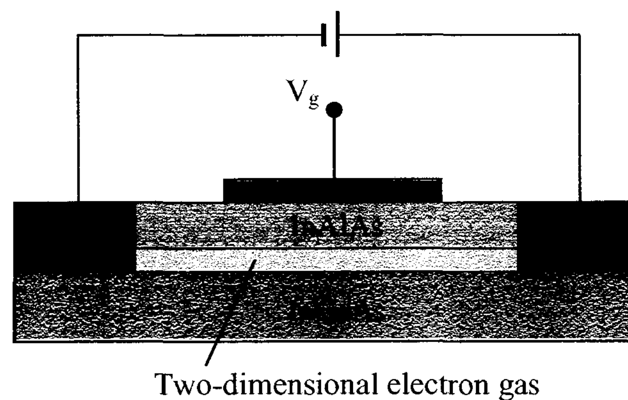

Fig. 1.2 Spin-polarized field effect transistor scheme. V_g is the gate voltage. [6]

There are four essential requirements for implementing semiconductor spintronics technology in practical devices, as can be seen by inspection of the spin-FET:

1) efficient injection of spin-polarized carriers into semiconductors,
2) sufficient spin diffusion length and lifetime for transport within the semiconductor host medium,
3) effective control and manipulation of spin carriers,
4) efficient detection of spin to provide the result.

Reproduced with permission of the copyright owner. Further reproduction prohibited without permission.

Successful spin injection into semiconductors has been achieved by using magnetic semiconductors and ferromagnetic metals as spin injecting contact. This will be discussed in more detail in the following section.

A number of time-resolved optical experiments have demonstrated a remarkable long spin lifetime and efficient spin transport in direct band gap semiconductor materials such as GaAs [7-9]. In these experiments, a circular-polarized optical pulse is used to create spin-polarized carriers and a time delayed probe pulse monitors the phase, amplitude, and location of the resulting spin precession. Spin lifetimes >100 ns [7] and spin diffusion length of many microns [8,9] have been reported in optically pumped bulk GaAs. In quantum dots, nanosecond spin dynamics persists to room temperature, and a longer spin lifetime [10,11] has been observed as the discrete energy spectrum and the exclusion principle inhibit both elastic spin flip and inelastic phonon scattering mechanism.

1.2 Spin injection

Spin polarized carriers can be generated by optical pumping utilizing quantum selection rules in bulk semiconductor as well as in heterostructure and quantum dots. However, electrical generation of spins is more preferred for integration with existing semiconductor technology.

One simple approach to electrically generate spin polarized carriers in a semiconductor is the injection of spins from a magnetic material in intimate contact with the semiconductor. Great efforts have been put into synthesis and characterization of new magnetic semiconductors since such materials enable the design of the spin injecting

Reproduced with permission of the copyright owner. Further reproduction prohibited without permission.

interface based on the familiar principles of bandgap engineering between similar structures and properties.

The first demonstrations of electrical spin injection were reported by Fiederling *et al* [12] and Jonker *et al* [13] using a diluted magnetic semiconductor (DMS) as magnetic contact. In both cases, electron spin polarization of more than 50% reveals an efficient spin transport across the interface. However, the requirements of relatively low temperature (<10 K) and high magnetic field (>1 T) inhibit practical application.

Ferromagnetic semiconductors (FMS) exhibit long range ferromagnetic order below a characteristic Curie temperature and can also be used for spin injection. Recently, FM order was discovered in GaMnAs and InMnAs where Mn acts as both magnetic element and acceptor providing the source of spin polarized holes [14]. Although such host semiconductor materials are widely recognized for applications, the extremely short spin lifetime of the holes and high hole mass are serious drawbacks for device operation [3].

The difficulties of achieving high spin-injection efficiency from magnetic semiconductors in a practical regime led to an extensive investigation of ferromagnetic metals as magnetic contacts. Although the metal-semiconductor interface structure for these materials is not well understood, ferromagnetic metals present several advantages in terms of low coercive field, high Curie temperature and fast switching time over the magnetic semiconductor.

In the diffusive transport regime, spin injection from a FM metal in intimate contact with a semiconductor was measured to be less than 1% [15]. Theoretical calculations attribute this small effect to the conductivity mismatch between metal and

Reproduced with permission of the copyright owner. Further reproduction prohibited without permission.

semiconductor which leads to spin accumulation and enhanced spin flip scattering at the heterointerface [16,17]. In such condition, successful spin injection can be achieved only if the spin polarization in the metal is 100%. However, this obstacle can be circumvented by inserting a tunneling barrier, so that the resistance is dominated by the interface supporting a difference in electrochemical potential between the spin-up and spin-down bands [18]. Indeed, several groups have reported successful spin injection into semiconductor heterostructures from FM metals using a variety of tunnel barriers, including Schottky contacts, thin metal oxides and AlAs [19-21].

Metal oxide such as AlO forms a canonical rectangular barrier which can be easily controlled by altering the tunneling width. The Schottky contact formed between a metal and a semiconductor provides a natural potential barrier with pseudo-triangle shape. The barrier width represented by the depletion layer can be controlled by the doping level of the semiconductor.

Half-metallic ferromagnets represent a new class of materials for spin injection contacts. The concept of half-metallic ferromagnets was introduced by de Groot *et al.* [22], on the basis of band structure calculations in NiMnSb and PtMnSb semi-Heusler phases. Due to the ferromagnetic coupling, the spin-up subband (generally the majority-spin) is metallic, whereas the Fermi level falls into a gap of the spin-down subband. Thus, the spin polarization of electrons at the Fermi level is 100%, which meets the criteria for efficient spin injection in the diffusive regime. Obvious conditions for the occurrence of this new class of materials are the existence of narrow bands and energy gaps in the energy spectrum, and of strong ferromagnetic interactions. Half metals are the extreme case of strong ferromagnets (or saturated Hubbard ferromagnets), where not only 3d

Reproduced with permission of the copyright owner. Further reproduction prohibited without permission.

electrons are fully polarized, but also other unpolarized bands (s or p type) do not cross the Fermi level. Besides the case of semi-Heusler compounds, half metallic behavior is also found in CrO_2 and in $(La_{1-x}Sr_x)MnO_3$ (LSMO) ferromagnetic manganites at room temperature.

1.3 Spin transport across interface

Spin transport in a magnetic heterostructure may be strongly affected by the character of the interface, which was revealed by experiments as well as theoretical studies.

First, Stroud *et al* [23] highlighted the importance of interface defects: Analysis of ZnMnSe/AlGaAs(001) spin polarized light-emitting diodes (spin-LEDs) revealed that interface defects, such as stacking faults, limit spin-injection efficiency in diffusive transport, and thus are a potential source of spin flip scattering in semiconductor spintronic devices. In addition, a band offset across the heterointerface is an important factor in affecting the spin-flip scattering rate. The dissipation of high kinetic energy of spin-polarized carriers diffusing through an interface with high band offset is likely to proceed by non-spin-conserving mechanism, lowering the spin polarization.

An interface derived effect was also observed in $La_xSr_{1-x}MnO_3/SrTiO_3$ (LSMO/STO) tunnel junctions. Here the tunneling magnetoresistance is much smaller than that expected from the half metallic nature of LSMO, and the response is diminished at temperature far below Curie temperature T_c [24,25]. The decreased MR has been attributed to severe deterioration of the ferromagnetism locally occurring near the LSMO/STO interfacial region [26].

Reproduced with permission of the copyright owner. Further reproduction prohibited without permission.

More interestingly, the interface may change the sign of spin polarization of carriers tunneling from a FM metal into an insulator or semiconductor layer. In the past decade, extensive data have been obtained with FM/AlO/Al junctions, and a positive polarization has been found for all the ferromagnetic metals and alloys that have been studied [27]. This is surprising, especially for metals like Co or Ni in which a negative polarization is expected from the smaller density of states at Fermi level for the majority spin band. Recent studies [28,29], however, show that the sign of the spin polarization depends on the choice of the barrier materials. In Co/I/LSMO tunnel junctions, the effective polarization of Co was found to be positive when I is AlO, and negative when I is STO or $Ce_{0.69}La_{0.31}O$ (CLO). Theoretical calculations have shown that the charge transfer and bonding mechanism modify the spin-polarized density of states (DOS) at the interface layer. This can be viewed as a purely interface filtering effect controlling the polarized evanescent wave in the barrier [30,31].

In summary, interface driven magnetic interactions may lead to differences in magnetic character between the interface and bulk layers, manifested as changes in magnetic moment and spin polarization. These characters are essential in determining the steady state of the injected current. However, aforementioned observations provide no direct clarification of the magnetic characters at the interface. Therefore, it is highly desirable to develop new approaches to directly probe the spin-polarized density of states at the interface. In addition, it is equally important to address the interface magnetic anisotropy and magnetization reversal process which may also be quite different due to the discontinuity of the chemical environment at the interface in such hybrid structures.

Reproduced with permission of the copyright owner. Further reproduction prohibited without permission.

These properties have great impact on the switching behavior and precessional dynamics, which are key elements for high speed spintronic devices.

1.4 Magnetization switching and dynamics

Understanding the magnetization dynamics and switching process has become important as magnetic recording and magnetoelectronic technologies push toward operation in the gigahertz regime and nanoscale size. In large particles, the magnetization switches by nucleation and expansion of reversed domains, leading to the switching time in the nanosecond range due to spin lattice relaxation, which was very fast from the perspective of semiconductor technology decades ago. This intrinsic response time, however, is now a potential limitation of magnetic technology, which must keep pace with semiconductor circuits that can operate well above 1 GHz. Thus, a faster switching mode is required to improve the operation speed of spintronic devices such as MRAMs. Indeed, a prominent fast switching mode can occur by uniform rotation in small particles with a single domain, which may push the switching time into the picosecond range.

Precessional switching was first demonstrated by using a shaped magnetic field pulse [32], where the magnetization **M** precesses around a transient field applied perpendicular to **M** and stops at the opposite direction when the field ends. Recently, a spin-polarized current is found to apply a torque to the local magnetization by transferring spin angular momentum to **M** [33], allowing excitation of a steady state precessional mode and a magnetization reversal without application of a magnetic field. Moreover, coherent control of magnetization by ultrashort laser pulse may provide a new scheme of non-field-driven manipulation and switching. Advanced techniques to shape

Reproduced with permission of the copyright owner. Further reproduction prohibited without permission.

laser pulse provide the possibility to manipulate the magnetization with high precision. In all of these approaches, precise control of ultrafast magnetization dynamics is a crucial prerequisite to achieve reliable and fast switching.

Time-resolved magneto-optical technique allows investigation of the evolution of spins and their interaction with electrons and phonons in femtosecond timescales, thus providing a microscopic view into the excitation and relaxation process of magnetization precession. It is anticipated that these investigations will significantly contribute to further development of spintronics.

1.5 Scope of this dissertation

In the course of this dissertation, I performed time-resolved nonlinear/linear magneto-optical studies on ferromagnetic-metal/semiconductor and half-metallic-ferromagnet/insulator heterointerfaces, and internal photo-emission studies on ferromagnetic/nonmagnetic semiconductor heterointerfaces. The goal has been to develop approaches to directly study interface magnetism, spin dynamics, and electronic properties relevant to spin injection and MTJ application. The focus is on three important systems:

Ferromagnetic-metal/Semiconductor Interface - For the first time, magnetization-induced second-harmonic-generation (MSHG) is applied to directly study interface magnetism in a hybrid structure containing a noncentrosymmetric semiconductor - Fe/AlGaAs. A strong interface magnetization induced effect is observed in the azimuthal dependence of SH intensity for judicious selection of a polarization combination, leading to a high sensitivity to interface magnetization. The reversal process of Fe interface layer

Reproduced with permission of the copyright owner. Further reproduction prohibited without permission.

magnetization is compared with the reversal of the bulk magnetization obtained from the magneto-optic Kerr effect (MOKE). The switching characteristics are distinctly different due to interface-derived anisotropy – single step switching occurs at the interface layer, while two-jump switching occurs in the bulk Fe for the magnetic field orientations employed in Fe/AlGaAs (001). Furthermore, a time-resolved MSHG (TR-MSHG) study demonstrates a coherent interface magnetization precession, implying the feasibility of fast precessional control of interfacial spin. The interface magnetic anisotropy is analyzed based on Landau-Lifshitz-Gilbert (LLG) equations. It is also compared with the bulk anisotropy determined from bulk magnetization precession measurements.

Half-metallic Ferromagnet/Insulator Heterostructure – Time-resolved MOKE experiments (TR-MOKE) are performed to systematically study the magnetization precession in $La_{0.67}Ca_{0.33}MnO_3$ (LCMO) and $La_{0.67}Sr_{0.33}MnO_3$ (LSMO) on different substrates including $SrTiO_3$, $NdGaO_3$ (NGO), and $LaAlO_3$ (LAO). The measurements are carried out in a wide range of magnetic field (0 ~ 4 T) and temperature (10 ~ 300 K), with precession frequency varying from several to hundred GHz. The magnetic anisotropy is determined from the measured field and azimuthal dependence of the precession frequency. The interface bonding and strain induce a pronounced effect on the magnetization precession dynamics.

Ferromagnetic/Nonmagnetic Semiconductor Heterojunction – Internal photo-emission is applied to determine the band offsets at $CdCr_2Se_4$–(AlGa)As and $CdCr_2Se_4$–ZnSe interfaces. The conduction band offsets ΔE_c = 660 and 530 meV at the $CdCr_2Se_4$–GaAs and $CdCr_2Se_4$– ZnSe interfaces are determined from the threshold energies of the

Reproduced with permission of the copyright owner. Further reproduction prohibited without permission.

photocurrent spectrum at room temperature. The band offset has been reduced successfully by engineering of the interface bonding and stoichiometry.

Reproduced with permission of the copyright owner. Further reproduction prohibited without permission.

Chapter 2

Experimental Techniques

This chapter presents the optical characterization techniques which have been used to study magnetic and electronic properties. Section 2.1 describes the magneto-optic Kerr effect and the optical geometries for measuring magnetization vector components. An interface magnetization sensitive technique – magnetization-induced second-harmonic generation – is described in section 2.2, including a detailed analysis of nonlinear susceptibilities in Fe/AlGaAs and the corresponding experimental consideration. Section 2.3 presents the time-resolved magneto-optic techniques for probing interface and bulk magnetization dynamics. The magnetization precessions and its mathematical derivations are also discussed in this section. Section 2.4 describes the internal photoemission technique utilizing a table-top tunable laser system with high brightness.

2.1 Magneto-optic Kerr effect

A linear polarized light undergoes a change of polarization state upon reflection from a magnetic medium. This is known as magneto-optic Kerr effect. Magneto-optics is presently described in the context of either microscopic quantum theory [34] or macroscopic dielectric theory [35].

Reproduced with permission of the copyright owner. Further reproduction prohibited without permission.

Microscopically, the coupling between light and electron spin occurs through the spin-orbit coupling, $(\nabla V \times p) \bullet s$, which results from the interaction of the electron spins with the effective magnetic field the electron "sees" as it moves through the electric field $-\nabla V$ with momentum p inside a medium. Such an interaction gives rise to off-diagonal components of the dielectric tensor, which is determined by the motion of electrons in a magnetic medium with imbalanced populations of spin-up and spin-down electrons.

Macroscopic descriptions of the magneto-optic effect are based on the dielectric properties of a magnetic medium, represented by a dielectric tensor [35]:

$$\varepsilon = \varepsilon_0 \begin{pmatrix} 1 & iQ_z & -iQ_y \\ -iQ_z & 1 & iQ_x \\ iQ_y & -iQ_x & 1 \end{pmatrix}. \tag{2.1}$$

From Maxwell's equations, the normal modes of light propagating in such medium are left-circular polarized light with refraction index $n_L = n(1 - \frac{1}{2}\vec{Q} \bullet \hat{k})$, and right-circular polarized light with refraction index $n_R = n(1 - \frac{1}{2}\vec{Q} \bullet \hat{k})$, where $n = \sqrt{\varepsilon}$ is the average refraction of index, $\vec{Q} = (Q_x, Q_y, Q_z)$ is the Voigt vector, and $\hat{k}$ is the unit vector along the direction of the light propagation. A linear polarized light propagating in the medium will then decompose into left- and right-circular polarized light modes. The difference between the real parts of n_L and n_R results in phase shifts of the two normal modes due to their different propagating velocities, leading to a rotation of polarization plane of the light. At the same time, the difference between the imaginary parts of n_L and n_R cause the different absorption rates for the two normal modes, affecting the ellipticity of the light.

Reproduced with permission of the copyright owner. Further reproduction prohibited without permission.

The magneto-optic Kerr effects are categorized according to the geometry of the magnetization in relation to the plane of incidence and the film plane (Fig. 2.1): the longitudinal geometry, in which the applied field lies in the plane of the sample and in the incident plane; the transverse geometry, in which the applied field lies in the plane of the sample but is perpendicular to the incident plane; and the polar geometry, in which the applied field is perpendicular to the plane of the sample and in the incident plane.

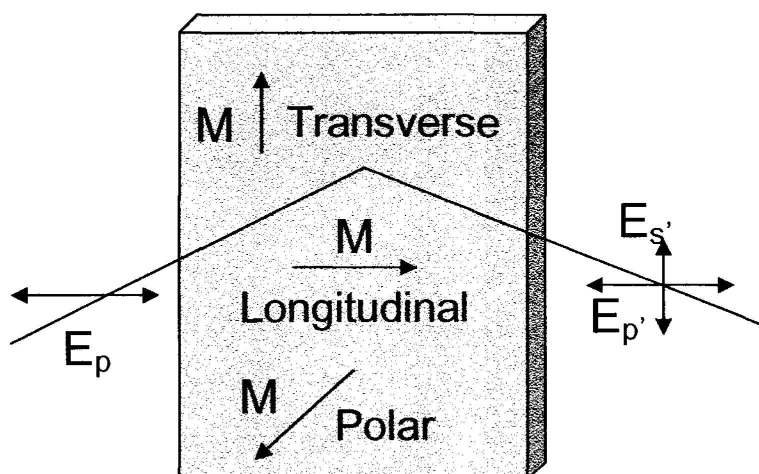

Fig. 2.1: Geometries of longitudinal, transverse, and polar Kerr effects.

For conventional MOKE measurements, a beam of light passes through a linear polarizer and is incident on the sample, and the reflected beam passes through an analyzing polarizer (analyzer) and is measured by a photodetector. The setting of the analyzer depends on the magnetization component to be detected. For the longitudinal (or polar) geometry, the analyzer angle is set close to 90° with respect to the incident plane of

Reproduced with permission of the copyright owner. Further reproduction prohibited without permission.

polarization. For the transverse geometry, the analyzer is set to 0° to transmit light with the same polarization as incident light. At analyzer angles between these extremes, the intensity of the transmitted light depends upon both components [36].

The nature of the magneto-optic Kerr effect depends on the orientation of the magnetization **M** with respect to the incident plane and the plane of the sample. The longitudinal and polar components of **M** changes the polarization state of the light upon reflection. In contrast, the transverse component of **M** only change the intensity of the reflected beam (for p polarized incident light), and no ellipticity occurs [37]. This is summarized in Table 2.1.

Table 2.1: The Fresnel coefficients for p polarized light incident on a magnetic layer having dielectric constant of ε. The incident angle and the refracted angle in the magnetic layer is given by θ_1 and θ_2. The substitutions $\alpha_1 = \cos\theta_1$ and $\alpha_2 = \cos\theta_2$ are used. The Voigt coefficients Q_P, Q_L and Q_T are proportional to the magnitude of the magnetization along the corresponding directions.

	r_{pp}	r_{ps}
Polar	$\frac{\sqrt{\varepsilon}\alpha_1 - \alpha_2}{\sqrt{\varepsilon}\alpha_1 + \alpha_2}$	$\frac{Q_P\sqrt{\varepsilon}\alpha_1}{i(\sqrt{\varepsilon}\alpha_1 + \alpha_2)(\alpha_1 + \sqrt{\varepsilon}\alpha_2)}$
Longitudinal	$\frac{\sqrt{\varepsilon}\alpha_1 - \alpha_2}{\sqrt{\varepsilon}\alpha_1 + \alpha_2}$	$\frac{Q_L\sqrt{\varepsilon}\alpha_1 \tan\theta_2}{i(\sqrt{\varepsilon}\alpha_1 + \alpha_2)(\alpha_1 + \sqrt{\varepsilon}\alpha_2)}$
Transverse	$\frac{\sqrt{\varepsilon}\alpha_1\sqrt{1 - Q_T^2/\alpha_2^2} - \alpha_2 - i\sqrt{\varepsilon}Q_T\alpha_1 \tan\theta_2}{\sqrt{\varepsilon}\alpha_1\sqrt{1 - Q_T^2/\alpha_2^2} + \alpha_2 - i\sqrt{\varepsilon}Q_T\alpha_1 \tan\theta_2}$	0

Reproduced with permission of the copyright owner. Further reproduction prohibited without permission.

2.2 Magnetization-induced second-harmonic-generation

2.2.1 Nonlinear magnetic susceptibility

The optical second-harmonic polarization **P** (2ω) of a magnetic medium is phenomenologically described by a third-rank nonlinear susceptibility tensor for the crystallographic contribution χ_{ijk}^{cr} and a fourth-rank axial tensor χ_{ijkl}^{m} for the magnetization-induced part [38]:

$$P_i(2\omega) = \chi_{ijk}^{cr} E_j(\omega) E_k(\omega) + \chi_{ijkl}^{m} E_j(\omega) E_k(\omega) M_l, \quad \text{i, j, k,l = x, y, z} \tag{2.2}$$

where M is the magnetization of the medium and E(ω) is the fundamental field. In the bulk of a centrosymmetric medium, the electric dipole contributions to both nonlinear susceptibilities are identically zero. At the surface and interface, the inversion symmetry is broken, resulting in the surface and interface induced components. The magnetization of the medium will not break the inversion symmetry of the bulk, but can lower the surface and interface symmetry modifying the nonlinear susceptibility. Therefore, χ_{ijkl}^{m} is only nonzero at the surface and interface in a centrosymmetric medium.

For a particular magneto-optical configuration, Eq. (2.2) may be simplified to one third-rank tensor with different components, which are either even or odd in M, describing the crystallographic or the magnetization-induced contribution, respectively:

$$P_i(2\omega, \pm M) = (\chi_{ijk}^{+}(\pm M) \pm \chi_{ijk}^{-}(\pm M)) E_j(\omega) E_k(\omega). \tag{2.3}$$

The odd component χ_{ijk}^{-} changes sign upon magnetization reversal and therefore give rise to the magnetic asymmetry in the MSHG response.

On a microscopic level, this asymmetry arises, as in linear magneto-optics, due to the splitting of the energy levels by the exchange and the spin orbit interactions [39,40].

Reproduced with permission of the copyright owner. Further reproduction prohibited without permission.

The relation between the microscopic spin-dependent band structure and the nonlinear magneto-optical susceptibility can be written as:

$$\chi_{ijk}(2\omega;\omega,\omega) \propto \sum_{a,b,c} \frac{\langle a|i|c\rangle\langle c|j|b\rangle\langle b|k|a\rangle}{(2\hbar\omega - E_{ca} + i\hbar\Gamma_{ca})(\hbar\omega - E_{ba} + i\hbar\Gamma_{ba})}, \tag{2.4}$$

where $|a\rangle$, $|b\rangle$, and $|c\rangle$ are spin dependent initial, intermediate, and final states.

The symmetry of the nonlinear susceptibility is dictated by the symmetry of the particular surface under consideration. The nonzero elements of χ can be obtained under symmetry operations [41]:

$$\chi_{ijk} = \Sigma\ \Sigma\ \Sigma\ T_{ii'}T_{jj'}T_{kk'}\chi_{i'j'k'}, \tag{2.5}$$

where T is the 3 ×3 transformation matrix for each symmetry operation.

Similar to MOKE, the MSHG response depends on the geometry of magnetization in relation to the incident light and sample plane. The measured intensity in a fixed experimental geometry with opposite magnetization direction can, in general, be written as a sum of effective tensor components:

$$I^{\pm}(2\omega) \propto \left|\chi^{+}_{eff}(2\omega) \pm \chi^{-}_{eff}(2\omega)\right|^2 \tag{2.6}$$

where χ^{+}_{eff} and χ^{-}_{eff} are linear combinations of the even and odd tensor elements and Fresnel factors α_{ijk}:

$$\chi_{eff} = \sum_{i,j,k} \alpha_{ijk}\chi_{ijk} \tag{2.7}$$

The magnetic asymmetry can then be defined as

$$A = \frac{I^{+} - I^{-}}{I^{+} + I^{-}} \tag{2.8}$$

Reproduced with permission of the copyright owner. Further reproduction prohibited without permission.

Because the asymmetry A is normalized to the total SH intensity, it does not depend on the intensity of the fundamental light. Thus, a large asymmetry A can be expected since the magnitude of the odd components may be in the same order of that of even components, leading to a large nonlinear Kerr rotation which can be 3 orders of magnitude stronger than the linear one [42,43].

Previous studies on the buried interface magnetization by MSHG have focused on the centrosymmetric structures. In the following, MSHG studies on the interface magnetization in Fe/AlGaAs containing a noncentrosymmetric material are discussed.

Table 2.2: The nonzero elements of the MSHG susceptibility tensor for Fe/AlGaAs (001) structure in the longitudinal configuration ($\vec{M}$ // $\hat{x}$). The surface is in the $\hat{x}$-$\hat{y}$ plane. χ^+ and χ^- denote the even and odd elements with magnetization. The even elements from interface and bulk are indicated by subscripts a and b.

Sample Orientation	χ^+	χ^-	Input Polarization	Output Polarization
M_x // [100]		yyy	s	s
	$yxz^b = yzx^b$	yxx, yzz	p	s
	zyy^a		s	p
	$xzx^a = xxz^a$, zxx^a, zzz^a		p	p
M_x // [110]		yyy	s	s
		yxx, yzz	p	s
	$zyy^{a,b}$		s	p
	$xzx^{a,b} = xxz^{a,b}$, $zxx^{a,b}$, zzz^a		p	p

Although MSHG is intrinsically sensitive to the interface magnetization in the centrosymmetric layer (Fe: bcc), a bulk response may be generated in the noncentrosymmetric material (AlGaAs: zinc blende) which significantly reduces the nonlinear magneto-optical effect. However, this bulk derived signal may be avoided by judicious selection of input- and MSHG-light polarization combination. To quantitatively

Reproduced with permission of the copyright owner. Further reproduction prohibited without permission.

describe this, we have analyzed the tensor components χ^{+}_{ijk} and χ^{-}_{ijk} in Fe/AlGaAs (001) heterostructures and collect in Table 2.2.

For both principle crystallographic directions <100> and <110>, the magnetic components χ^{-}_{ijk} contribute only to the s-polarized MSHG signal. In particular, for *s*-input polarization and *s*-polarized MSHG signal, a large bulk response from the GaAs (001) substrate can be avoided since it contains only a magnetization-induced response. This combination yields the following azimuthal pattern for the SH intensity measurement:

$$I(2\omega,\phi,\pm M) = \left| \pm A^{s,s} \pm B^{s,s} \cos 4\phi \right| \tag{2.9}$$

Here the coefficients $A^{s,s}$ and $B^{s,s}$ are the combinations of magnetization-induced nonlinear tensor elements and Fresnel factors. These terms change sign upon magnetization reversal. However, this pattern does not yield any effect of magnetization reversal for the MSHG intensity measurement. Therefore, a mixture of small *p*-polarized bulk SHG component with MSHG signal is required to obtain a magnetic contrast in such measurement. This can be achieved simply by rotating the analyzer a few degrees. In addition, the signal in ideal $S_{in}S_{out}$ combination is normally small as shown in measurements from centrosymmetric structures, which may lead to very low signal to noise ratio for the M-H loops. Although the bulk signal can reduce the magnetic contrast, a small mixed-in bulk component may be helpful to improve the signal to noise ratio because the interference of this component with the magnetization induced response will increase the total MSHG intensity. We will show later in the experiment that this mixed-in component is indeed helpful to enhance the nonlinear magneto-optical response, resulting in high sensitivity to the interface magnetization.

Reproduced with permission of the copyright owner. Further reproduction prohibited without permission.

Similarly, we have analyzed the tensor components χ^{+}_{ijk} and χ^{-}_{ijk} in Fe/GaAs (110) heterostructure collected in table 2.3. In contrast to (100) face, no simple polarization combinations can be used to measure the azimuthal pattern showing magnetization effect in this structure. To get a high magnetic contrast in the magnetization reversal measurements, we need to select specific polarization combinations for different orientations. From the table, we find that $P_{in}S_{out}$ can be used for [001] and [-111] directions, and $S_{in}S_{out}$ is suitable for [001] and [1-10] directions.

Table 2.3: The nonzero elements of the MSHG susceptibility tensor for Fe/AlGaAs (110) structure in the longitudinal configuration ($\vec{M}$ // $\hat{x}$). The surface is in the $\hat{x}$-$\hat{y}$ plane. χ^{+} and χ^{-} denote the even and odd elements with magnetization. The even elements from interface and bulk are indicated by subscripts a and b.

Sample Orientation	χ^{+}	χ^{-}	Input Polarization	Output Polarization
M_x // [001]		yyy	s	s
		yxx, yzz	p	s
	zyy^a, xyy^b		s	p
	xzx^a=xxz^a zxx^a, zzz^a zxz^b=zzx^b xzz^b		p	p
M_x // [-111]	yyy^b	yyy	s	s
	yzx^a=yxz^a yxx^a, yzz^b	yxx, yzz	p	s
	zyy^b, xyy^b	xyy	s	p
	xzx^a = xxz^a zxx^a, zzz^a xxx^b, xzz^b zxz^b=zzx^b	xxx, xzz zxz=zzx	p	p
M_x // [1-10]		yyy	s	s
	yxx^b, yzz^b	yxx, yzz	p	s
	zyy^a		s	p
	xzx^a=xxz^a zxx^a, zzz^a		p	p

Reproduced with permission of the copyright owner. Further reproduction prohibited without permission.

2.2.2 Experimental considerations

MSHG experiments are performed with a Ti:sapphire amplifier system (Spectra Physics) generating 150-femtosecond pulses with 1-mJ energy at 1-KHz repetition rate and 800-nm wavelength. The attenuated laser beam (15 mW) is focused to a ~500-μm diameter spot on the sample at an angle of incidence of 45° (Fig. 2.2). The SHG signal is generated in the direction of the reflected laser beam, and is detected with a high signal-to-noise ratio using a photomultiplier tube (PMT) (Hamamatsu R2949) and a chopper in combination with a lock-in amplifier (PerkInElmer 7265). The SHG light is effectively filtered using the combination of a prism and blue filters. For measurements of the azimuthal angle dependence of the MSHG signal, the sample is mounted on a computer-controlled rotation stage between the poles of an electromagnet, with the magnetic field applied in the plane of the Fe film. The experimental setup allows measurements of magnetic hysteresis loops in longitudinal geometry.

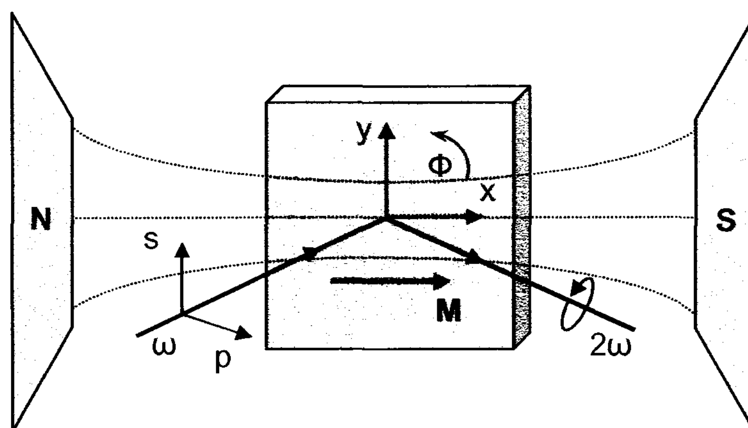

Fig. 2.2: Schematic MSHG experimental geometry: sample rotates azimuthally in the applied magnetic field in longitudinal magneto-optical configuration. The notations p and s denote the polarizations parallel and perpendicular to the incident plane of reflection, respectively.

Reproduced with permission of the copyright owner. Further reproduction prohibited without permission.

First, we performed rotational SHG measurements at zero field in 10-nm Fe films grown on AlGaAs (001) for different polarization combinations (Fig. 2.3). The SHG response for the combination of input p and output s polarizations shows a four-fold symmetry, indicating a pure bulk response from AlGaAs layer and the substrate. Both four-fold and two-fold symmetry are revealed in the SHG response for combination of input p and output p polarizations. This is caused by a superposition of cubic bulk SHG response and an isotropic component generated from Fe/AlGaAs interface. The surface contribution to isotropic SHG is small due to the oxidization when exposure to the ambient air. Such results are well expected for a bilayer system of a body-centered-cubic (bcc) crystal on a zinc-blende structure, indicating a well established setup ready to probe the SHG response from the interface magnetization.

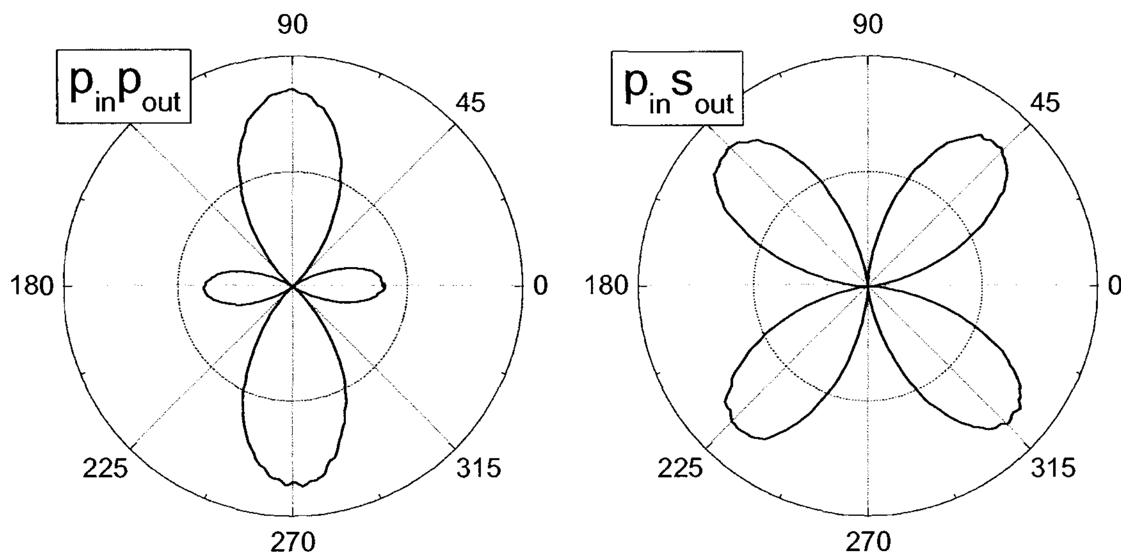

Fig. 2.3: Rotational SHG intensity curves from 10 nm Fe (001) film for different polarization combinations. The axis along 0° corresponds to the hard [1-10] direction in the bulk Fe.

Reproduced with permission of the copyright owner. Further reproduction prohibited without permission.

Next, we performed the rotational MSHG measurements in 10-nm Fe/AlGaAs (001). In these measurements, the applied field is set at ±600 Oe so that the magnetization is aligned along the field direction, and the incident light is s-polarized and the SHG light pass through the analyzer set at angle α with respect to the s-polarized direction. We can clearly see a magnetic contrast in each polarization combination shown in Figure 2.4. This magnetic contrast can be quantitatively described by the magnetic asymmetry:

$$A(\alpha) = [I(2\omega,\alpha,+M) - I(2\omega,\alpha,-M)]/[I(2\omega,\alpha,+M) + I(2\omega,\alpha,-M)], \quad (2.10)$$

where I represents the SH intensity measured for both magnetization directions, which is given by:

$$I(2\omega,\alpha,\pm M) \propto \left|E_p(2\omega)\sin(\alpha) \pm E_s(2\omega)e^{i\varphi}\cos\alpha\right|^2. \quad (2.11)$$

It is then easily calculated that

$$A(\alpha) = 2\Phi_k ctg\alpha[1 + (\Phi_K ctg\alpha)^2]^{-1}\cos\varphi \quad (2.12)$$

with the magnitude of the nonlinear complex Kerr angle $\Phi_k = E_s(2\omega)/E_p(2\omega)$. Figure 2.5 depicts the asymmetry as a function of the analyzer angle α with magnetization along [1-10] direction. We note that the asymmetry is significantly reduced when *p*-polarized light generated from bulk GaAs is involved at large α (>20°). However, the SH intensity is very small at α<1°, leading to low signal-to-noise ratio and large uncertainty of the asymmetry measurement. Therefore, the large MSHG signal and asymmetry at medium α (4°~20°) must result from the interference between bulk p-polarized component and magnetization induced s-polarized component. We determine the correlated phase φ=66°

Reproduced with permission of the copyright owner. Further reproduction prohibited without permission.

from the fit to the asymmetry measurement in Fig. 3.5 using Eq. (2.12). At the same time we obtain a nonlinear Kerr angle $\Phi_K = 1.6^\circ$.

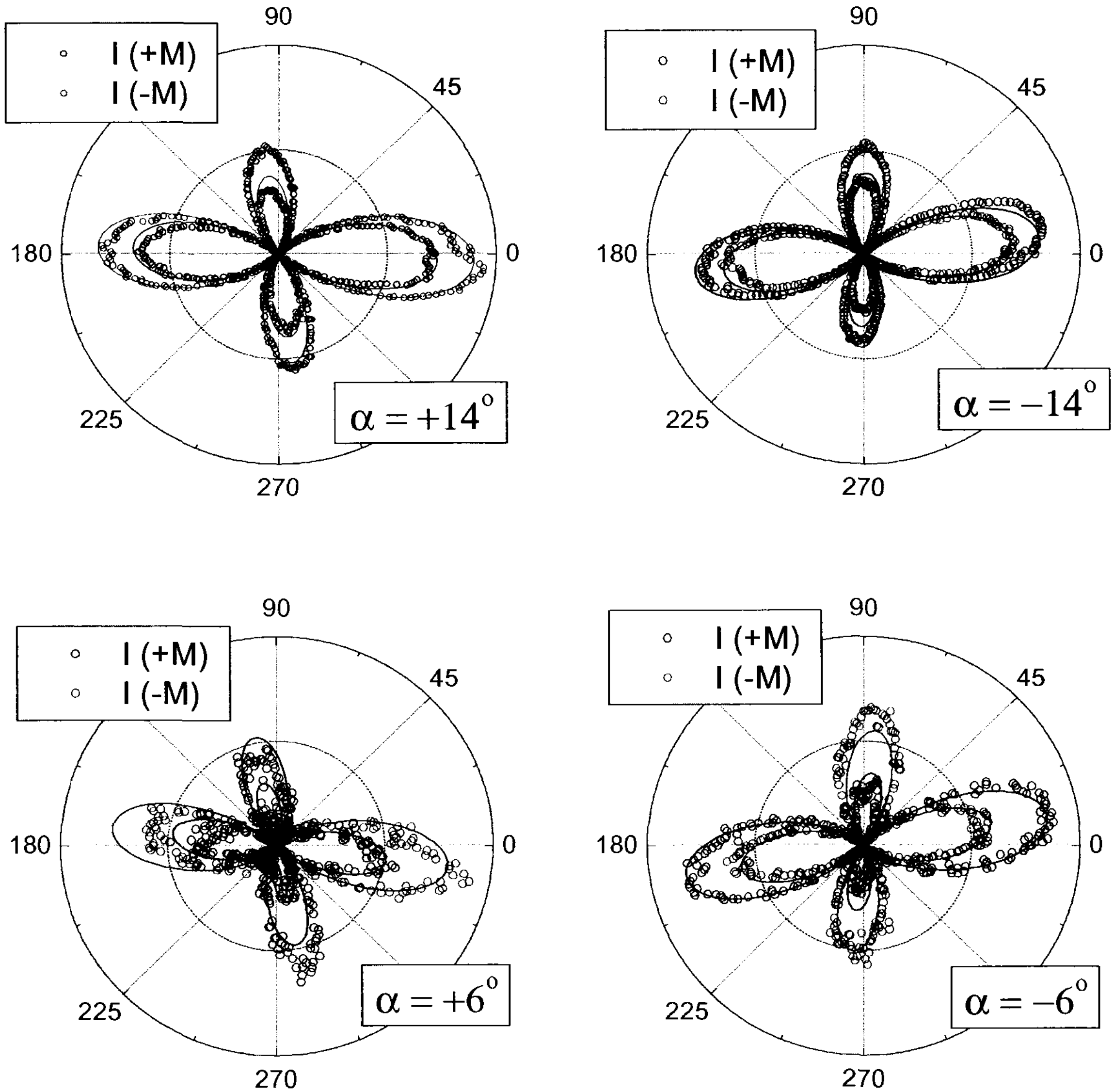

Fig. 2.4: Longitudinal nonlinear magneto-optical effect in a 10-nm Fe film on AlGaAs (001) for different analyzer angles. The incident light is s polarized, and SHG pass through the analyzer set at angle α with respect to the s-polarized direction. The experimental data are shown by circles and the best fits by Eq. (2.13) are shown by solid lines.

Reproduced with permission of the copyright owner. Further reproduction prohibited without permission.

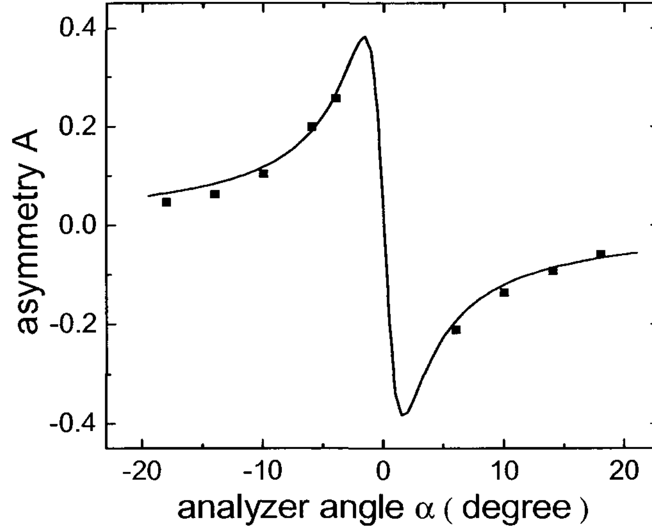

Fig. 2.5: Asymmetry A as a function of the analyzer angle α for magnetization along [1-10] direction of Fe/AlGaAs (001) for s polarized incident light. Solid line is the best fit according to Eq. (2.12).

We discuss next in detail the anisotropy components in the rotational MSHG intensity curves. The two-fold symmetry is clearly caused by p-polarized signal generated from the bulk GaAs, which has form $\cos 2\phi$. The isotropic component from the interface also contributes to the p-polarized signal. However, this even component and the odd component described in section 2.2.1 are not able to describe the angular shifts of the four loops in each curve. Therefore, one has to take into account additional anisotropic contributions to the second order nonlinear response. In particular, the nonlocal (quadrupole-allowed) contribution from the bulk of a cubic metal and semiconductor can lead to a four-fold anisotropy of SHG which has form $\sin 4\phi$ for purely $S_{in}S_{out}$ polarization combination. We may neglect the quadrupole contribution for $S_{in}P_{out}$ combination which does not contribute to the angular shift and is much smaller than other lower order components. Very surprisingly, we find a unidirectional component in the

Reproduced with permission of the copyright owner. Further reproduction prohibited without permission.

rotational intensity curves, which may result from a vicinal surface. However, the rotational patterns of $P_{in}P_{out}$ and $P_{in}S_{out}$ do not show a clear unidirectional component. The fact that this component appears in $S_{in}S_{out}$ rotational intensity curve at zero fields indicates that it is of structural origin instead of magnetic. By accounting for these additional contributions, the rotational patterns are modified as:

$$I(2\omega,\phi,\alpha,\pm M)=\left|(\pm A^{s,s}\cos\alpha \pm B^{s,s}\cos 4\phi\cos\alpha)e^{i\varphi}+C^{s,p}\sin\alpha+ D^{s,p}\cos 2\phi\sin\alpha+F^{s,s}\sin 4\phi\cos\alpha+U^{s,p}\sin(\theta+\phi)\sin\alpha\right|^2 \quad (2.13)$$

The last term in Eq. (2.13) represents the unidirectional component pointing along a direction specified by θ. This equation is used for the theoretical fits to the experimental data of Fig. 2.4, showing a good agreement between experiment and theory. The azimuthal amplitudes $A^{s,s}$, $B^{s,s}$, $C^{s,p}$, $D^{s,p}$, $F^{s,s}$, and $U^{s,p}$ used in the fits are given in Table 2.4.

Table 2.4: Azimuthal amplitudes in the fits to the rotational MSHG intensity curves by Eq. (2.13) for Fe/AlGaAs (001).

$A^{s,s}$	$B^{s,s}$	$C^{s,p}$	$D^{s,p}$	$F^{s,s}$	$U^{s,p}$
±0.6	±0.1	3	21	0.4	0.6

In the fitting process, we use the same phase φ as obtained from the analyzer angle dependence of asymmetry along [1-10] direction. From the ratio $(A^{s,s}+B^{s,s})/(C^{s,p}+D^{s,p})$, we determine the nonlinear Kerr angle along this direction, $\Phi_k \approx 1.7^\circ$, which agrees with the value obtained previously.

Reproduced with permission of the copyright owner. Further reproduction prohibited without permission.

To summarize, we find the components generating the rotational MSHG intensity are: (1) the interface magnetization-induced component, (2) the bulk nonmagnetic response from GaAs, (3) the interface (dipole-like) nonmagnetic contribution, (4) the nonlocal (quadrouple-allowed) nonmagnetic response from bulk GaAs and Fe, and (5) the nonmagnetic unidirectional contribution (its origin is not unambiguously identified).

2.3 Time-resolved MOKE and MSHG spectroscopy

2.3.1 Laser induced magnetization precession

Ultrafast demagnetization and laser induced precession are among the important magnetic phenomena triggered by short laser pulse. The femtosecond time resolution allows the investigation of precession frequencies up to tens of terahertz. The time evolution of the magnetization precession also provides direct information on damping parameters which can only be obtained indirectly from the broadened absorption lines by non-time resolved techniques. In the following we give a brief description of the precession motion of the magnetization in ferromagnetic material.

The precession motion of magnetization can be described by the Landau-Lifshitz-Gilbert equation:

$$\frac{d\vec{M}}{dt} = -\gamma\vec{M} \times H_{eff} + \frac{\alpha}{M}\vec{M} \times \frac{d\vec{M}}{dt} \tag{2.14}$$

where γ is the gyromagnetic ratio given by $g\mu_B / h$, and α is the dimensionless Gilbert damping constant. The effective field H_{eff} is the sum of external magnetic field, demagnetization field, anisotropy field, dipolar field, and exchange field. The torque on the magnetic moment produced by H_{eff} drives a precession motion around the direction

Reproduced with permission of the copyright owner. Further reproduction prohibited without permission.

of the effective field (Fig. 2.6), depicted by the first term. The precession is damped by exchanging energy and angular momentum with environment, which is described by the second term, until the magnetization finally aligns parallel to H_{eff}.

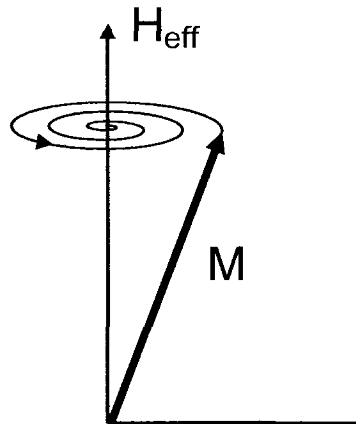

Fig. 2.6: Precession of magnetization in the effective magnetic field.

For small angle precession, Eq. (2.14) can be solved analytically involving the following steps: (1) finding the equilibrium orientation of magnetization determined by competition of the anisotropies and the applied field; (2) deriving the equations of motion describing torques acting on spins deviating slightly from the equilibrium orientation due to the effective field; (3) solving the linearized equations of motion, together with Maxwell's equations, and electromagnetic and exchange boundary conditions, to obtain the frequencies of the spin wave modes.

In the following, we give an example of how to derive the uniform magnetization precession frequency in a thin ferromagnetic film with external field H_e applied in the film plane. The measurement configuration can be described by the angle of the applied

Reproduced with permission of the copyright owner. Further reproduction prohibited without permission.

field δ and the equilibrium angle of magnetization ϕ with respect to the [100] direction of the film (Fig 2.7). The magnetic free energy of the film takes on the form:

$$E_a = \frac{K_{//}}{4}\sin^2(2\phi) + K_u \sin^2(\phi - \pi/4) + K_{\perp}\sin^2\theta + 2\pi M_z^2, \tag{2.15}$$

where $K_{//}$ and K_u are the in-plane cubic and uniaxial anisotropy constants, respectively. $K_{\perp}$ is the out-of-plane anisotropy constant, and θ denotes the equilibrium angle between the magnetization and the film plane.

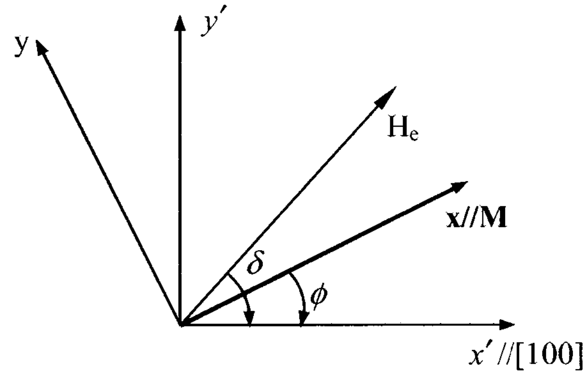

Fig. 2.7: Coordinate system used for calculating the magnetization precession frequency in a ferromagnetic thin film.

The equilibrium position of magnetization is in the film plane and given by:

$$-\frac{K_{//}}{M_s}\sin 2\phi \cos 2\phi + \frac{K_u}{M_s}\cos 2\phi + H_e \sin(\delta - \phi) = 0. \tag{2.16}$$

The magnetization precession motion driven by the magnetic torque reads:

$$\frac{dm_x}{dt}\vec{x} + \frac{dm_y}{dt}\vec{y} + \frac{dm_z}{dt}\vec{z} = -\gamma \begin{vmatrix} \vec{x} & \vec{y} & \vec{z} \\ M_s + m_x & m_y & m_z \\ H_x & H_y & H_z \end{vmatrix}, \tag{2.17}$$

Reproduced with permission of the copyright owner. Further reproduction prohibited without permission.

where H_x, H_y, H_z are the effective field components along x, y, and z directions, respectively. These fields are given by:

$$
\begin{aligned}
H_x &= -\frac{dE_a}{dM_x} + H_e \cos(\delta - \phi) \\
H_y &= -\frac{dE_a}{dM_y} + H_e \sin(\delta - \phi) \,, \\
H_z &= -\frac{dE_a}{dM_z}
\end{aligned}
\tag{2.18}
$$

where E_a needs to be rewritten as:

$$
\begin{aligned}
E_a = K_{//} & \frac{(M_x \cos\phi - M_y \sin\phi)^2 \times (M_x \sin\phi + M_y \cos\phi)^2}{M_s^4} \\
+ K_u & \frac{[M_x(\sin\phi - \cos\phi) + M_y(\cos\phi + \sin\phi)]^2}{2M_s^2} + K_\perp \frac{M_z^2}{M_s^2} + 2\pi M_z^2
\end{aligned}
\tag{2.19}
$$

Thus, the torque equations become:

$$
\begin{aligned}
\frac{1}{\gamma}\frac{dm_y}{dt} &= [-4\pi M_s - \frac{2K_\perp}{M_s} + \frac{K_{//}}{M_s}\sin^2(2\phi) + \frac{K_u}{M_s}(\sin\phi - \cos\phi)^2 - H_e \cos(\delta - \phi)]m_z \\
\frac{1}{\gamma}\frac{dm_z}{dt} &= [\frac{2K_{//}}{M_s}\cos(4\phi) + \frac{2K_u}{M_s}\sin(2\phi) + H_e \cos(\delta - \phi)]m_y
\end{aligned}
\tag{2.20}
$$

For the uniform precession, m_y and m_z have the form:

$$
\begin{aligned}
m_y &= m_{y0} e^{i\omega t + \varphi_y} \\
m_z &= m_{z0} e^{i\omega t + \varphi_z}
\end{aligned}
\tag{2.21}
$$

The precession frequency is then obtained by substituting Eq. (2.21) into Eq. (2.20). The frequency expression is given in Eq. (4.1) and (4.2) in chapter 4.

For large angle precession, such first order approximation is not valid and a numerical simulation is required to depict the precession motion of the magnetization.

Reproduced with permission of the copyright owner. Further reproduction prohibited without permission.

2.3.2 Experimental setup

Figure 2.8 shows a schematic TR-MOKE setup used in this dissertation. A commercial Ti:sapphire regenerative amplifier system (Spectra-Physics) provides 150-fs laser pulses with a center wavelength of 800 nm and a repetition rate of 1 KHz. The laser beam is split into pump and probe beam by a beam splitter. The pump beam is focused on the sample at normal incidence. After passing through a delay line, the plane-polarized probe beam is focused on the same region of the sample at an incident angle of 45°. The reflected probe beam then passes through an analyzer set at crossed polarization with respect to the incident plane of polarization.

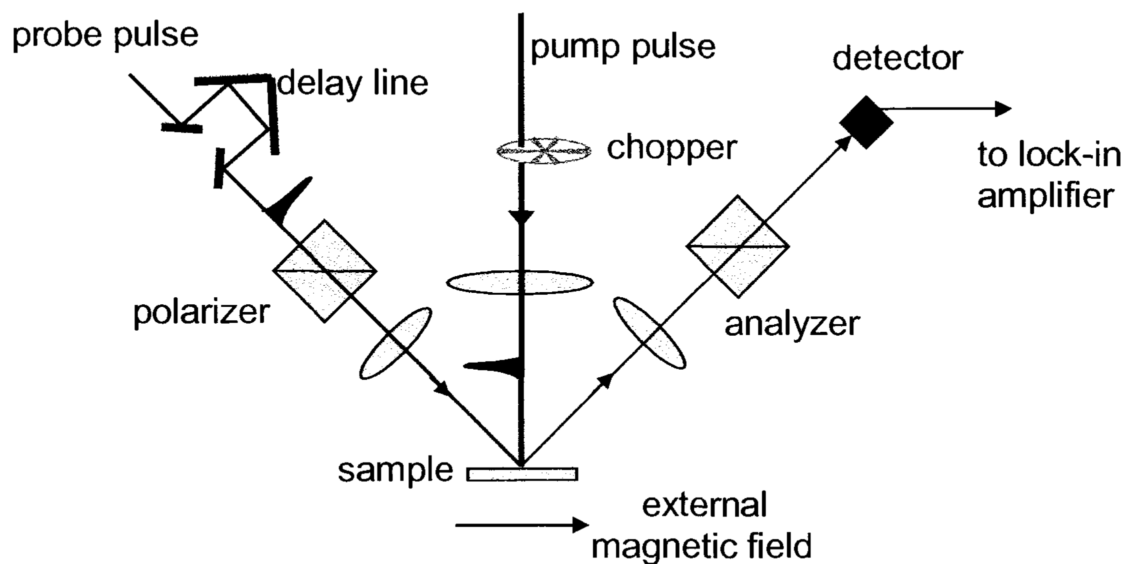

Fig. 2.8: Sketch of the time-resolved MOKE setup.

The signal detection in the transient MOKE measurement is depicted schematically in Fig. 2.9: (a) Pump beam is blocked: the probe pulses are detected with a

Reproduced with permission of the copyright owner. Further reproduction prohibited without permission.

photodiode generating current pulses with peak intensity I_o, corresponding to the orientation and modulus of the magnetization at equilibrium. The pulsed photocurrent is converted to a DC signal (bottom panel) by a gated integrator and boxcar averager, which eliminates the void signal and noise. (b) The pump beam is unblocked: the pump beam induces a change of the magnetization, altering the intensity of the time-delayed probe beam that passes through the analyzer, which is represented by $I_{\Delta t}$ at a time delay Δt with respect to the pump beam. (c) To measure the intensity difference I_o- $I_{\Delta t}$ (typically small) by the lock-in amplifier, the pump beam is modulated by a chopper to cause the intensity of the probe beam to alternate at the modulated frequency. A time-resolved MOKE spectrum is then obtained by sweeping the delay time.

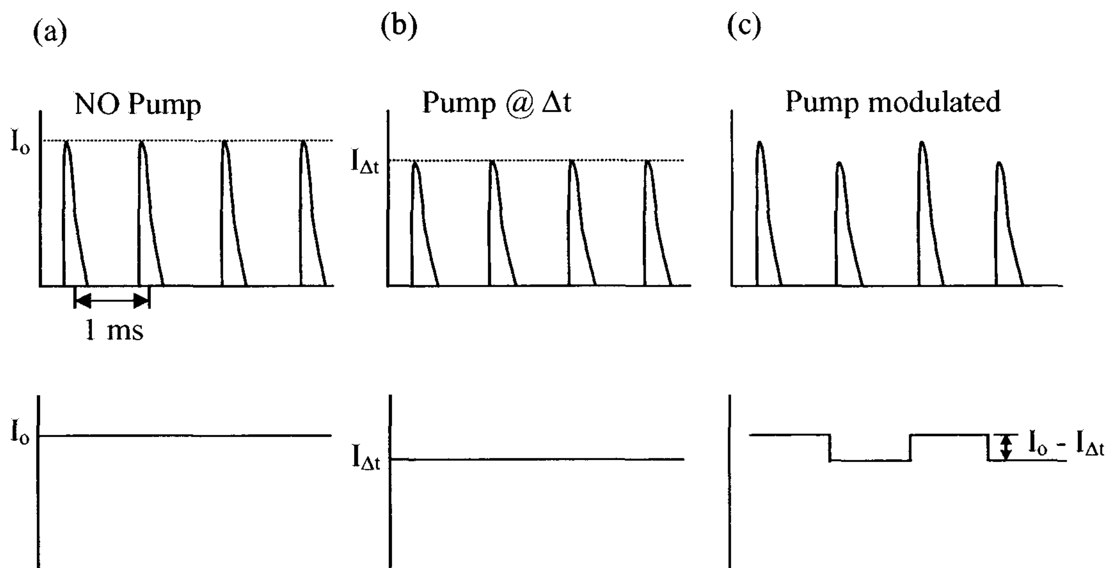

Fig. 2.9: Schematic diagram of transient MOKE signal detection in TRMOKE experiments. The top and bottom panels indicate the pulsed photocurrent from the detector and signal after gated integrator and boxcar averager.

Reproduced with permission of the copyright owner. Further reproduction prohibited without permission.

Similar to the TR-MOKE technique, TR-MSHG exploits an ultrafast pump beam to trigger the magnetization dynamics of a medium, which is then tracked in the time-domain by a time-delayed probe beam (Fig. 2.10). However, a special detection system is required to measure the SHG which is much weaker than the fundamental light reflected from the sample.

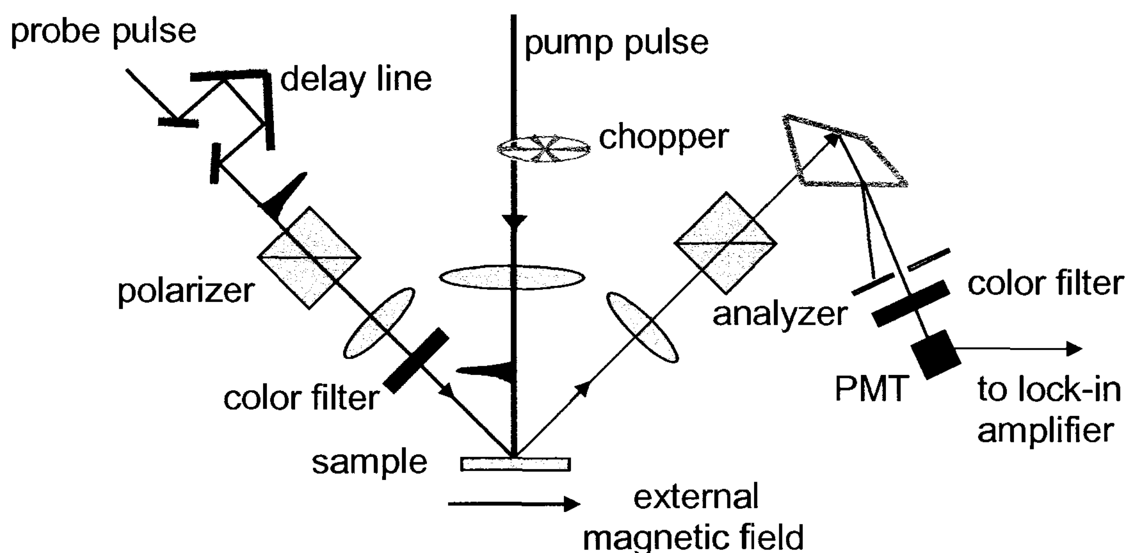

Fig. 2.10: Sketch of time-resolved MSHG setup.

Several features in the TRMSHG setup, shown in Fig. 2.10, need to be highlighted, which are important to accomplish such measurements. First, a color filter is put in front of the sample to eliminate the SH light, generated from the laser system and optics, from the fundamental light of the probe beam. Thus, only a beam with pure fundamental light is incident on the sample and interacts with it. Second, the reflected beam from the sample passes through a prism separating the propagation directions of the

Reproduced with permission of the copyright owner. Further reproduction prohibited without permission.

fundamental light and SHG generated from the sample. Third, the fundamental light needs to be blocked, and the SHG passes through another color filter eliminating the scattered fundamental light and illuminates on a photomultiplier tube. The current produced by the PMT is amplified by a low-noise current amplifer (SR250), and then integrated and fed into the lock-in amplifier.

2.4 Internal Photoemission (IPE)

Internal photoemission (IPE) refers to absorption of photons which results in electronic transitions from the occupied states of a material (emitter) to the empty states of another (collector). The most common example is the excitation of electrons near the Fermi energy of a metal to the (unoccupied) conduction band of an adjacent semiconductor by absorbing visible or infrared photons to overcome the energy barrier (Fig. 2.11), producing a steady state photocurrent across the barrier interface. This process is termed internal photoemission in analogy to standard photoemission where the transition is between occupied states of a material and the vacuum level. IPE is a powerful method to measure barrier heights in metal-semiconductor Schottky diodes [44], complementing the more commonly used currentvoltage (*I-V*) and capacitance-voltage (*C-V*) techniques. In addition to measuring metal-semiconductor barrier heights, IPE has been used to measure band alignment between semiconductor electrodes and semiconductor or insulators [45].

Reproduced with permission of the copyright owner. Further reproduction prohibited without permission.

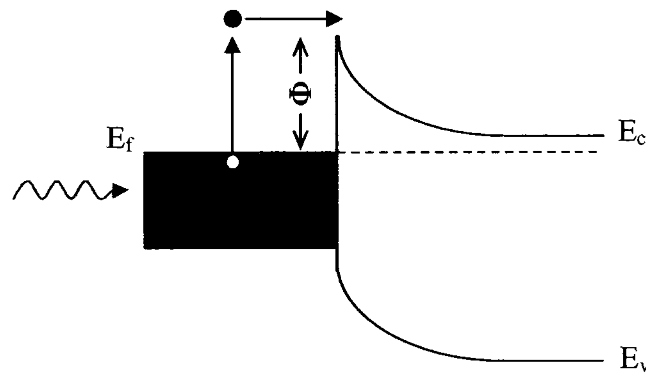

Fig. 2.11: Schematic of internal photoemission from a Fermi surface to a conduction band of a semiconductor. Φ is the energy barrier across the interface.

Internal photoemission is usually described with Fowler theory [46], in which the internal quantum efficiency Y (quantum efficiency per absorbed photon) is given by

$$Y=(h\nu - \Phi)^r , \tag{2.22}$$

where Φ is the barrier height and $h\nu$ is the photon energy. The value of r depends on the transition generating the energetic electron and the scattering process involved [47].

In spite of the neat experimental design, a strong infrared light source is required to produce a large photocurrent measurable with high signal to noise ratio. Recently, a Free Electron Laser (FEL) was used to measure the band discontinuity of semiconductor heterostructures with high accuracy [48,49].

In this dissertation, a table-top experimental setup is developed to perform the IPE measurements by utilizing an optical parametric amplifier as the bright light source. In the following the experiment setup and the laser system are described in detail.

IPE Experimental Setup - A schematic diagram of the IPE is shown in Fig. 2.12. The laser system consists of a Ti:Sapphire regenerative amplifier (Spitfire, Spectra-

Reproduced with permission of the copyright owner. Further reproduction prohibited without permission.

Physics) and an optical parametric amplifier (OPA-800C, Spectra-Physics). The OPA beam delivers 150 fs pulses with a 1 KHz repetition rate tunable from 10 μm to 600 nm (see Fig. 2.13). The top layer of sample is connected to a low noise current amplifier and the substrate is held at ground. The photocurrent is measured continuously as a function of wavelength, and the signal of the amplified photocurrent pulse is recorded on a digital oscilloscope triggered by the laser repetition frequency. The photocurrent is estimated from the time integral of the current pulse utilizing a gated integrator and boxcar averager.

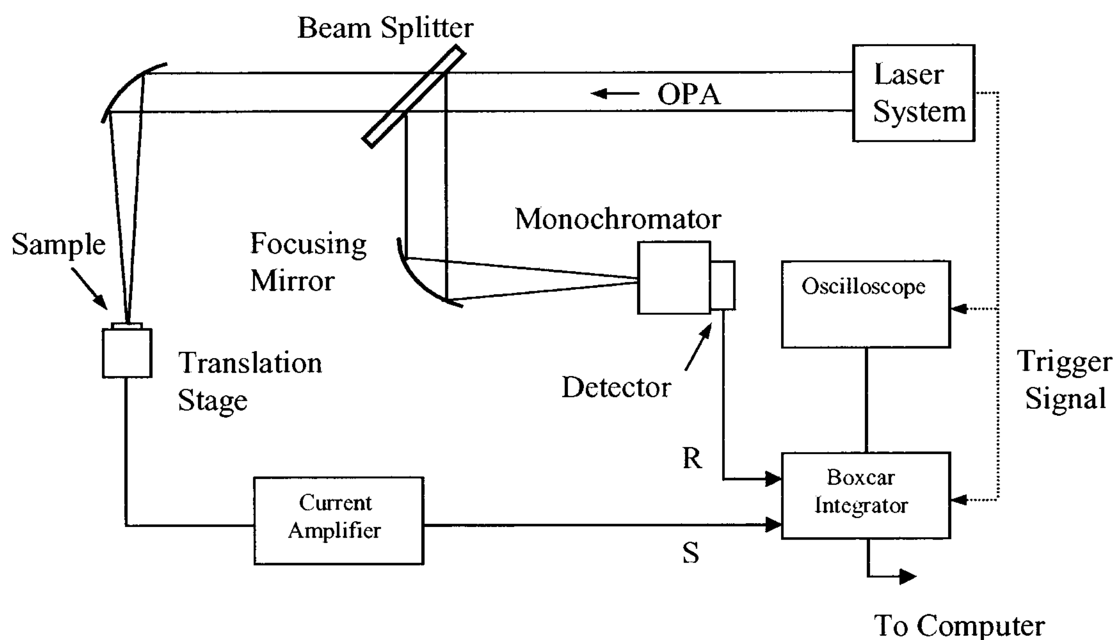

Fig 2.12: Experimental setup for band offset measurement of semiconductor heterostructures.

Laser system - The Ti:Sapphire amplifier generates 150-fs laser pulses with a center wavelength of 800 nm and a repetition rate of 1 KHz. The OPA system converts the 800 nm pulses to longer wavelengths through a type-2 OPA process. The system uses

Reproduced with permission of the copyright owner. Further reproduction prohibited without permission.

a BBO crystal as the nonlinear medium. The output pulses are tunable in the range 1140-1600 nm (signal) and 1600-2650 nm (idler). Furthermore, a special cut BBO crystal and $AgGaS_2$ crystal provide the second-harmonic and different-frequency mixing (DFM) of the signal and idler beams (600 -1150 nm, 3-10 μm). The OPA tuning curves are shown in Fig. 2.13.

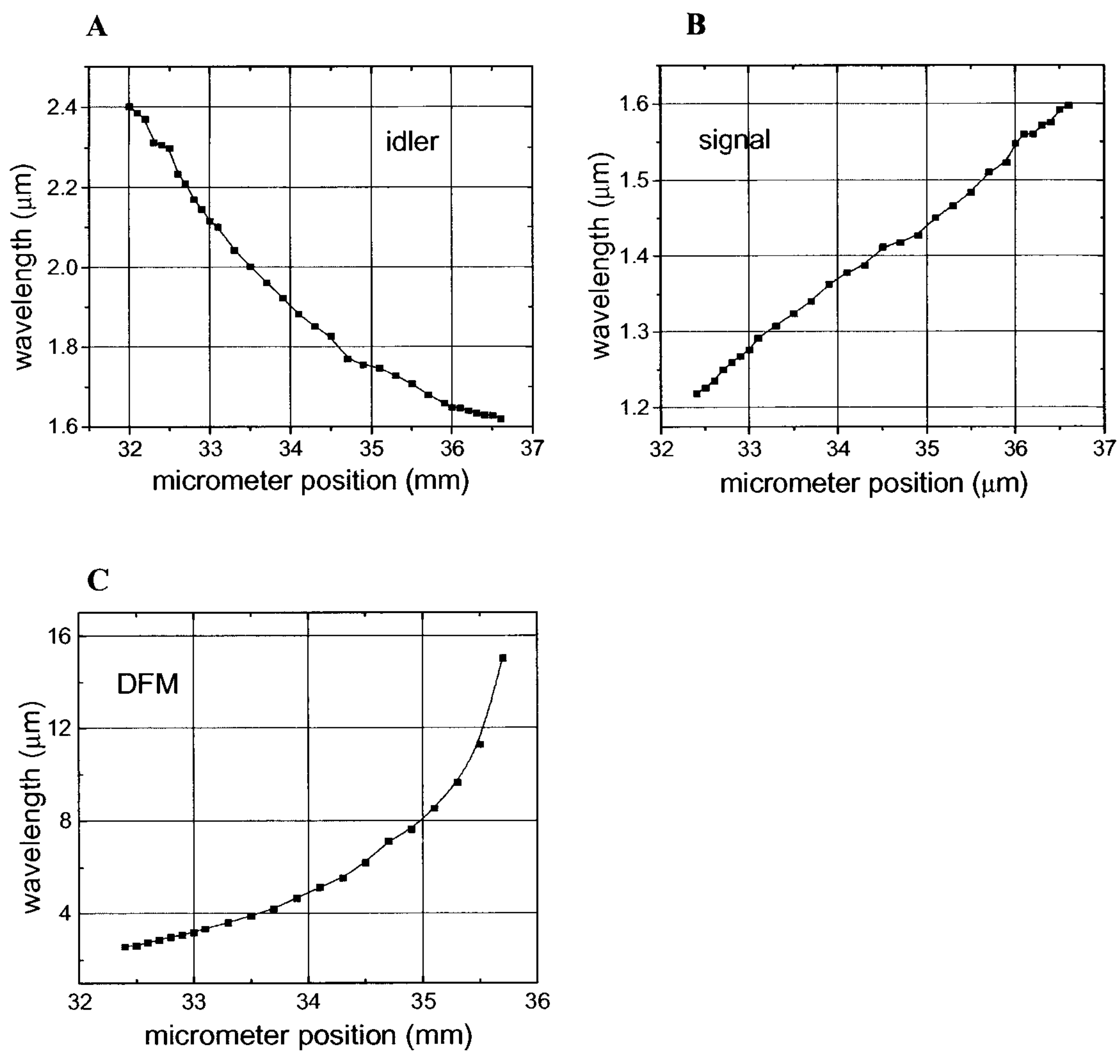

Fig 2.13: The OPA wavelengths vs BBO tuning position.

Reproduced with permission of the copyright owner. Further reproduction prohibited without permission.

Chapter 3

Interface magnetization reversal and anisotropy in Fe/AlGaAs

The reversal process of the Fe interface layer magnetization in Fe/AlGaAs heterostructures is measured directly using magnetization-induced second harmonic generation, and is compared with the reversal of the bulk magnetization as obtained from magneto-optic Kerr effect. The switching characteristics are distinctly different in Fe/AlGaAs (001) – single step switching occurs at the interface layer, while two-jump switching occurs in the bulk Fe for the magnetic field orientations employed. The different switching processes lead to a deviation angle of 40-85° between interface and bulk magnetization at given fields. This behavior may result from reduced exchange interaction in the direction normal to the interface and different magnetic anisotropies at the heterojunction. In contrast to Fe/AlGaAs (001), the interface magnetization in Fe/AlGaAs (110) is rigidly coupled to the bulk Fe. The different behavior reveals large influence of the interface bonding configuration on the magnetic character despite similar chemical composition of both interfaces. .

3.1 Introduction

Ferromagnetic metals offer most of the properties required for practical spin injection contact materials: high Curie temperature, low coercive field, and high spin

Reproduced with permission of the copyright owner. Further reproduction prohibited without permission.

polarization of electrons at the Fermi level. In addition, metallization is a standard process in any semiconductor device fabrication line, so that the use of a ferromagnetic metal and semiconductor heterostructure could easily be incorporated into existing technology processes.

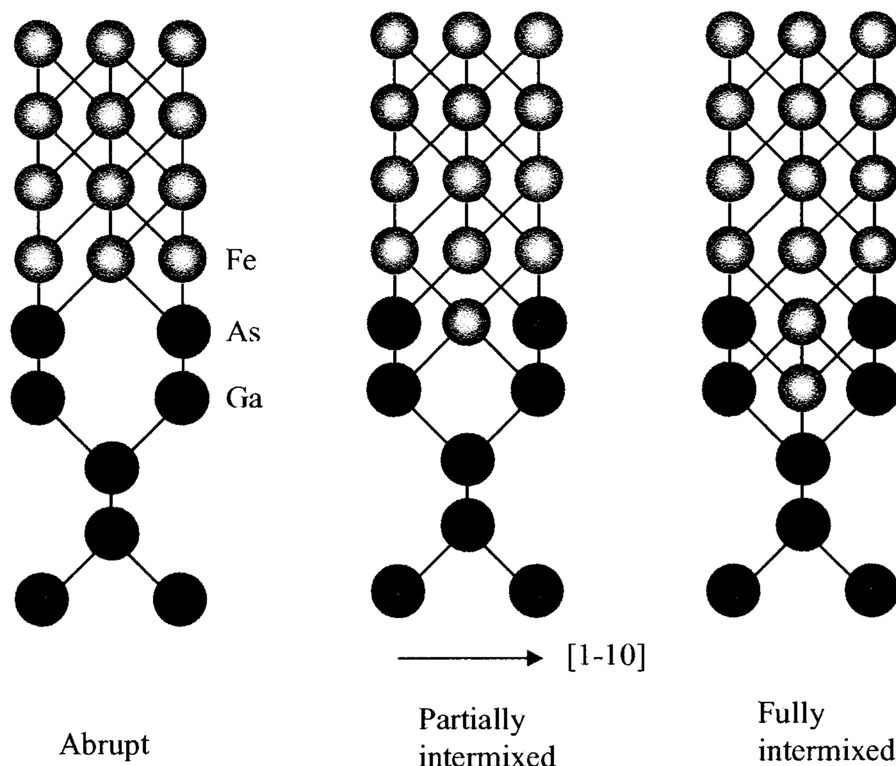

Fig. 3.1: Interface structure for the As-terminated Fe/GaAs (001). [51]

Among the various FM/S spin injection heterostructures, a single-crystal Fe film on GaAs substrate is particularly promising because of the large injected electron spin-polarization of 32% demonstrated in a Fe/AlGaAs (001) Schottky contact [50]. Tunneling electron microscopy reveals a well defined interface due to the small lattice mismatch

Reproduced with permission of the copyright owner. Further reproduction prohibited without permission.

(~1.3%). Several possible interface chemical structures (Fig. 3.1) have been discussed by Erwin *et al.* [51] and a partially intermixed interface was recently proposed in the low temperature annealed sample based on Z-contrast microscopy images. The correlation between the spin injection efficiency and chemical structure at the heterointerface reveals that a chemically ordered interface is helpful to reduce the spin scattering of the tunneling electrons.

Further improvement of spin injection, however, requires a detailed understanding of the magnetic properties at the heterointerface, since the spin-polarized density of states at the interface is of critical importance in spin-dependent tunnel experiments. In fact, interface driven magnetic interactions often lead to differences in magnetic characters between interface and bulk layers, manifested as changes in magnetic anisotropy, magnetic moment, or spin orientation. In ferromagnetic thin films, such differences are generally small owing to uniform environment and large exchange coupling along the vertical direction. However, distinct differences in chemical environment and structure at an interface may cause large changes in magnetic characters, leading to noncollinearity between the bulk and interface magnetization [52,53]. Since the discontinuity in chemical environment is typical for all metal-semiconductor interfaces, it is highly desirable to develop an approach to directly investigate its impact on the magnetic properties.

3.2 Interface magnetization reversal and magnetic anisotropy in Fe/AlGaAs (001)

Reproduced with permission of the copyright owner. Further reproduction prohibited without permission.

Very thin Fe (001) films exhibit an unusual in-plane uniaxial component to the magnetic anisotropy, such that the easy axis is along [110] for films <15 monolayers (~ 21 Å) thick [54]. This is dramatically different from the cubic magnetic anisotropy of bulk bcc Fe which has <100> easy axes. A detailed study of Fe films grown on well-characterized GaAs(001) surfaces prepared by molecular beam epitaxy (MBE) attributed this behavior to an interface contribution derived from the directional character of Fe-As bonding [54], corroborating the original hypothesis of Krebs et al. [55]. It was argued that this Fe-As bonding is common to the interface which ultimately forms, regardless of the initial GaAs(001) surface reconstruction [56]. Further evidence for this picture was provided by x-ray absorption studies, which showed that Fe *3d* charge transfer at the interface was independent of GaAs substrate preparation and orientation [57].

Such a uniaxial magnetic anisotropy (UMA) component profoundly affects the magnetization reversal process, leading to "one-jump" or "two-jump" switching depending on the orientation of the applied field and the hard in-plane axis resulting from the UMA [36,58-60]. More recent work has shown that the shear strain introduced from anisotropic relaxation of the Fe lattice for films thicker than 20 Å produced a strain anisotropy which competes with the interface derived contribution, significantly modifying the overall behavior [61]. Nevertheless, a fundamental understanding of the evolving magnetic anisotropy remains elusive owing partially to the lack of direct information of the magnetization reversal process for interface Fe layers in real films.

Here, MSHG is applied to directly study the interface magnetization reversal process in Fe/AlGaAs (001). Samples were grown by molecular-beam epitaxy (MBE) using interconnected growth chambers in Dr. Berend Jonker's group at NRL. The top

Reproduced with permission of the copyright owner. Further reproduction prohibited without permission.

150-Å of n-type AlGaAs was highly doped to form narrow Schottky barrier. The 100-Å thick single crystalline Fe films were grown at <15°C to minimize potential intermixing at the interface [50]. The MSHG measurement is performed in longitudinal geometry with a nearly ideal s-polarized input light and s-polarized SHG mixed in p-polarized component at a constant analyzer angle $\alpha = 6^{o}$. At this angle M-H loops can be obtained with very high sensitivity and high signal to noise ratio.

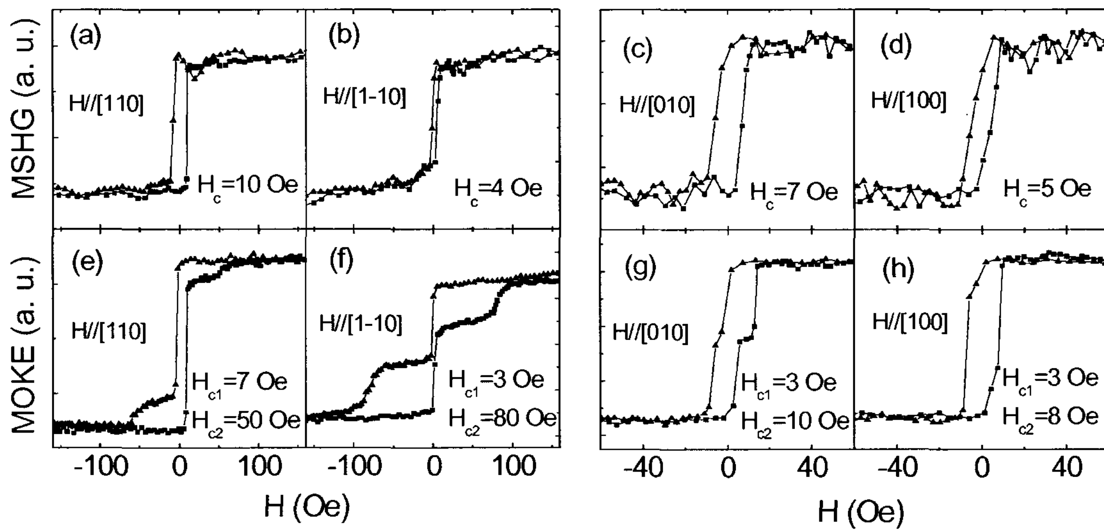

Fig. 3.2: Longitudinal MSHG, (a) – (d), and MOKE, (e) – (h), *M-H* loops from 10-nm Fe (001) film with the field applied along the principal crystallographic axes [110], [1-10], [010], and [100], respectively. The squares (triangles) indicate increasing (decreasing) magnetic field. The coercive fields are listed in each panel.

The top panel in Fig. 3.2 shows a set of typical MSHG magnetization curves for the 10-nm Fe (001) film with the magnetic field applied along the different crystallographic directions indicated. For comparison, we plot MOKE magnetization curves in the bottom panel. The most striking difference between MSHG and MOKE *M-H* loops is the switching behavior of the magnetization reversal process. In the case of the

Reproduced with permission of the copyright owner. Further reproduction prohibited without permission.

MSHG curves, one-jump switching is observed for all principal crystallographic axes (Figs. 3.2 (a) – (d)). In contrast, the MOKE *M-H* loops exhibit distinct plateaus and two switching fields, revealing a two-jump reversal process (Figs. 3.2 (e) – (h)). The difference in the magnetization reversal process is particularly apparent for the hard axis [1-10] as shown in Figs. 3.2 (b) and (f). These data reveal that the magnetization of the interface layer switches in a manner which is distinctly different from that of the bulk, and is not rigidly locked to the bulk by the strong exchange coupling typically associated with ferromagnetic metals.

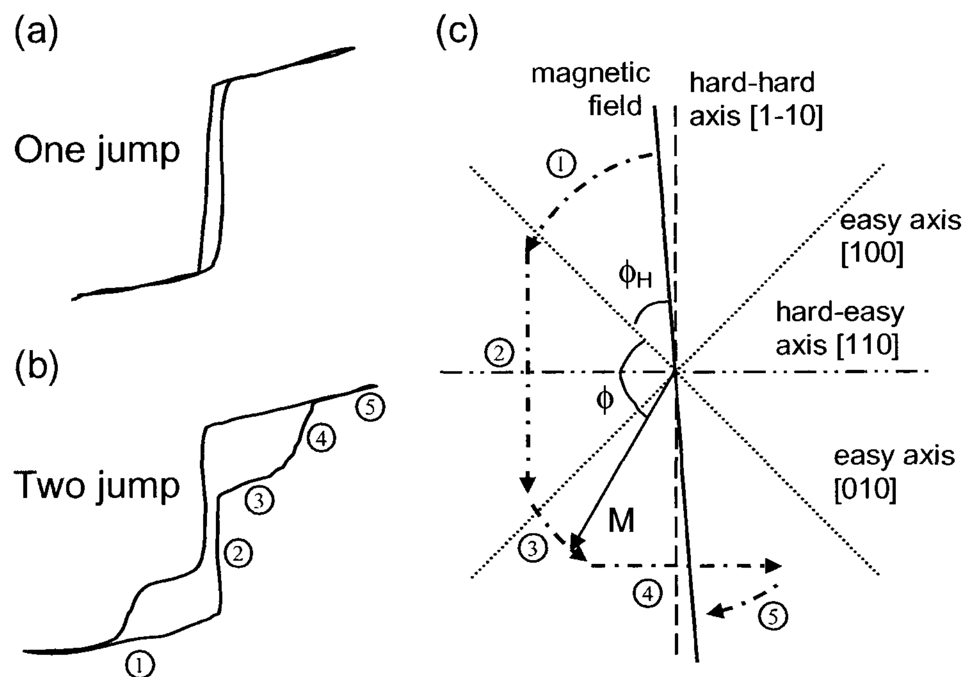

Fig. 3.3: (a) *M-H* loop for one-jump switching; (b) *M-H* loop for two-jump switching; and (c) sequence of the two-jump process. The numbers relate the steps in the sequence to the corresponding feature in the *M-H* loop.

Reproduced with permission of the copyright owner. Further reproduction prohibited without permission.

The reversal process of the thickness-averaged (macroscopic) magnetization in the Fe/GaAs (001) system has been studied in detail [58-60], and the mechanisms are summarized in Figs. 3.3 (a) – (c) using the terminology of ref. [60]. One-jump switching occurs when *M* is first pulled over ("jumps") the hard-hard axis, and thus has sufficient energy to immediately rotate over the hard-easy axis. This produces the conventional looking *M-H* loop of Fig. 3.3 (a). This switching occurs for all crystallographic directions when the uniaxial anisotropy is stronger than the cubic anisotropy, i.e., $|r| \geq 1$ [59,60]. Hence, our MSHG data show that the anisotropy at the AlGaAs interface is dominated by the UMA contribution.

Two-jump switching occurs when *M* is first pulled over the hard-easy axis, but lacks sufficient energy to cross the hard-hard axis (Fig. 3.3 (c)). As the magnitude of the reversed applied field increases further, the second jump occurs when *M* rotates through this hard-hard axis. These two jumps result in intermediate plateaus or kinks in the *M-H* loop and two distinct switching fields (Fig. 3.3 (b)). One important point about this mechanism is that it requires two distinct hard axes in the plane of the sample. This condition only arises when the ratio of uniaxial to cubic anisotropy ($r = K_u/K_1$) is less than unity [59,60].

We determined an anisotropy ratio $|r| = 3.5$ for the interface magnetization, and $|r| = 0.4$ for the bulk magnetization [62] from coherent magnetization precession measurements (discussed in the next chapter), indicating that the switching processes are in very good agreement with the predictions based on the coherent rotation model [59,60].

A quantitative analysis of the magnetization curves shown in Figs. 3.2 (b) and (f) reveals that the deviation angle θ between bulk and interface magnetization is in the

Reproduced with permission of the copyright owner. Further reproduction prohibited without permission.

range 40°-85° between the first and second switching step. This is because the bulk magnetization switches first to the easy [100] axis, as shown in Fig. 3.3(c), whereas the interface magnetization switches directly to the easy [010] axis.

In a uniform ferromagnetic thin film, the strong exchange coupling $A \cong 10^{-11}$ J/m tends to maintain the interface spins quasi-parallel to the spins in the bulk of the film. Thus a magnetization twisted region may exist. The thickness of this twisted spin region (exchange length l_c) varies for different materials. For Fe, the large magnetostatic energy quickly reorients the spins from out-of-plane to in-plane, leading to a transition region on the order of 3 nm. In contrast, the magnetocrystalline/magnetoelastic anisotropy energy density K_c is much smaller, so the in-plane reorientation requires a much thicker transition region. The variation of in-plane magnetization orientation with distance from the interface can be described by [63]:

$$\theta(z) = \arctan\left[\sinh\left(\frac{a_0 + z}{l_c}\right)\right], \tag{3.1}$$

where the exchange length $l_c = (A/K)^{1/2}$. The parameter a_0 is given by:

$$\tanh\left(\frac{a_0}{l_c}\right) = \frac{\sqrt{A \cdot K_c}}{K_s}, \tag{3.2}$$

where K_s is the interface anisotropy. The black curve in Fig. 3.4 shows the deviation angle $\theta(z)$ for $K_s = 2.5$ erg/cm^2 and characteristic values of $A=1.0\times10^{-6}$erg/cm and $K_c = 4.0\times10^{5}$erg/cm^3 of bulk Fe. In this case, the deviation angle between bulk and interface spins would be less than 10 degrees for a 10-nm thick Fe film. Such a small magnetization deviation angle can not explain the present experimental results. The magnetization reorients in a much thinner layer for reduced exchange coupling strength, as shown in Fig. 3.4, implying a reduced value of A for the interface layers.

Reproduced with permission of the copyright owner. Further reproduction prohibited without permission.

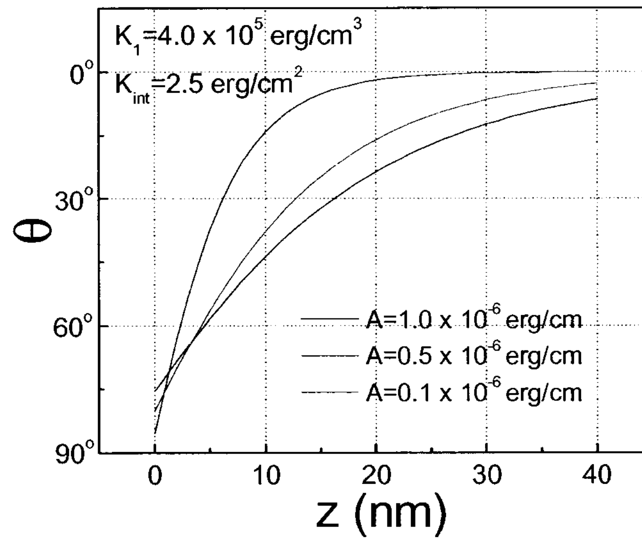

Fig. 3.4: Variation of in-plane magnetization orientation with distance from the interface according to Eq. (3.1).

The assumption of a constant interlayer exchange coupling strength might not be true for layers with different lattice parameters, bonding environment and magnetic character. A different magnetic interaction at the interface could dramatically reduce the exchange coupling and cause the abrupt change of switching characteristics. Gordon *et al.* found a body-centered tetragonal distortion in a 9 ML thick Fe film on GaAs (001) [64]. The measured distortion involves an in-plane contraction and an out-of-plane expansion. This structural anisotropy could dramatically affect the magnetic anisotropy and reduce the exchange coupling normal to the planes. In addition, small variation of the Fe-As bonding may also affect the magnetic phase of the Fe interface layer. Fe-As *pd* hybridization has been shown to affect (quench) the Fe magnetic moment and the exchange coupling as illustrated in theoretical calculation [51,65]. Therefore, we propose that the specific bonding and structure at the Fe/AlGaAs interface may lead to a different

Reproduced with permission of the copyright owner. Further reproduction prohibited without permission.

magnetic interaction and exchange coupling of the Fe interface layer with respect to the bulk spins.

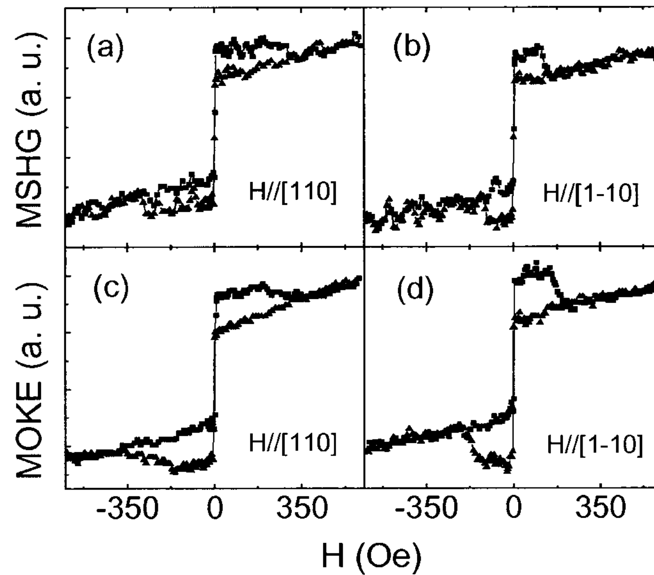

Fig. 3.5: Longitudinal MSHG, (a) and (b), and MOKE, (c) and (d), *M-H* loops from the 50-nm Fe film capped with a 5 nm Cr layer with the field applied along the hard-easy [110] and hard-hard [1-10] axes, respectively. The squares (triangles) indicate increasing (decreasing) magnetic field.

For comparison, we utilized the MSHG technique to probe the magnetic anisotropy of the Fe/Cr interface. A 50-nm thick Fe film grown on AlGaAs and capped with a 5-nm Cr layer was used for this experiment. The large Fe thickness eliminates the MSHG signal from the Fe/AlGaAs interface because of the short absorption depth (~20 nm) of the MSHG signal at 400-nm wavelength. The *p*-input polarization and *s*-polarized MSHG signal (Figs. 3.5 (a) and (b)) provides the best signal-to-noise ratio. Figure 3.5 shows a set of typical longitudinal MSHG (top panel) and MOKE (bottom panel)

Reproduced with permission of the copyright owner. Further reproduction prohibited without permission.

magnetization curves with the magnetic field applied along the hard <110> crystallographic directions. Both the MSHG and MOKE *M-H* curves clearly show a two-jump reversal process, in contrast to the switching behavior of the 10-nm Fe film. We determined an anisotropy ratio $|r| < 0.1$ from coherent magnetization precession measurements, indicating a very small UMA contribution at this interface. A two-jump reversal process for this value of $|r|$ is again in very good agreement with the predictions of the coherent rotation model [59,60]. These results clearly indicate that the Fe/Cr interface contributes a negligible UMA component. The MSHG and MOKE *M-H* loops of Fig. 3.5 both exhibit an "overshoot." This effect can be attributed to an optical effect caused by "mixing in" a small contribution from the transverse magnetization [36].

3.3 Interface magnetization reversal and magnetic anisotropy in Fe/AlGaAs (110)

The value of spin injection measured in the surface emitting spin-LED represents a lower bound to the initial injected spin polarization, since the value of spin polarization measured is limited by the spin lifetime of the carriers. Previous studies have reported longer spin lifetimes in optically pumped GaAs (110) quantum well structures than for the (001) orientation and the (110) spin lifetimes increased at higher temperatures [66], making this orientation attractive for spin-LED.

However, The MBE growth of GaAs (110) is more challenging and less developed, which may result in lower material quality or a nonoptimized structure. In contrast to the typical layer-by-layer growth mode on a (001) face, a pronounced three-dimensional clustering was observed for growth on the (110) face [67]. Recent

Reproduced with permission of the copyright owner. Further reproduction prohibited without permission.

experiments, however, report a two dimensional growth, but with a surface roughness of typically 5 Å [68]. Moreover, the free (110) surface is composed of zig-zag ridges of As and Ga running parallel to [1-10] with voids between the ridges, so that not all Fe atoms will be equivalently bonded to the surface, regardless of the centering of the Fe atoms (above the Ga-As bonds; above Ga or As atoms; or in surface depressions). No evidence of Fe-induced surface reconstruction is found on this surface, which is in contrast to the (001) surface, where the Fe atoms displace the sub-monolayer of As surface dimers and the first monolayer of Ga atoms to form a uniform Fe/As interface [54]. Such differences of electronic structures between the two interfaces may lead to different magnetic properties of Fe interfacial layers.

In epitaxial Fe (110) films grown on single crystal (110) oriented GaAs substrates, previous investigations found a reorientation transition of the magnetic easy axis of the magnetization from the [1-10] to [001] axis with increasing film thickness [69,70]. Such evolution arises from a combination of uniaxial in-plane magnetic anisotropy and the cubic anisotropy. The total magnetic anisotropy density can then be written as:

$$F^{(110)} = \frac{1}{4}K_1(t)(\frac{3}{4}\sin^2(2\varphi) + \sin^2\varphi) + K_u(t)\sin^2\varphi \tag{3.3}$$

where t is the thickness of the Fe film. In Fig. 3.6, $F^{(110)}$ is plotted qualitatively as function of the in-plane angle φ for different ratio r with $K_1(t) > 0$. Up to the critical anisotropy ratio $r_c = -0.25$ the absolute minimum is at φ=90°, which means the easiest axis is along the [1-10] direction. A second local minimum appears at 0° for r>-1 which makes the [001] direction an intermediate axis. For r>-0.25, the absolute minimum is at φ=0° which means the easiest axis is along [001] direction as in bulk Fe. The local minimum now at 90° makes the [1-10] direction an intermediate axis.

Reproduced with permission of the copyright owner. Further reproduction prohibited without permission.

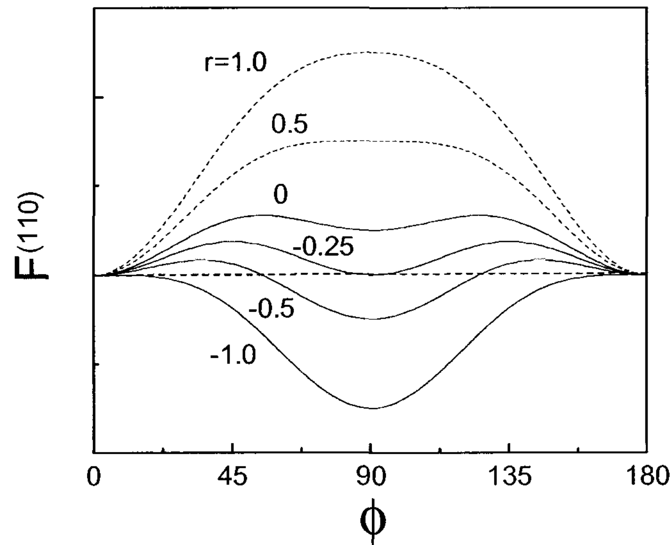

Fig. 3.6: The in-plane anisotropy energy density at zero field according to Eq. (3.3) for Fe (110) films with different anisotropy ratio $r=K_u/K_1$.

Since the switching behavior is strongly affected by the magnetic anisotropy, it is critical to directly probe the switching process of the interface Fe layer in a thick Fe film, where the bulk magnetic anisotropy is dramatically different from that of the film of a few monolayer. A direct comparison between interface and bulk magnetization switching along all in-plane crystallographic directions in 10 nm Fe (110) film is given in Fig. 3.7. We can see a very similar switching process between the two - an easy axis along the [1-10] direction with the same coercivity and a kink in the magnetization curves along the [001] direction. Such kink arises from a two-jump process with the first jump of the magnetization from a local minimum formed along an intermediate axis [001] to a global minimum appeared close to [1-10] direction, followed by a continuous rotation of the magnetization before its second jump to the opposite direction. The identical switching behavior and coercivities indicate a rigid coupling between the bulk and interface

Reproduced with permission of the copyright owner. Further reproduction prohibited without permission.

magnetization in Fe (110) film, in contrast to the decoupling between the two in Fe (001) film.

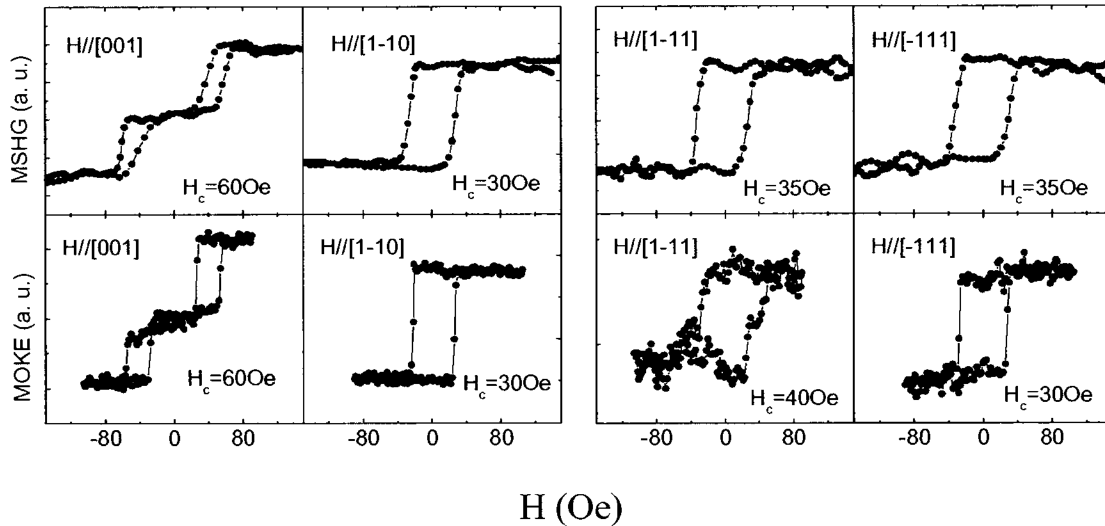

Fig. 3.7: Longitudinal MSHG and MOKE, *M-H* loops from 10-nm Fe (110) film with the field applied along the principal crystallographic axes [001], [1-10], [1-11], and [-111], respectively. The coercive fields are listed in each panel.

Such difference between Fe (001) and Fe (110) films implies that the bonding at the interface can dramatically change the exchange coupling strength. X-ray absorption studies of unoccupied 3d states of Fe reveal a large amount of charge transfer into the GaAs substrate, resulting in a $3d^5$ electron configuration of the Fe overlayer. Calculations show that $3d^5$ occupancy is near the crossover from ferromagnetic to antiferromagnetic order. In addition, the Fe lattice constant and structure can also affect the exchange energy. The differences in electronic structure between Fe/AlGaAs (110) and (001) caused by the different interfacial lattice positions of Fe atoms and the directionality of Fe-As bonding may lead to the large change of exchange coupling strength.

Reproduced with permission of the copyright owner. Further reproduction prohibited without permission.

3.4 Interface magnetization reversal in Fe/AlO/AlGaAs (001)

Tailoring the interfacial doping concentration of a semiconductor produces a narrow depletion layer and forms a triangle shaped tunnel barrier at the Fe/AlGaAs interface. Inserting a metal oxide is an alternative approach of forming a tunneling barrier to overcome the impedance mismatch between the magnetic metal and the semiconductor. Here, Al_2O_3 tunneling barrier was grown by oxidizing 10-Å of Aluminum deposited on AlGaAs layer in pure O_2 at RT. The 100-Å thick polycrystalline Fe film was then grown at 10-15 ^{o}C [71]. Since the Fe film is in direct contact with the oxide layer, it is important to study the effect of such barrier layer on the magnetic interaction of the Fe interface layer.

For this purpose, we have performed MSHG measurements to study the interface magnetization reversal process and to compare it to the bulk one, as shown in Fig. 3.8. The MOKE measurements show the presence of a small uniaxial anisotropy, which is possibly growth induced due to evaporation at a slightly oblique angle. The MSHG measurements reveal a ferromagnetic order for the interface magnetization, which exhibits not only a small uniaxial anisotropy, but also a variation of the coercive fields which may be caused by the texture being more pronounced at the interface since the Fe film deposited on the amorphous Al_2O_3 is polycrystalline. Such results clearly exclude a magnetic dead layer at Al_2O_3 interface due to its stable chemical structure. Indeed, a 40% percent spin polarization is observed in the optical active QW of the spin-LED structure [71] and only a few percent reduction of magnetic moment is reported for the interfacial Fe layer [72]. Therefore, such structure may prove to be an ideal system for comparison with theoretical models for the spin-dependent injection and detection.

Reproduced with permission of the copyright owner. Further reproduction prohibited without permission.

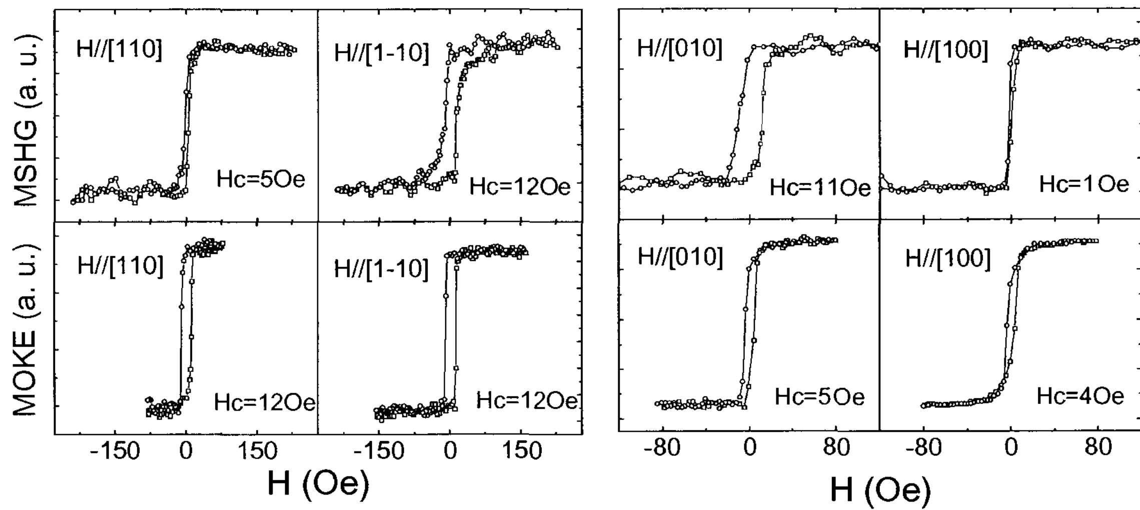

Fig. 3.8: Longitudinal MSHG and MOKE *M-H* loops in $Fe/Al_2O_3/AlGaAs$ (001) film with the field applied along the principal crystallographic axes [110], [1-10], [010], and [100], respectively. The squares (circles) indicate increasing (decreasing) magnetic field. The coercive fields are listed in each panel.

Summary

In this chapter, static MSHG is applied to study the interface magnetic interaction, anisotropy and magnetization reversal process in Fe films grown on AlGaAs substrates. Strong magnetization-induced effect is observed from the azimuthal dependence of SH intensity in such heterostructure interfaces, which directly excludes a magnetic dead layer and confirm the ferromagnetic order for the interface Fe layer. However, we find a pronounced difference in the reversal process of the bulk and interface magnetization in Fe/AlGaAs (001) – single step switching occurs at the interface layer, whereas two-jump switching occurs in the bulk Fe for the magnetic field orientations employed. The angle between the interface and bulk magnetization can be as large as 40° -85°, which is attributed to a decoupling of bulk and interface spins. This occurs as a consequence of the

Reproduced with permission of the copyright owner. Further reproduction prohibited without permission.

large difference in the magnetic anisotropy ratios arising from interface-induced contributions which we attribute to the specific bonding and structure at the Fe/AlGaAs (001) interface. In contrast, the interface magnetization in the Fe/AlGaAs(110) is rigidly coupled to the bulk one, indicating a strong exchange interaction of its interface layer with the bulk Fe. Our results show that MSHG is a powerful technique to probe interface magnetic properties in non-centrosymmetric hybrid structures as well as in centrosymmetric systems.

Reproduced with permission of the copyright owner. Further reproduction prohibited without permission.

Chapter 4

Time-resolved studies of spin precession in Fe/AlGaAs (001)

Ultrafast coherent precession of interfacial electron spins is observed in an Fe/AlGaAs (001) tunneling junction by TRMSHG. The spin precession of the interface magnetization is decoupled from the bulk Fe film, and exhibits a higher precessional frequency and opposite phase for a given applied field. This surprising result indicates that a faster magnetization switching can be achieved in nanostructures where interface properties dominate, and portends higher speed operation in future magnetic nanoscale devices.

Furthermore, uniform bulk magnetization precessions are generated by ultrafast optical excitation along the in-plane easy axis [100], as well as along the hard axis [1-10], in 10-nm Fe films grown on AlGaAs (001). From the temporal evolution of the coherent magnetization precession, the magnetic anisotropy constants and damping parameters are determined which are crucial in designing fast magnetic switching devices and novel spintronics devices. Low order spin wave modes as well as the uniform mode are observed in a 50-nm Fe film on AlGaAs (001), allowing an analysis of the exchange coupling and mode profile.

4.1 Introduction

The demand for ever-increasing speed at which information can be processed

Reproduced with permission of the copyright owner. Further reproduction prohibited without permission.

has triggered an intense search for ways to reduce the time for magnetization reversal to less than a nanosecond in ferromagnetic films used in magnetic media and devices such as random access memory. Thus understanding the underlying spin dynamics and developing new avenues for switching the magnetization are aggressively pursued areas of research. Recently discovered techniques include precessional magnetization reversal by ultrashort field pulsing [73] and current-induced switching by spin-momentum transfer [74]. Significant progress has been made in precessional switching, where timescales of a hundred picoseconds have been accessed. Recent work has shown that spin momentum transfer can drive magnetic reversal with switching times that are less than one nanosecond [75].

The large interface-induced magnetic anisotropy and the resulting noncollinearity between interface and bulk magnetizations [52,76] in Fe/AlGaAs (001) suggest that the *interface magnetization* can be manipulated and used rather than the bulk magnetization as the active layer for information storage/processing, with lower input power required for switching. The interface magnetization also plays a key role in the functioning of spintronic devices, which offer advanced performance and entirely new functionality [1,77,78]. Magnetic metal tunnel junctions are the basis of state-of-the-art magnetic random access memory and the read heads found in hard disk drives[79,80]. Thin ferromagnetic metal films have successfully been used to electrically inject spin-polarized current into a semiconductor heterostructure using a tunnel barrier approach [3,19,20,81]. Since the source term in spin tunneling is the spin polarization of the *interface density of states*, not the bulk polarization, the performance of these devices is strongly dependent on the magnetic properties of the heterointerface [28]. Hence,

Reproduced with permission of the copyright owner. Further reproduction prohibited without permission.

interface-selective probing of ultrafast magnetization dynamics is crucial for the design and realization of spin-electronic junction devices.

4.2 Interface magnetization precession

We trigger the interface magnetization precession utilizing the excitation mechanism introduced initially for bulk spin precession in a thin ferromagnetic metal film [82], as follows. A modulated pump beam with 50 μJ pulse energy is focused to a spot of 1.5 mm in diameter on the sample. In equilibrium, the interface magnetization is along an effective field H_{eff}. The incident pump pulse instantaneously heats up the film. The instantaneous lattice expansion changes the anisotropy of the film and induces a transient field H_{tr}. When H_{tr} has vanished, the vector M is rotated away from its original equilibrium orientation along H_{eff}. Therefore, it starts to precess around H_{eff}. A p-polarized time-delayed probe beam with 20 μJ pulse energy is incident on the sample at an angle of 45° as illustrated in Fig. 4.1(a). The reflected second-harmonic generation light passes through a crossed-polarization analyzer. In the longitudinal geometry with applied field along the in-plane hard axis [1-10], we detect the out-of-plane components of the precessing magnetization M at the interface.

Figure 4.1(b) shows the time-resolved MSHG signal after the excitation of Fe/AlGaAs in an applied magnetic field of 560 Oe along the in-plane hard axis [1-10]. The oscillations result from the precessional rotation described above. The Fourier transformation (see inset) yields a single frequency of ν = 5.8 GHz. The precession frequencies at different magnetic fields are plotted in Fig. 4.1(c) showing a strong field

Reproduced with permission of the copyright owner. Further reproduction prohibited without permission.

dependence, which clearly distinguishes this signal from potential non-magnetic interface contributions, e.g. phonons.

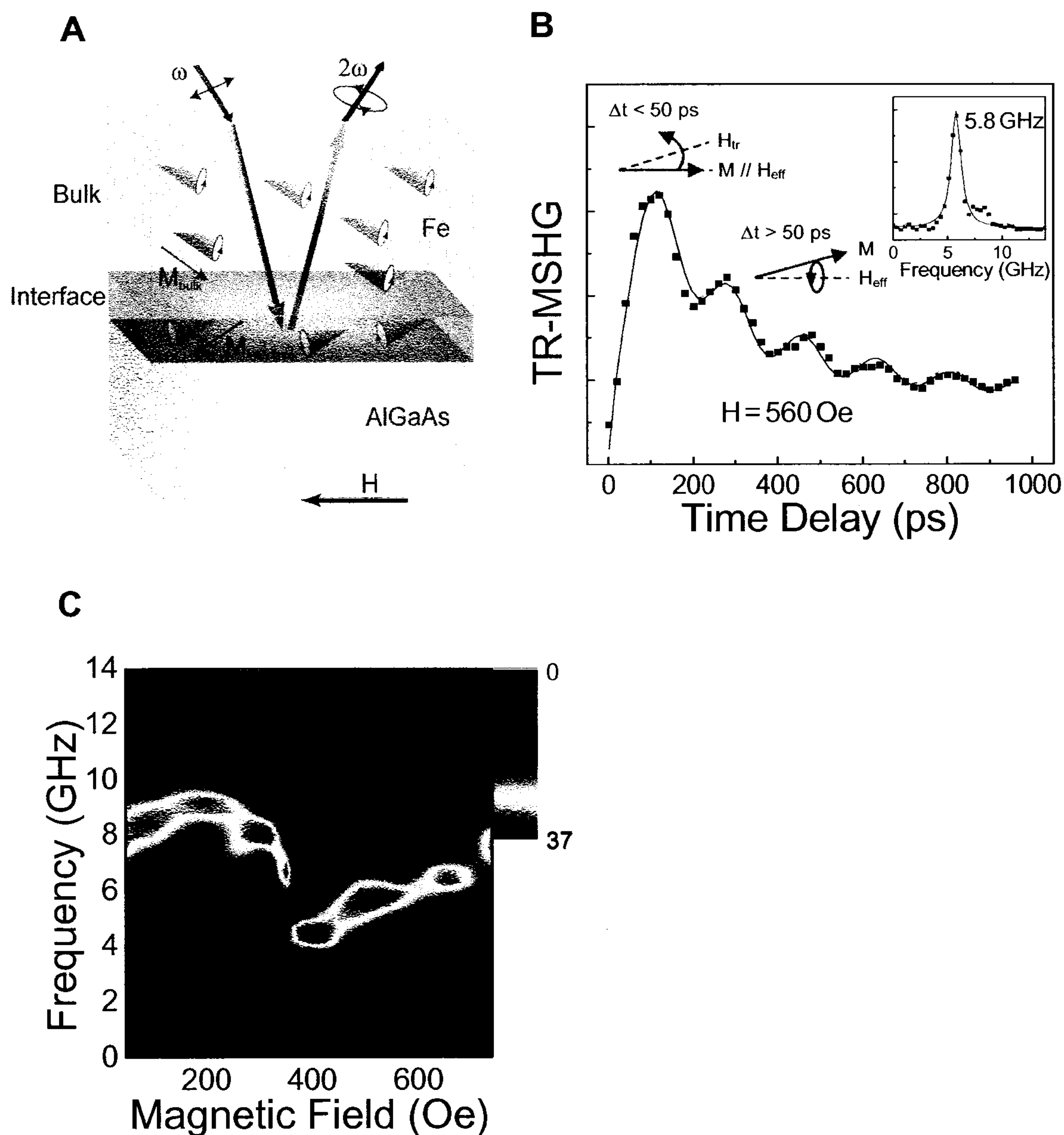

Fig. 4.1: (a) Experimental configuration. (b) Time-resolved MSHG signal after excitation with a magnetic field H=560 Oe applied along [1-10] direction. The inset shows the Fourier transformation. (c) Interface precession frequency at different magnetic fields along [1-10] direction.

Reproduced with permission of the copyright owner. Further reproduction prohibited without permission.

To fully understand the spin precession dynamics at the interface in Fe/AlGaAs, it is critical to obtain quantitative information on the magnetic anisotropies. The field dependence of uniform precession frequencies (Fig. 4.1c) allows us to determine these values. From the Landau-Lifshitz-Gilbert equation (2.14), the uniform precession frequencies can be described by

$$\omega = \gamma[(H_e \cos(\delta - \phi) + H^{\alpha})(H_e \cos(\delta - \phi) + H^{\beta})]^{1/2} \tag{4.1}$$

where

$$\begin{aligned} H^{\alpha} &= H_d + H_{\perp} - \frac{K_u}{M_s}(\sin\phi - \cos\phi)^2 - \frac{K_{//}}{M_s}\sin^2(2\phi), \\ H^{\beta} &= \frac{2K_{//}}{M_s}\cos(4\phi) + \frac{2K_u}{M_s}\sin(2\phi), \end{aligned} \tag{4.2}$$

and $\gamma = \gamma_e g/2$ (with $\gamma_e = 1.76 \times 10^7$ Hz/Oe and g = 2.09) is the gyromagnetic ratio. ϕ and δ are the angles between the in-plane easy axis [100] and the directions of magnetization and applied magnetic field H_e, respectively. K_u and $K_{//}$ are the in-plane uniaxial and cubic anisotropy constants, respectively. H_d and $H_{\perp}$ are the demagnetization and out-of-plane anisotropy field, respectively.

Figure 4.2 shows the interface and bulk precession frequencies as a function of magnetic fields. The red and black solid curves are the best fits for the interface and bulk precession, respectively, using Eq. (4.1). The fitting parameters are collected in Table 4.1, where H_d is determined from VSM measurements on the same sample. The results reveal a distinctly different ratio of in-plane uniaxial to cubic anisotropy $r = K_u/K_{//}$ between interface and bulk. A ratio of 3.5 is obtained at the interface, while a much smaller value of 0.4 is determined for the bulk. As a consequence, a two-step switching process in the

Reproduced with permission of the copyright owner. Further reproduction prohibited without permission.

bulk is expected from the coherent rotation model [59, 60], while single step switching occurs at the interface [76].

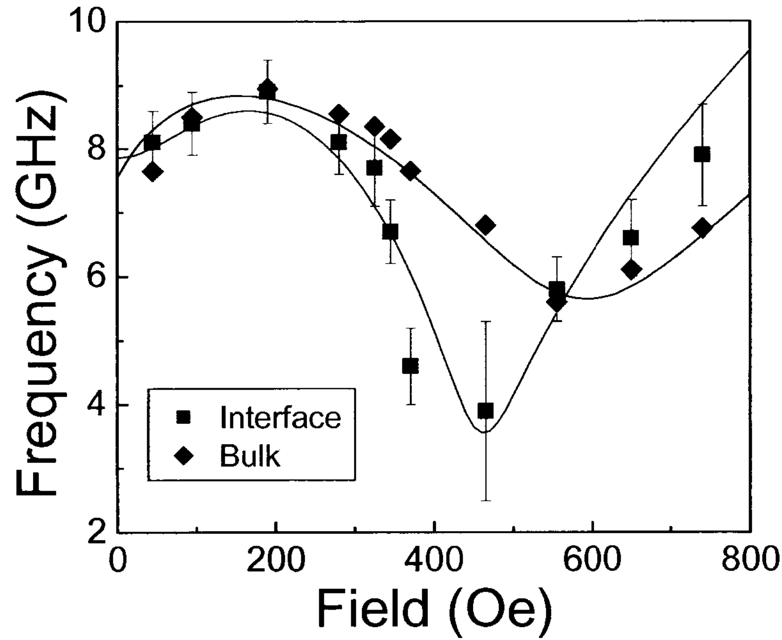

Fig. 4.2: Interface and bulk precession frequency versus applied magnetic field. The solid lines are the fits by Eq. (4.1).

Table 4.1: Anisotropy field values deduced from fits of Eq. (4.1) to the field dependence of the precession frequency at the interface and in the bulk.

	H_d (KOe)	$H_d + H_\perp$ (KOe)	$H_\perp$ (KOe)	$K_{//}/M_s$ (Oe)	K_u/M_s (Oe)
Interface	15.7	29	13.3	48	172
Bulk	15.7	18	2.3	200	70

Furthermore, we find a much larger out-of-plane field $H_d + H_\perp$ at the interface than in the bulk (Tab. 4.1). The demagnetization field is assumed to be the same for the bulk and the interface, H_d = 15.7 KOe, according to the recent report on the bulk-like

Reproduced with permission of the copyright owner. Further reproduction prohibited without permission.

magnetic moment of Fe interface layer on GaAs substrate measured by x-ray magnetic circular dichroism [83]. Hence $H_{\perp}$ is much larger at the interface than in the bulk. The sum of $H_{\perp}$ and H_d will determine the slope of the frequency-field dependence in the range of high fields. Figure 4.2 shows that after the precession frequency reaches the minimum it increases much more rapidly at the interface than in the bulk. The higher precession frequencies at the interface imply a faster switching of the interface magnetization in this thin film sample, as well as in nanostructures where interface properties dominate.

Figure 4.3 presents a comparison between interface and bulk spin precession dynamics at low fields applied along [1-10] direction and the impact of the different switching processes. The hysteresis loop in Fig. 4.3 (a) measured by static MSHG shows a single-step magnetization switching at +/- 4 Oe corresponding to a jump over the uniaxial hard axis. Therefore, the interface magnetization is reversible in the range of positive field (H > 4 Oe) or negative field (H < -4 Oe), where it stays between the [010] easy axis and the [1-10] hard axis. The reversal sequence of the magnetization vector is illustrated in Fig. 3.3. The red curve in Fig. 4.3 (b) represents the interface magnetization precession dynamics measured at a field of 72 Oe sweeping down from positive high field, and the black curve is taken at the same field but sweeping up from negative high field. The two measurements show the same phase and amplitude of the magnetization precession, indicating the same direction of magnetization at the same magnetic field regardless of its sweeping direction. This dynamic behavior is expected based on the observed hysteresis loop that shows the same magnetization for increasing and decreasing field sweeps.

Reproduced with permission of the copyright owner. Further reproduction prohibited without permission.

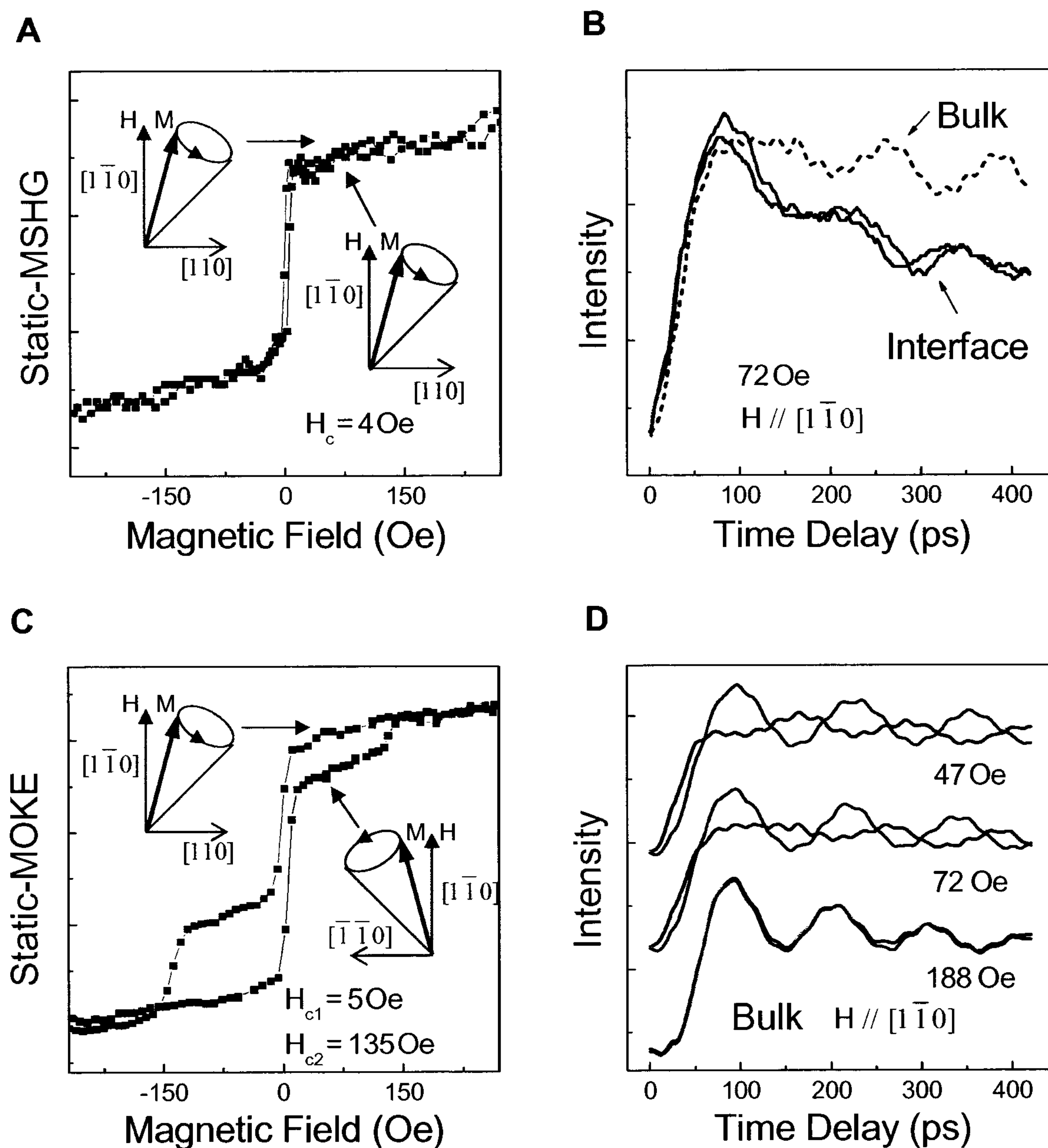

Fig. 4.3: (a) Interface *M-H* loop taken by static MSHG measurement. (b) Interface magnetization precession at H = 72 Oe. Black and red curves are taken with field sweeping up or down, respectively. Dashed blue curve shows bulk magnetization precession at 72 Oe with field sweeping up. (c) Bulk *M-H* loop taken by static MOKE measurement. (d) Bulk magnetization precessions at fields of 47 Oe, 72 Oe and 188 Oe. Black and red curves are taken with field sweeping up or down, respectively.

Reproduced with permission of the copyright owner. Further reproduction prohibited without permission.

The dashed blue curve in Fig. 4.3 (b) shows the corresponding precession dynamics of the bulk obtained with TR-MOKE. A comparison of the solid and dashed curves reveals that the interface and bulk magnetization precessions are clearly decoupled and are ~ 180 degrees out of phase. This is attributed to the different switching characteristics of the bulk and a vanishingly small exchange coupling between the interface and bulk magnetization, as discussed below.

The hysteresis loop in Fig. 4.3 (c) recorded by static MOKE shows a distinctly different reversal behavior in the bulk – a two-step switching process [58-60,76]. The first step at +/-6 Oe occurs when the magnetization is pulled over the intermediate hard axis [110]. The reversal sequence of the magnetization vector is illustrated in Fig. 3.3. As the magnitude of the reversed applied field increases further to about +/-134 Oe, the second step occurs as M rotates through the hard-hard axis [1-10] [58-60,76].

The effect of the two-step switching on coherent magnetization precession in the bulk is shown in Fig. 4.3 (d). The red curves are taken at fields sweeping down, while the black curves are taken at fields sweeping up. The two curves measured at 47 Oe exhibit a phase difference close to 180° indicating a different equilibrium magnetization direction. From the above switching model, the magnetization stays between the [010] easy axis and the [1-10] hard axis for the field sweeping down, while it stays between the [100] easy axis and the [1-10] hard axis for the field sweeping up. In both cases, heating by the pump pulse instantaneously changes the in-plane anisotropy so that the equilibrium direction of magnetization becomes closer to the applied field direction, i.e., [1-10] axis. The change of the equilibrium direction happens too fast for the magnetization to follow, so it starts precessing about the new equilibrium axis. Since the magnetization stays

Reproduced with permission of the copyright owner. Further reproduction prohibited without permission.

nearly symmetric about the [1-10] direction in the two measurements, the initial angle of magnetization with the new equilibrium axis has opposite signs in the two cases (Fig. 4.3 c). This is equivalent to a phase difference of 180° because in both cases the magnetization vector precesses counterclockwise about the equilibrium axis H_{eff} according to $\dot{M} = -\gamma M \times H_{eff}$.

Similar precession dynamics is observed when the field is tuned to 72 Oe which is between the first and second switching field (Fig. 4.3 d). However, no phase difference is observed when the field is increased to 188 Oe which is above the second switching field. Therefore, we conclude that the two-step switching causes the observed phase shift in the bulk spin precession.

Since the direction of the interface magnetization and its precession phase do not depend on the history of the sweeping field (Fig. 4.3 a, b), the interface and bulk spin precession are decoupled, and exhibit an opposite initial phase between them at applied fields below the second switching field in the bulk. The nearly 180° phase difference can be seen from comparison of the interface and bulk precession curves in Fig. 4.3 (b) measured at the same field of 72 Oe, where the interface and bulk equilibrium magnetization stay nearly symmetric about the [1-10] axis. Therefore, the noncollinear spin orientation revealed in static measurements is also manifested in the dynamic process on the picosecond time scale.

Our findings provide new insights into dynamic phenomena occurring at magnetic interfaces and demonstrate that the interface magnetization may be manipulated independently and at higher frequencies than that of the bulk film. These results indicate that faster magnetization switching can be achieved in nanostructures where interface

Reproduced with permission of the copyright owner. Further reproduction prohibited without permission.

properties dominate, and portend higher speed operation in future magnetic nanoscale devices.

4.3 Bulk magnetization precession

The process of magnetization reversal in thin films is of considerable importance in magnetic and magneto optical recording, and in the context of magnetoelectronics [84]. These applications require very small ferromagnetic elements with uniaxial anisotropy for storing binary information in two stable states. Epitaxial growth of a ferromagnetic metal on a semiconductor provides an approach to realize high-density arrays of magnetic elements by using intrinsic in-plane uniaxial anisotropy instead of shape anisotropy. A ferromagnetic Fe film grown epitaxially on a GaAs (001) substrate is a particularly promising system because of its small lattice mismatch and strong uniaxial magnetic anisotropy. Since such applications require fast switching of the magnetization, it is highly desirable to understand the influence of the magnetic character of bulk Fe on coherent magnetization precession which is a prerequisite to realize fast precessional switching.

4.3.1 Uniform magnetization precession in 10-nm Fe (001) film

The bulk magnetization precession is triggered by the same mechanism as interface magnetization precession discussed in the previous section. In the following studies, a modulated pump beam with 15-μJ pulse energy is focused to a spot of 1-mm in diameter on the sample as illustrated in Fig. 4.4(a). The effect on the magnetization is

Reproduced with permission of the copyright owner. Further reproduction prohibited without permission.

measured by a much weaker (~1 μJ), time delayed probe beam using the MOKE technique.

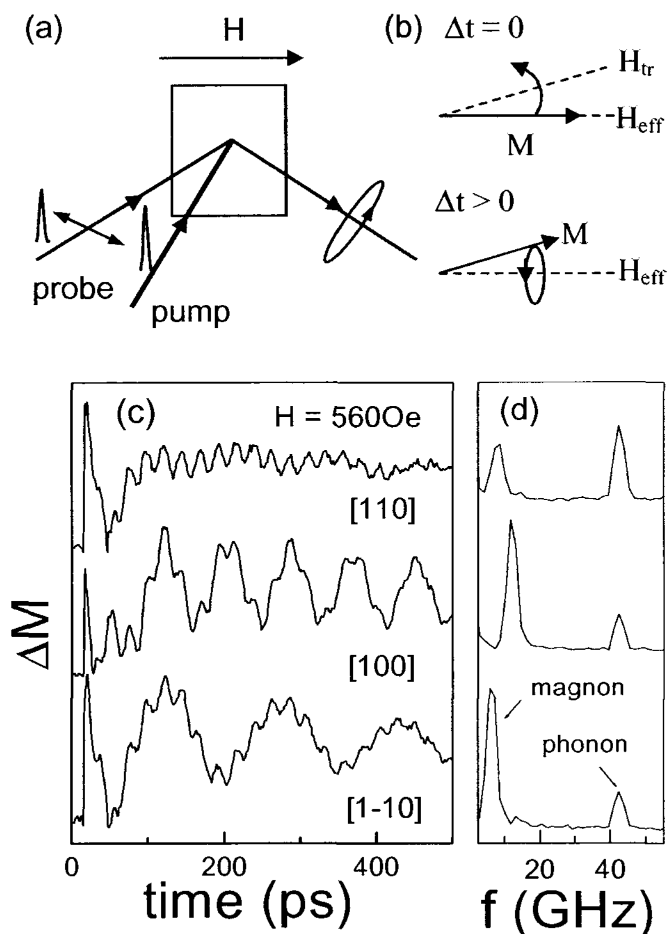

Fig. 4.4: (a) Experimental configuration with longitudinal geometry, (b) schematic diagram of the coherent excitation process of uniform magnetization precession, (c) Transient Kerr signal and (d) Fourier transforms of (c) after picosecond excitation of a 10-nm thick epitaxial Fe film with magnetic field H = 560 Oe applied along [110], [100] and [1-10] directions.

Figure 4.4(c) shows typical results for the magnetization evolution after excitation of the 10-nm thick Fe film for an applied magnetic field of 560 Oe. The Fourier spectra of the transient MOKE signals reveal two coherent excitations with distinct frequencies

Reproduced with permission of the copyright owner. Further reproduction prohibited without permission.

(Fig. 4.4(d)). The high-frequency oscillation at 42.5 GHz is independent of the magnetic field. This mode corresponds to a transverse acoustic (TA) phonon which is generated in the GaAs substrate by the instant lattice expansion of the Fe film at $\Delta t = 0$ ps. The coherent TA phonon is coupled to the photon by conserving the momentum through backward Raman scattering causing oscillation of the reflected probe beam intensity [85]. The second oscillation at lower frequency (5-15 GHz) depends on the magnitude and orientation of the magnetic field. Figure 4.4(c) shows that the film relaxes back to quasi-equilibrium after approximately 50 ps, and therefore the measured precession occurs in the original anisotropy field, thus revealing the equilibrium magnetic properties [82]. As shown below, the anisotropy and demagnetization field of the coherent magnetization precession agrees well with the parameters of the uniform FMR mode measured in a 96 Å thick Fe film on GaAs (001) [55].

As shown in Figs. 4.4(c) and 4.5(a), large spin waves are generated along the [1-10] and [100] directions, while only a weak spin wave excitation is observed along the [110] direction where the magnetization is less canted. For a magnetic field of 560 Oe applied along the [1-10] or [100] direction, the magnetization is canted away from the applied field because of the uniaxial character of the magnetic anisotropy of the Fe film. The cubic magnetocrytalline anisotropy also contributes to the transient anisotropy field, but this effect is small. This has been verified with a 50-nm thick epitaxial Fe film which exhibits no uniaxial anisotropy. In this control sample the precession amplitude is 5 times smaller. Furthermore, the oscillating MOKE signal shows the same phase for opposite applied magnetic fields. This excludes the existence of an out-of-plane transient magnetic field. We note the large spin wave amplitude at small magnetic field applied along the in-

Reproduced with permission of the copyright owner. Further reproduction prohibited without permission.

plane hard [1-10] axis. An even larger rotation angle can be achieved at higher excitation level and larger uniaxial magnetic anisotropy, as for example in thinner Fe films. This would lead to a large out-of-plane component of magnetization and the resultant demagnetization field could trigger an out-of-plane precession. This process could then be utilized for fast magnetization reversal.

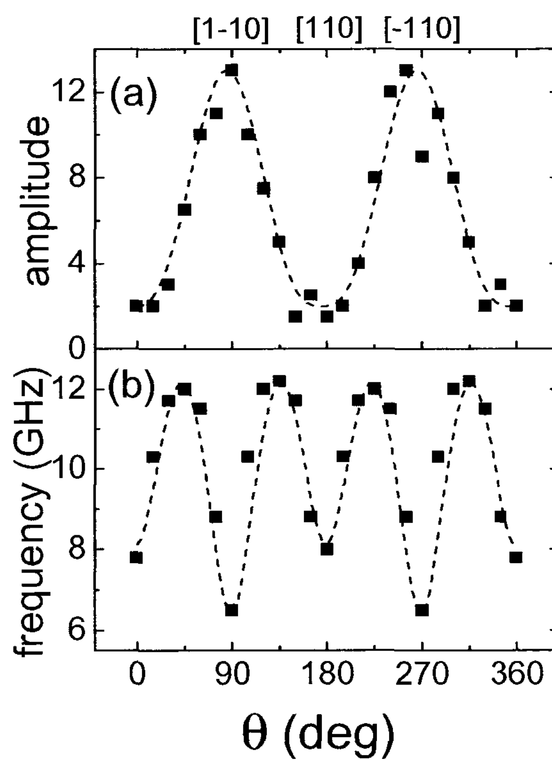

Fig. 4.5: (a) Precession amplitude and (b) frequency as a function of sample orientation at magnetic field H = 560 Oe. The dashed line is a guide to the eye.

The orientation dependence of the precession frequency clearly reveals uniaxial and cubic anisotropy as shown in Fig. 4.5(b). We will show in the following that the magnetic anisotropy constants can be determined from the field dependence and anisotropy of the precession frequency. Figure 4.6(a) shows the frequency spectra for

Reproduced with permission of the copyright owner. Further reproduction prohibited without permission.

magnetic fields applied along the [100] and [1-10] directions. The latter is the hard axis for the uniaxial and cubic magnetic anisotropies. For small angle excitations, the frequency dispersion is well described by the model of the uniform FMR mode [55]. Previous Brillouin scattering [86,87] and FMR studies [55] on thin Fe films suggest that surface anisotropy and spin pinning is negligible. The field dependence of uniform precession frequencies, described by Eq. (4.1), allows us to determine these values. Here, the anisotropy field is given by:

$$\begin{aligned} H^{\alpha} &= 4\pi M_s + \frac{2K_{out}}{M_s} - \frac{K_u}{M_s}(\sin\phi - \cos\phi)^2 + \frac{K_1}{M_s}(2 - \sin^2(2\phi)), \\ H^{\beta} &= \frac{2K_1}{M_s}\cos(4\phi) + \frac{2K_u}{M_s}\sin(2\phi), \end{aligned} \tag{4.3}$$

K_1, K_u and K_{out} are the cubic anisotropy, in-plane uniaxial anisotropy and out-of-plane anisotropy constants, respectively.

To accurately describe the field dependence of the precession frequency, we need to know the magnetization angle ϕ which is determined by the subtle balance of external and internal magnetic field caused by the magnetic anisotropy. The dependence of ϕ on applied magnetic field is obtained from the hysteresis curves measured by VSM. The solid lines in Fig. 4.6 (a) are the precession frequencies calculated from Eq. (4.1) and (4.3). The cubic anisotropy K_1/M_s, uniaxial anisotropy K_u/M_s and out-of-plane saturated magnetic field $4\pi M_s+2K_{out}/M_s$ used in the calculation are 0.21 KOe, 0.09 KOe, and 17.5 KOe, respectively. The angle ϕ calculated from the above anisotropy constants reproduces the in-plane hysteresis curve, and the out-of-plane saturated field is consistent with independent MOKE measurements. For the easy [100] axis, the precession frequency increases monotonically with increasing applied magnetic field. This behavior

Reproduced with permission of the copyright owner. Further reproduction prohibited without permission.

is typical along an easy axis. For the hard [1-10] axis, the frequency initially increases due to the rotation of the magnetization toward the easy [100] axis, then decreases due to further rotation towards the hard [1-10] axis, and finally increases as the magnetization aligns along the applied magnetic field direction.

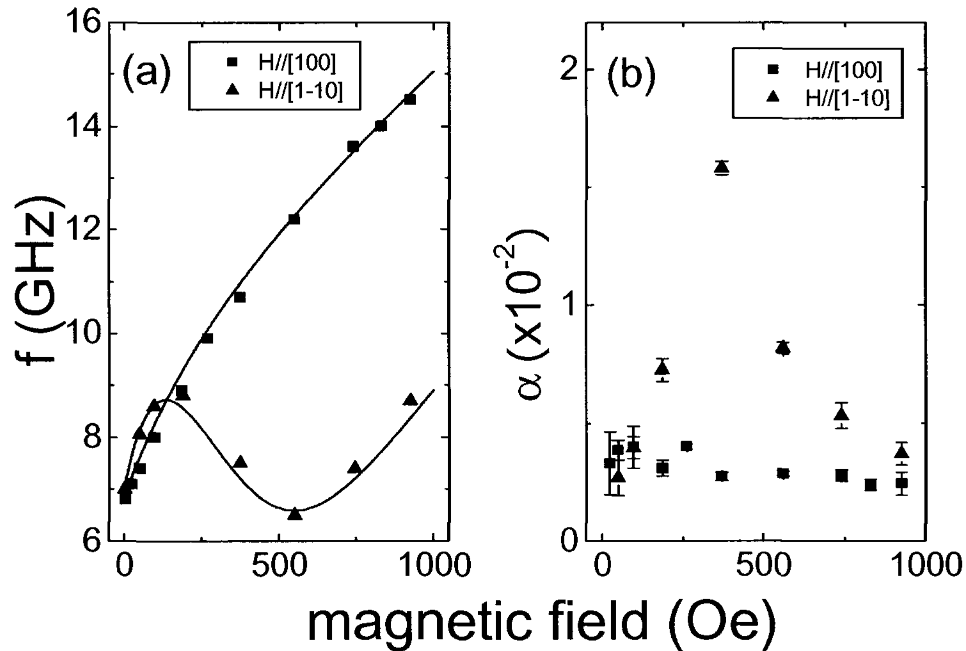

Fig. 4.6: (a) Precession frequency versus applied magnetic field along [100] and [1-10] axes. The solid line is a fit by Eq. (4.1) and (4.3). (b) Gilbert damping parameter α versus applied magnetic field along [100] and [1-10] directions.

The (Gilbert) damping parameter α is another important factor in fast magnetic switching. Generally the damping parameter is treated as a constant. However, there is theoretical and experimental evidence [88,89] that α can vary with the magnetization angle relative to the field direction and film normal, with the magnitude of the applied field, and with the precession frequency. By including the damping term in the Landau-

Reproduced with permission of the copyright owner. Further reproduction prohibited without permission.

Lifshitz equation, the uniform magnetization precession can be described by an oscillating term and an exponential decaying term $\exp(-\Gamma t)$, where

$$\Gamma = \frac{\alpha\gamma[(H_e\cos(\delta-\phi)+H^{\alpha})+(H_e\cos(\delta-\phi)+H^{\beta})]}{2(1+\alpha^2)}. \quad (4.4)$$

The expression for Γ can be simplified as $\Gamma = \alpha\omega$ in the case of $H^{\alpha} = H^{\beta}$ and small α. The damping parameter α is calculated from Eq. (4.4) and parameters used in Eq. (4.1) for the frequency calculation. Figure 4.6(b) shows α as a function of the magnetic field applied along the [100] and [1-10] directions. The damping parameter varies strongly with applied field along the hard [1-10] axis whereas α remains nearly constant along the easy [100] axis. This behavior may be explained by the two-magnon scattering process where the damping rate depends on the spin wave manifold [88]. For the hard axis, the magnetization rotates towards the [1-10] direction with increasing applied field. This will change the density of accepting magnon states and therefore the damping parameter. In contrast, for the easy [100] axis the magnetization direction will not significantly rotate with increasing applied field and therefore α remains nearly constant. Further studies are required to fully elucidate the damping mechanism.

4.3.2 Spin wave excitation in 50-nm Fe (001) film

Figure 4.7(a) shows typical results for the magnetization evolution after excitation of the 50-nm thick Fe film with the external field applied along the hard axis [110]. The presented time-domain data clearly show the oscillatory variation of the MOKE signal. Such oscillations strongly depend on the strength of the applied field, indicating the coherent excitation of magnetization precession.

Reproduced with permission of the copyright owner. Further reproduction prohibited without permission.

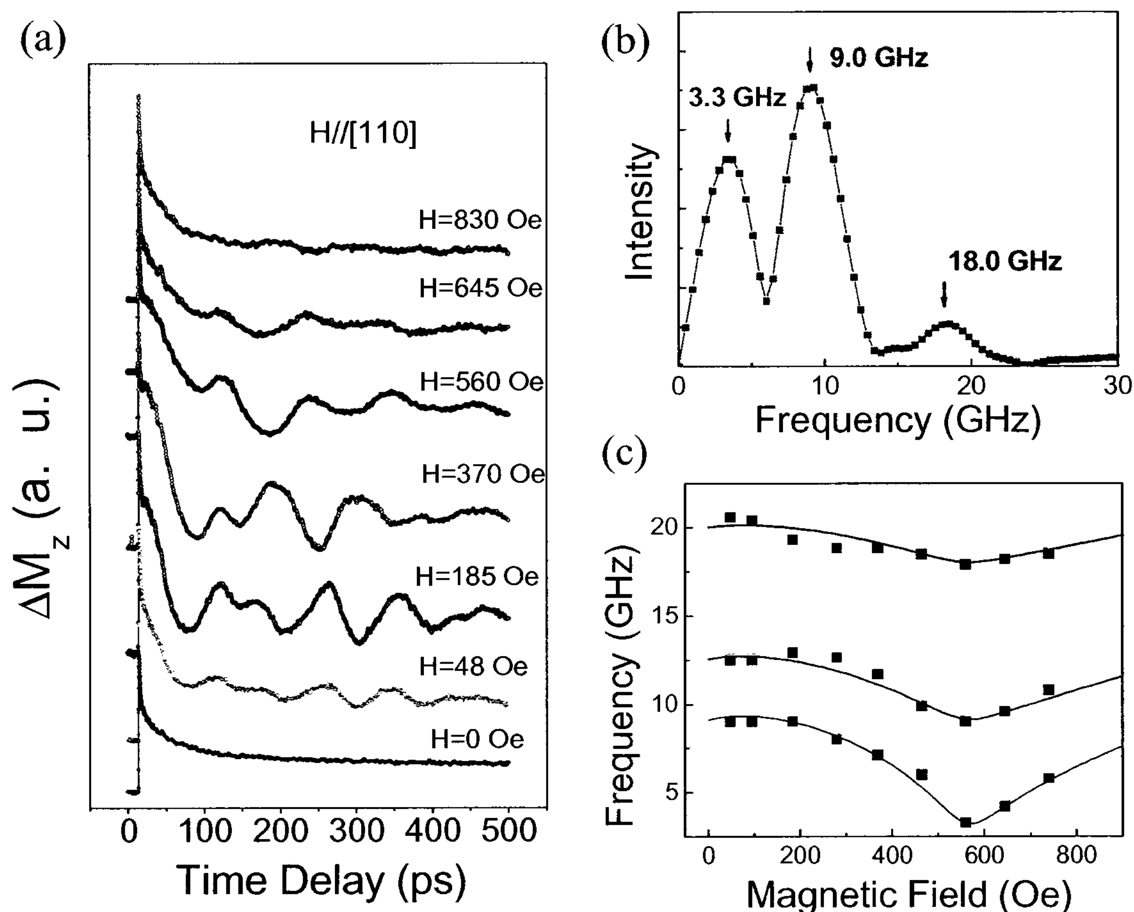

Fig. 4.7: (a) Transient Kerr signal after picosecond excitation of a 50-nm thick epitaxial Fe film with magnetic field applied along [110], (b) Fourier transforms of (a), and (c) precession frequency versus magnetic field. The solid lines are fits by Eq. (4.5).

The fact that the oscillations vanish at zero magnetic field and at fields larger than 800 Oe reveals that canting the magnetization is important to excite coherent magnetization precession. At zero field, the magnetization aligns along the magnetic easy axis [100] which keeps the easiest direction when the pump beam changes the magnetic crystalline anisotropy and demagnetizes the medium. Therefore no torque can drive the magnetization away from this direction, and we only observe an exponential decay of the

Reproduced with permission of the copyright owner. Further reproduction prohibited without permission.

MOKE signal due to the recovery of the magnetization modulus. At magnetic fields larger than 800 Oe, the magnetization aligns along the direction of the field, which is strong enough to pin the magnetization when the magneto-crystalline energy is modified by the pump beam such that the magnetization always stays along the same direction. For medium strength of applied field, the direction of the effective field can be modified by the pump beam due to the competition between the anisotropy field and the external field. Consequently, the magnetization may rotate away from the equilibrium direction and precess about this direction when the medium returns to equilibrium. The Fourier spectra of the transient MOKE signals (Fig. 4.7 (b)) reveal three coherent excitations of magnetization precession. The field dependence of the precession frequencies is shown in Fig. 4.7 (c). The precession with lowest frequency corresponds to the uniform mode, which is determined by the sum of anisotropy field H_a, demagnetizing field H_d, and external field H_e. The cubic anisotropy K_1/M_s, and out-of-plane saturated magnetic field $4\pi M_s+2K_{out}/M_s$ determined from the best fit of the data (Fig. 4.7) by Eq (4.1) are 0.27 KOe and 17.5 KOe, respectively, and the uniaxial anisotropy K_u/M_s is negligible. These magnetic anisotropy constants are very close to that in bulk Fe, which has cubic magneocrystalline anisotropy of 0.28 KOe. The hysteresis curve calculated from the above anisotropy constants reproduces the magnetization reversal process measured by VSM.

The other two precession modes with higher frequencies than the uniform mode correspond to the first and second order spin wave modes, in which not only anisotropy field but also the exchange field $H_{ex} = \frac{2A}{M_s^2}\nabla^2 M$ may affect the speed of spin precession. The exchange field originates from the exchange interaction between electronic spins and

Reproduced with permission of the copyright owner. Further reproduction prohibited without permission.

is proportional to the square of the spin wave vector q. In our experiments, the in-plane wave vector must be very small, since the diameter of the optical pump and probe beam is much larger than the wavelength of the spin wave modes (1 mm vs. 20 μm), and hence the response from the magnetization is averaged within this region. The exchange field caused by in-plane spin interaction is then much smaller than the anisotropy field and external field, and it can be neglected. The large spin wave vector along vertical direction, however, may contribute significantly to the exchange field in thin films.

Considering the electromagnetic and exchange boundary conditions [90] with free spin at the interfaces, we find that the normal modes are sine- or cosine-type standing spin waves whose frequencies can be described by:

$$(\frac{\omega}{\gamma})^2 = (H\cos(\phi_H - \phi) + H_\alpha + \frac{2A}{M_s}q^2)(H\cos(\phi_H - \phi) + H_\beta + \frac{2A}{M_s}q^2) \tag{4.5}$$

where H^α and H^β are given in Eq. (4.3), and q is the spin wave vector normal to the surface plane given by $\frac{n\pi}{l}$. Here, n denotes the order of the standing spin wave mode and l is the thickness of the film. We may note from Eq. (4.5) that in a ferromagnetic film the large exchange stiffness constant may markedly enhance the spin precession frequency. For high order spin wave modes in which the exchange field dominates, the precession frequency is simply proportional to A, and it will follow the n^2 law which refers to a quadratic increase of frequency with respect to the spin wave order [91]. However, a significant deviation from n^2 law is observed in the low order spin wave modes in ferromagnetic resonance [91,92]. No quantitative model is available to precisely describe the low order spin wave modes due to the limited data points in such experiment.

Reproduced with permission of the copyright owner. Further reproduction prohibited without permission.

The field dependence of precession frequency in our pump-probe experiments provides complementary information in the regime of low-order spin waves in which the anisotropy field and exchange field are comparable. In Fig. 4.7(c), we note that the frequency curves of spin wave modes as well as uniform mode exhibit a minimum at the saturation field of 560 Oe. This is caused by the rotation of the magnetization, which reduces the anisotropy field with increasing applied field. Therefore, the anisotropy field affects the frequency of spin waves the same way as it affects the uniform mode.

The separation of frequency between each mode is then caused by the exchange field which grows as the order of the mode increases. The exchange stiffness constant is determined to be 0.8×10^{-6} erg/cm from the simultaneous fitting of the first and second order standing spin waves (Fig. 4.7(c)) using Eq. (4.5). The good agreement between the calculation and experimental data indicates no significant effect of the magnetization rotation on the mode profile of the standing spin wave.

The above model is also sufficient to describe the azimuthal dependence of spin wave excitation presented in Fig. 4.8. In such measurement, the amplitude of the field is fixed at 560 Oe, but the sample is rotated between the hard [110] and the easy [100] directions. No spin wave is excited along the easy [100] axis, further revealing the importance of canting magnetization for spin wave excitation. We obtain the same anisotropy and exchange stiffness constants from the fitting to the azimuthal dependence of spin wave frequencies (Fig. 4.8(b)).

Reproduced with permission of the copyright owner. Further reproduction prohibited without permission.

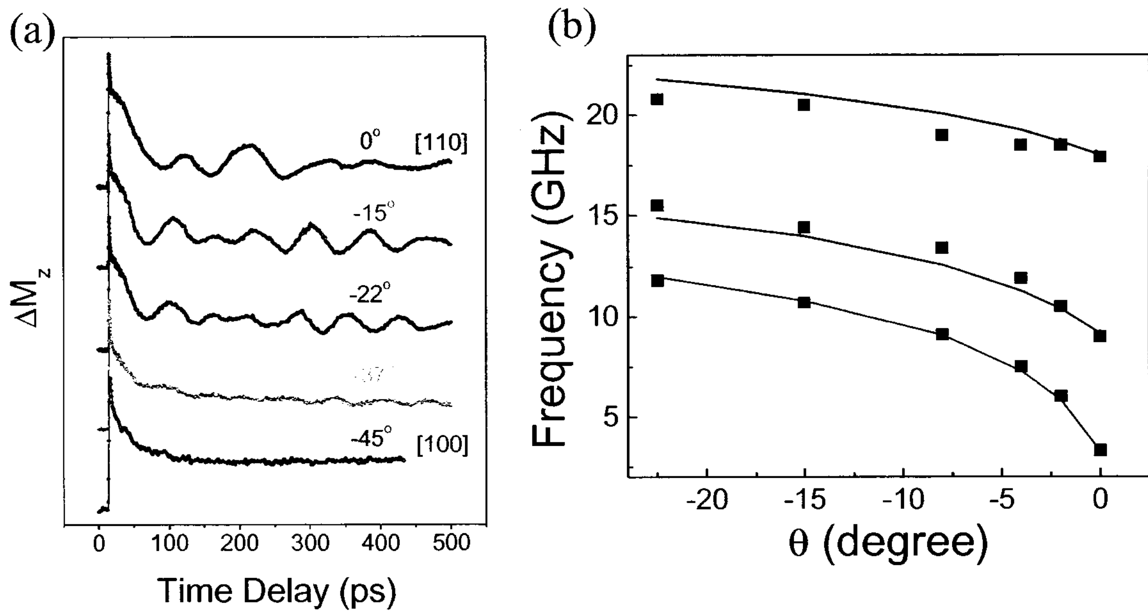

Fig. 4.8: (a) Transient Kerr signal after picosecond excitation of a 50-nm thick epitaxial Fe film with magnetic field of 560 Oe applied along different directions, and (b) precession frequency versus magnetic field. The solid lines are fit by Eq. (4.5).

However, the measured exchange stiffness constant is only about half of that determined from the high order spin wave modes in FMR [91]. This difference was thought to be caused by the pinning effect at interfaces due to its large surface anisotropy [92,93]. Pinning modifies the location of the surface antinodes of the standing spin waves thereby changing their effective wavelength. The other factors including the gradients of the internal field and magnetic moment may also affect the variation of magnetization close to the interfaces [94]. Although our results demonstrate that single effective exchange stiffness constant can indeed account for these factors, future theoretical work is needed to clarify the intrinsic physical nature.

Reproduced with permission of the copyright owner. Further reproduction prohibited without permission.

Summary

The dynamic response of the Fe/AlGaAs (001) magnetization to an optical excitation is studied by TR-MSHG and TR-MOKE spectroscopy. The coherent precession of the interface magnetization is decoupled from the bulk magnetization precession, and exhibits a higher frequency and opposite phase for a given applied field. A striking difference between interface and bulk magnetic anisotropy is revealed from the calculation of precessional frequency by LLG equation.

Uniform precessions are generated by ultrafast optical excitation along all directions of 10-nm Fe film. The anisotropy of the damping parameters is determined from the decay of the FMR mode, which are crucial in designing fast magnetic switching devices and novel spintronics devices. Low order standing spin wave modes as well as uniform precession are observed in the 50-nm Fe film, allowing the analysis of exchange stiffness constant in the bulk film.

Reproduced with permission of the copyright owner. Further reproduction prohibited without permission.

Chapter 5

Time-resolved spin precession in manganite films

Optically excited uniform magnetization precession in the ferromagnetic state of $La_{0.67}Ca_{0.33}MnO_3$ (LCMO) and $La_{0.67}Sr_{0.33}MnO_3$ (LSMO) films grown on different substrates are investigated by time-resolved magneto-optic Kerr effect. The parameters of magnetic anisotropy are determined from the measured field dependence of the precession frequency.

For LCMO film, the dominant anisotropy contribution in the film grown on $SrTiO_3$ (001) is the strain-induced easy-plane anisotropy. The strain-free films on $NdGaO_3$ (110) exhibit a uniaxial in-plane anisotropy that results from the interface due to the tilting of the oxygen octahedra in $NdGaO_3$.

For LSMO film, the easy-plane anisotropy is found in the tensile-strained film grown on $SrTiO_3$ (001) substrate, whereas the compressive-strained film grown on $LaAlO_3$ (100) substrate exhibits an easy normal-to-plane axis.

5.1 Introduction

Half-metallic nature [95] of manganites makes them technologically important materials for magnetic tunnel junctions [96-98] and spin injection structures [99,100]. Manganites share the same crystal structure as the mineral perovskite shown in Fig. 5.1.

Reproduced with permission of the copyright owner. Further reproduction prohibited without permission.

The ferromagnetic coupling between nearest neighbor Mn ions results from a double exchange mechanism [101]. Understanding of the magnetization dynamics in manganite thin films is important for the fastest switching operation of the spin-based devices. Several factors, such as the possible normal modes and the damping of the coherent magnetization precession, play a crucial role in achieving reliable switching behavior.

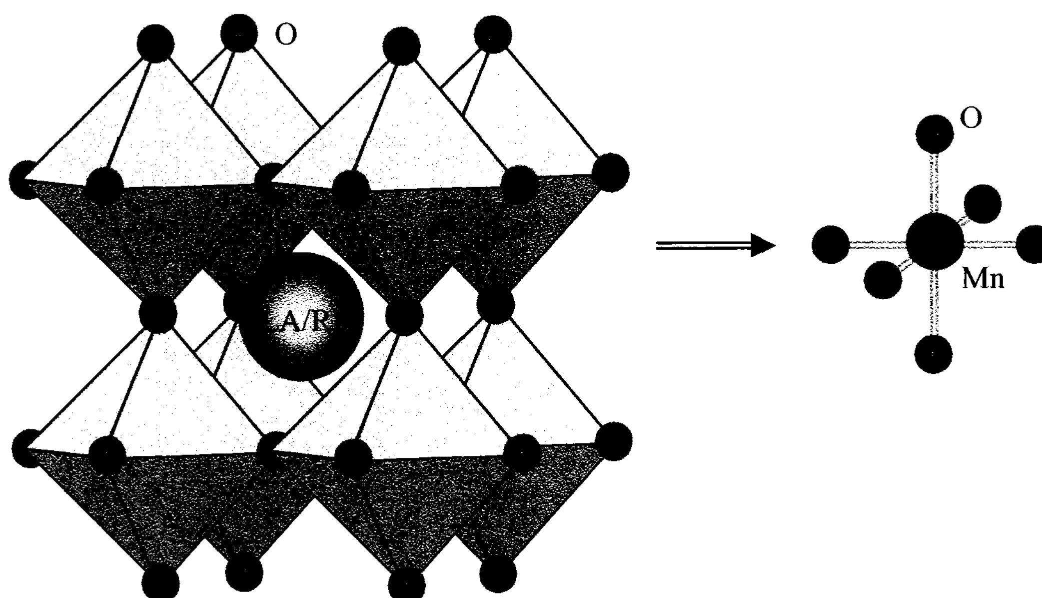

Fig. 5.1: Crystal structure of doped manganites :$LA_{1-x}RE_xMnO_3$. Each manganese atom is surrounded by six oxygen atoms to form a regular MnO_6 octahedron. The six oxygen atoms occupy the faces of a cube. Between the octahedral, at the corner of the cubes, lies a mixture of trivalent rare earth (LA) and divalent alkaline earth (RE) cations.

In this chapter, the dynamical magnetization response to an ultrashort laser pulse is investigated in $La_{0.67}Ca_{0.33}MnO_3$ and $La_{0.67}Sr_{0.33}MnO_3$ thin films. LCMO (T_c ~ 250 K)

Reproduced with permission of the copyright owner. Further reproduction prohibited without permission.

and LSMO (T_c ~380 K) belong to a family of colossal magnetoresistance manganites. Earlier investigations of magnetization dynamics in manganite thin films have been performed by ferromagnetic resonance (FMR) measurements, where the absorption of an alternating microwave field is measured as a function of a static magnetic field [102-107]. However, only sub-nanosecond or 100-picosecond dynamics with a fixed magnitude of the magnetization vector can be explored because of the low frequency (10 GHz) used in FMR and the direct coupling of the microwave field to the magnetization. On the long timescale accessible to FMR, the dynamics is governed entirely by the magnetic anisotropy of the film. The angular dependence of the resonance field in the FMR experiment provides information on the anisotropy constants - parameters that are crucial for the design of thin-film devices. Most of the FMR studies, however, did not explore the magnetic anisotropy in detail, but focused on the magnetic homogeneity of the manganite films, which was evaluated from the FMR linewidth.

In ultrafast optical studies, the sub-picosecond time resolution allows to study the magnetic response that is much faster than the coherent precession of magnetization. A strong laser pulse first excites electrons in the sample. The sample's magnetic response is then monitored as a function of the time delay between the pump and probe pulses. The coupling of the laser-pulse excitation to the magnetization of the sample is not always readily understood, which underscores the importance of magneto-optic measurements. The high spatial resolution of the optical approach, compared to FMR, will prove useful in the study of microscopic magnetic elements.

The first study of the picosecond magnetization dynamics of manganites was reported by Zhao *et al* [108], who monitored the optically induced conductance changes

Reproduced with permission of the copyright owner. Further reproduction prohibited without permission.

in LCMO films with 20-ps time resolution. Long-lived spin excitations were found responsible for a resistivity increase in the ferromagnetic phase. Several groups used time-resolved absorption measurements to study the photoinduced response of manganites. Matsuda *et al* [109] reported that the gradual change (200 ps) in the photoinduced absorption reflects the photoinduced demagnetization (PID) in $(Nd_{0.5}Sm_{0.5})Sr_{0.4}MnO_3$. More detailed studies by Lobad *et al* [110,111] and Averitt *et al* [112] of LCMO attributed the ultrafast component (100 fs) of the photoinduced absorption to electron-lattice thermalization. The slower change in absorption (20-200 ps) was ascribed to the PID driven by the spin-lattice thermalization. A long-lived spin relaxation component was found in $Nd_{0.67}Sr_{0.33}MnO_3$ in transient reflectivity measurements by Ren *et al* [113]. The relaxation was shown to be magnetic in origin and dependent on the strain induced by different substrates. In these studies, slow changes in the optical absorption were interpreted as the magnetization response. Subsequent studies by Ogasawara *et al* [114] and McGill *et al* [115,116] employed the time-resolved magneto-optic Kerr effect (TR-MOKE) to study the magnetization dynamics. Ogasawara *et al* found that after photoexcitation, the magnetization in $La_{0.6}Sr_{0.4}MnO_3$ (LSMO) decreases with a considerably longer time constant (1 ns) than the one measured by the transient absorption measurements [109-112]. McGill *et al* [116] studied the magneto-optic response of LCMO near T_c and observed the PID together with an even slower Kerr transient which they attributed to photoinduced spin ordering.

Photoinduced demagnetization is not the only effect created by a laser pulse impinging on a ferromagnetic sample. Ogasawara *et al* [114] pointed out the presence of an oscillatory component in their TR-MOKE measurements, which they interpreted as a

Reproduced with permission of the copyright owner. Further reproduction prohibited without permission.

coherent precession of magnetization in LSMO, but did not study this phenomenon in more detail. Photoinduced spin precession was first reported by Ju *et al* [117] in the study of optically excited exchange-biased NiFe/NiO bilayers. The precession of the NiFe magnetization was launched by the pump pulse via the "unpinning" of the exchange bias and detected by TR-MOKE. Optically induced magnetization precession was discovered in thin Ni films by Koopmans *et al* [118], who later confirmed [82] that the optically induced coherent precession and FMR are manifestations of the same phenomenon. They pointed out that the precession can be used as the "all-optical real-time ferromagnetic resonance" to study the properties of microscopic magnetic elements. Koopmans *et al* argued that the coherent precession in their measurements was induced by the thermal modification of the anisotropy in the Ni film. Zhang *et al* [119] induced the coherent magnetization precession in CrO_2 thin films by optically modulating the magnetic anisotropy of the films by nonthermal hot-electron spins. The work of Koopmans *et al* and Zhang *et al* demonstrated that the coherent precession in optical measurements is governed by the magnetic properties of the sample.

Here, photoinduced magnetization dynamics in LCMO and LSMO thin films are investigated by TR-MOKE. The goal is to determine the anisotropy of LCMO and LSMO films grown on different substrates from the field dependence of the precession frequency.

Substrate-induced magnetic anisotropy has been attributed to magnetoelastic interaction [120-124]. Static magnetization and FMR measurements on LSMO films by Kwon *et al* [125] revealed a magnetic anisotropy that depends on the strain state of the film. Easy plane anisotropy was found in tensile-strained LSMO/STO films, and easy normal-to-plane axis was discovered in compressively strained LSMO films grown on

Reproduced with permission of the copyright owner. Further reproduction prohibited without permission.

$LaAlO_3$ (001) (LAO). No in-plane anisotropy was detected by FMR. Similar magnetic anisotropy behavior was found in $Pr_{0.67}Sr_{0.33}MnO_3$ (PSMO) films by Wang *et al* [126]. PSMO films grown on STO and LAO displayed easy-plane and normal-to-plane easy-axis anisotropy, respectively. The anisotropy of the PSMO/NGO film could not be determined from magnetization measurements due to the large paramagnetic contribution of NGO. Suzuki *et al* [120] and Steenbeck and Hiergeist [121] studied the anisotropy of strained LSMO films and reported an in-plane biaxial anisotropy. The two studies disagreed whether the [100] (Mn-O bond direction) or the [110] axes are the easy axes in the tensile strained LSMO/STO films. O'Donnel *et al* [122] found an easy plane and a biaxial in-plane anisotropy with [100] easy axes in LCMO/STO. Recent measurements by Xiong *et al* [124] of magnetic anisotropy in LCMO films confirmed the dependence of the out-of-plane anisotropy constant on the amount of strain in the film, but revealed no in-plane anisotropy.

5.2 Magnetization precession and magnetic anisotropy in LCMO films

The LCMO films were epitaxially grown by pulsed-laser deposition on two substrates - SrTiO3 (100) and NdGaO3 (110) [127,128]. The film thicknesses are 60 nm, 100 nm, and 150 nm. The STO substrate induces biaxial tensile strain in LCMO films, while the NGO substrate induces very little strain. The samples are provided by Dr. Qi Li's group in Pennsylvania State University.

Most TR-MOKE measurements are performed with an applied pump fluence of 5 mJ/cm^2. Fluences as low as 1 mJ/cm^2 and as high as 10 mJ/cm^2 do not change the overall appearance of the TR-MOKE spectra. The extracted precession frequency shows no

Reproduced with permission of the copyright owner. Further reproduction prohibited without permission.

dependence on the excitation power. To study the field dependence of the precession frequency, we mount the samples in the center of a split-coil superconducting magnet (0-9 T) that allows optical access to the sample with the magnetic field being either in the film plane or almost normal to it. The variable-temperature inset of the magnet is used to control the sample temperature in the 10-300 K range.

The time-evolution of the precession is recorded by a delayed *s*-polarized probe pulse (400 nm) whose angle of incidence is close to zero (almost normal incidence, Fig. 5.2(a)). In this polar geometry, the polarization rotation of the reflected probe pulse is proportional to the normal component of magnetization M_z. Ogasawara *et al* [114] have found that the Kerr rotation in LSMO is largest when the probe energy is about 3.1 eV, twice the energy of the pump. Therefore, we use a frequency-doubling crystal and 400-nm probe pulses to increase the sensitivity of our setup.

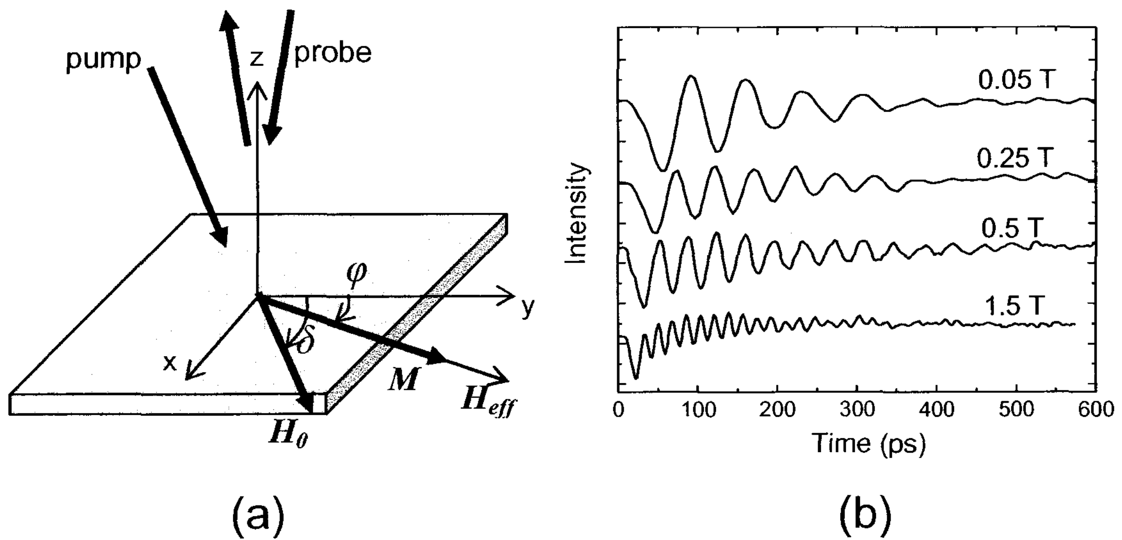

Fig. 5.2: (a) Geometry of the pump-probe measurement with applied magnetic field. (b) Magnetization precession as measured by TR-MOKE in the 60-nm LCMO/NGO film at T = 20 K and $\delta = 45^{o}$.

Reproduced with permission of the copyright owner. Further reproduction prohibited without permission.

Figure 5.2(b) shows the precession of magnetization as recorded by TR-MOKE. The presented time-domain spectra clearly display the oscillatory variation of the light intensity that passes through the analyzer. Since the polarization rotation is proportional to the normal component of M, the frequency of the oscillation corresponds to the frequency of the magnetization precession. By performing a Fourier analysis of the time-domain spectra, we extract the field-dependent precession frequency. In the following section we present the measured frequency-field dependence and compare it with the established theory.

5.2.1 LCMO/STO film

The field dependence of the precession frequency in the 100-nm thick LCMO/STO film is shown in Fig. 5.3. Panel (a) displays the frequencies measured with the in-plane field applied along two directions with an angle of 45° between them. The 0° measurement corresponds to the field applied along the [100] (Mn-O bond) direction. The different frequencies along the two field directions indicate that an in-plane magnetic anisotropy is present in the film.

The observed magnetization precession is described by the Landau-Lifshitz-Gilbert equation: $\frac{d\vec{M}}{dt} = -\gamma\vec{M} \times H_{eff} + \frac{\alpha}{M}\vec{M} \times \frac{d\vec{M}}{dt}$. To explain the frequency-field dependence presented in Fig. 5.3, we need to introduce a uniaxial easy-plane anisotropy $K_a M_z^2 / M_s^2$ ($K_a > 0$) and a fourth-order tetragonal-symmetry anisotropy $-K_{//}(M_x^4 + M_y^4)/2M_s^4 - K_{\perp} M_z^4 / 2M_s^4$ with in-plane easy axes X and Y ($K_{//} > 0$) along the film's [100] and [010] directions. The magnetic free energy can be written as

$$E = -H_0 \cdot M + 2\pi M_z^2 + K_a M_z^2 / M_s^2 - K_{//}(M_x^4 + M_y^4)/2M_s^4 - K_{\perp} M_z^4 / 2M_s^4, \qquad (5.1)$$

Reproduced with permission of the copyright owner. Further reproduction prohibited without permission.

where the first term represents the Zeeman energy and the second denotes the shape anisotropy energy due to demagnetization. The corresponding phenomenological fields are the demagnetizing field $H_d = 4\pi M_s$ and the anisotropy fields $H_a = 2K_a / M_s$, $H_\perp = 2K_\perp / M_s$, and $H_{//} = 2K_{//} / M_s$.

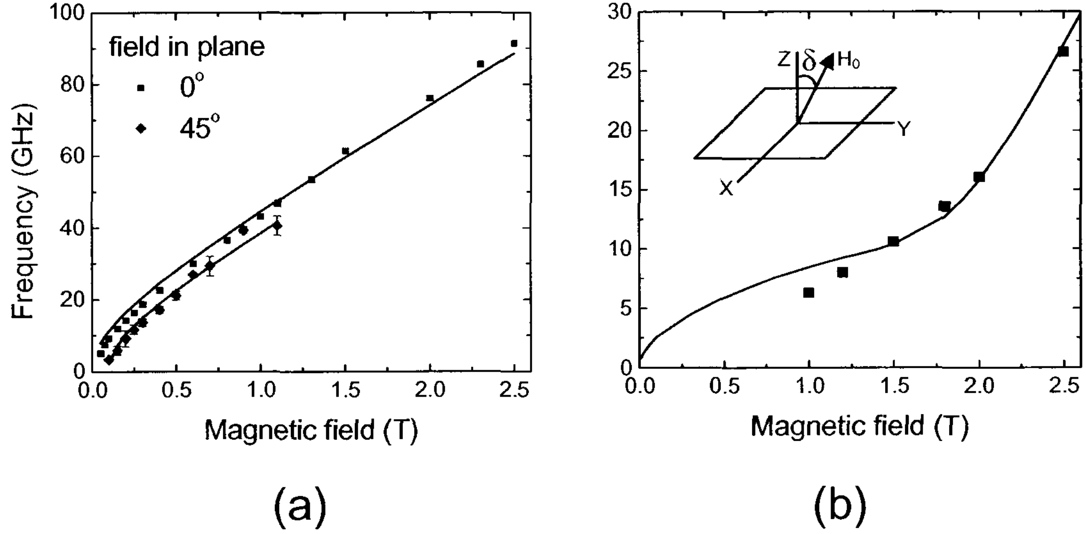

Fig. 5.3: Field dependence of precession frequency in LCMO/STO. Solid lines are calculated using the expressions given by Eq. (5.2), (5.3) and (5.4) with effective fields given in Table 5.1 and *g*-factor of 1.98. (a) Applied magnetic field is in plane. $\delta = 0^\circ$ and $\delta = 45^\circ$ orientations correspond to the field along the in-plane tetragonal easy-axis and along the in-plane tetragonal hard axis, respectively. δ is defined in Fig. 5.2. (b) Applied magnetic field is almost normal to the film and lies in the *Y*-*Z* plane, with *Y* being the tetragonal easy axis.

When the applied field is in the film plane (Fig. 5.2(a) and Fig 5.3 (a)), the precession frequencies can be calculated to be:

$$\omega = \gamma\sqrt{ab}, \tag{5.2}$$

where a and b are given by

$$\begin{aligned} a &= H_0\cos(\delta-\varphi) + H_d + H_a + H_{//}(\sin^4\varphi + \cos^4\varphi) \\ b &= H_0\cos(\delta-\varphi) + H_{//}\cos(4\varphi) \end{aligned} . \tag{5.3}$$

Reproduced with permission of the copyright owner. Further reproduction prohibited without permission.

When the applied field is in the Y-Z plane (Fig. 5.3(b)), the precession frequencies is calculated using Eq. (5.2) with a and b given by

$$\begin{aligned} a &= H_0\cos(\delta-\theta)-(H_d+H_a)\cos 2\theta - H_{//}\sin^2\theta\cos 2\theta + H_\perp\cos^2\theta\cos 2\theta \\ b &= H_0\cos(\delta-\theta)-(H_d+H_a)\cos^2\theta + H_{//}\sin^4\theta + H_\perp\cos^4\theta \end{aligned} \quad , \quad (5.4)$$

where θ is the equilibrium angle between Z and the film's magnetization. The g-factor value of 1.98 is used in the following analysis. Solid lines in Fig. 5.3 show the calculated frequencies. In Fig 5.3(a), the applied field is in the film plane and along the Y axis (or, equivalently, along the X axis) in the 0° measurement and at 45° to both X and Y axes in the 45° measurement. In Fig 5.3(b), the applied field is in the Y-Z plane making a 4° angle with the sample normal. Each solid line represents a result of the least-square fitting procedure carried out separately for each set of data. Only two free parameters are used to fit the in-plane measurements in Fig. 5.3(a) - H_a and $H_{||}$. The bulk magnetization value is used to calculate the demagnetization field H_d = 0.72 T. To fit the out-of-plane measurement in Fig. 5.3(b), H_a, $H_{//}$, and $H_\perp$ are used as fitting parameters. After fitting each measurement separately, the average values of the anisotropy fields are collected in Table 5.1.

TABLE 5.1: Anisotropy field values deduced from fits to the field dependence of the precession frequency in the LCMO/STO film.

sample	H_d (Te)	H_a (T)	$H_\perp$ (T)	$H_{//}$ (T)
LCMO/STO	0.72	0.57+/-0.24	-0.30	0.031+/-0.054

The observed anisotropy constants are in good agreement with static magnetization studies of the effects of strain on the anisotropy in manganite films

Reproduced with permission of the copyright owner. Further reproduction prohibited without permission.

[120,122-124]. The dominant contribution is the uniaxial easy-plane anisotropy with K_a = 1.6×10^5 J/m^3, which is the same as measured by Ranno *et al* [123] and O'Donnel *et al* [122], who found an easy-plane strain-induced anisotropy in tensile-strained LCMO/STO and LSMO/STO films. This uniaxial anisotropy constant K_a is larger than the one measured in the study of photoinduced precession in LSMO/STO (see section 5.3). The difference may result from the LCMO film being thinner than the LSMO film used in Ref. [114] and from LCMO being a lower-bandwidth manganite, thus, being more susceptible to epitaxial strain. The perpendicular component of the tetragonal anisotropy $K_\perp = -0.86 \times 10^5$ J/m^3 agrees well with O'Donnel's 4th order uniaxial easy-plane anisotropy constant. Our measurements also indicate the presence of an in-plane biaxial anisotropy ($K_{//} = 0.1 \times 10^5$ J/m^3) with its easy axes along the in-plane [100] and [010] directions, which corresponds to the directions of Mn-O bonds. Similar behavior was observed by O'Donnel *et al* who measured a higher biaxial anisotropy constant due to their LCMO film being thinner than the critical thickness of 60 nm [123]. No in-plane anisotropy was found by Xiong *et al* [124] in LCMO/STO films in 10-400 nm thickness range.

5.2.2 LCMO/NGO film

Figure 5.4 shows the field dependence of the precession frequency in a 100-nm thick LCMO/NGO film with the applied field both in the plane of the sample and almost normal to it. The main difference from the frequencies measured in LCMO/STO is a finite frequency at fields as low as 0.01 T, which can be extrapolated to a finite precession frequency at zero field, although measurements at zero field are not always successful. The finite zero-field frequency in the out-of-plane measurement (Fig. 5.4(b))

Reproduced with permission of the copyright owner. Further reproduction prohibited without permission.

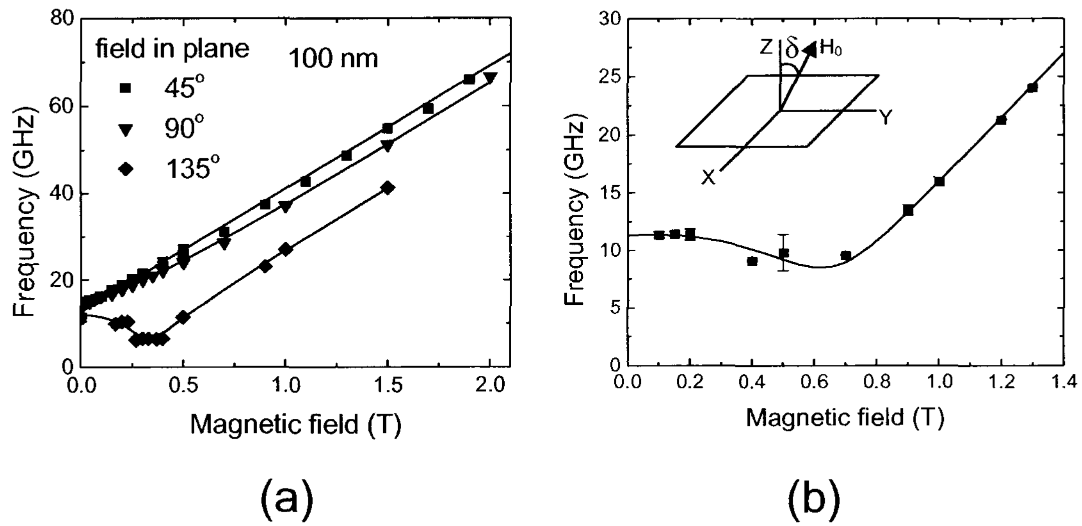

Fig. 5.4: Field dependence of precession frequency in LCMO/NGO, in the 100 nm* sample in Table 5.2. Solid lines are calculated using the expressions given by Eq. (5.2), (5.6) and (5.7) with the effective fields given in Table 5.2 and g-factor of 1.98. (a) Applied magnetic field is in plane. The $\delta = 45^o$, $\delta = 90^o$, and $\delta = 135^o$ orientations correspond to the field along the in-plane uniaxial easy-axis, at 45° to the easy axis, and along the in-plane uniaxial hard axis, respectively. δ is defined in Fig. 5.2. (b) Applied magnetic field is almost normal to the film and lies in the Y- Z plane, with Y being the uniaxial easy axis.

can be explained by a large positive in-plane tetragonal anisotropy constant $K_{||}$ in Eq. (5.1). The introduction of such a term leads to a pronounced four-fold symmetry in the in-plane magnetic properties. To verify that prediction, we study the frequency-field dependence as a function of the in-plane direction of the applied field (angle δ in Fig. 5.2(a)) and reveal a two-fold in-plane symmetry (Fig 5.4(a)). The field-dependent frequencies reach a maximum when we apply the magnetic field along a certain direction and a minimum upon rotation of the sample by 90°. The maximum-frequency direction corresponds to the 45° field angle and the minimum-frequency direction to the 135° field angle in Fig 5.4(a), representing the [110] and [1-10] crystallographic directions,

Reproduced with permission of the copyright owner. Further reproduction prohibited without permission.

respectively. The observed two-fold symmetry requires the introduction of two-fold symmetry terms in the magnetic free energy given by Eq. (5.1). The lowest-order anisotropy with required symmetry is an easy in-plane axis and has the form $-K_u M_{y'}^2 / M_s^2$, where $M_{y'}$ is the component of the magnetization along the easy direction y'. We achieve the best agreement between the calculated frequencies and the measured ones when the direction of y' is chosen to be along the maximum-frequency direction of Fig. 5.4(a) ([110] direction) and introduce a small biaxial anisotropy with easy axes along the [100] and [010] directions. According to Eq. (5.1), the X and Y directions in Fig. 5.2 are biaxial easy axes when $K_{||} > 0$. Then the direction of y' is at 45° to both X and Y. The uniaxial in-plane anisotropy energy acquires the form $-K_u[M_x M_y + 1/2(M_x^2 + M_y^2)]/M_s^2$, and the total free energy reads

$$\begin{aligned} E = & -H_0 \cdot M + 2\pi M_z^2 + K_a M_z^2 / M_s^2 - K_{//}(M_x^4 + M_y^4)/2M_s^4 - K_\perp M_z^4 / 2M_s^4 \\ & - K_u[M_x M_y + 1/2(M_x^2 + M_y^2)]/M_s^2 \end{aligned} \tag{5.5}$$

We introduce the in-plane uniaxial anisotropy field as $H_u = 2K_u/M_s$.

The precession frequency corresponding to the free energy given by Eq. (5.5) is described by Eq. (5.2) with a and b given by:

$$\begin{aligned} a &= H_0 \cos(\delta - \varphi) + H_d + H_a + \frac{H_u}{2}(1 + \sin 2\varphi) + H_{//}(\sin^4 \varphi + \cos^4 \varphi) \\ b &= H_0 \cos(\delta - \varphi) + H_u \sin 2\varphi + H_{//} \cos(4\varphi) \end{aligned}, \tag{5.6}$$

when the applied field is in the film plane (Fig. 5.4 (a)); and

$$\begin{aligned} a &= H_0 \cos(\delta - \theta) - (H_d + H_a + H_u)\cos 2\theta + H_\perp \cos^2 \theta \cos 2\theta \\ b &= H_0 \cos(\delta - \theta) - (H_d + H_a)\cos^2 \theta + H_u \sin^2 \theta + H_\perp \cos^4 \theta \end{aligned}, \tag{5.7}$$

when the applied field is in the Y-Z plane (Fig. 5.4 (b)).

Reproduced with permission of the copyright owner. Further reproduction prohibited without permission.

TABLE 5.2: Anisotropy field values deduced from fits to the field dependence of the precession frequency in LCMO/NGO films. 100 nm* sample - measurements in Fig. 5.4. 60 nm, 100 nm, and 150 nm samples - measurements in Fig. 5.5.

sample	H_d (T)	H_a (T)	$H_\perp$ (T)	$H_{//}$ (T)	H_u (T)
100 nm*	0.72	-0.37+/-0.15	-0.08	0.003+/-0.006	0.31+/-0.01
60 nm	0.72	-0.17+/-0.25		0.01+/-0.06	0.20+/-0.10
100 nm	0.72	-0.25+/-0.21		-0.03+/-0.05	0.19+/-0.02
150 nm	0.72	-0.26+/-0.25		-0.03+/-0.04	0.09+/-0.07

Frequencies calculated using the described model are shown by solid lines in Fig. 5.4, and the parameters derived from least-square fits are given in Table 5.2. These parameters are average values obtained from fitting the measurements with different orientations of the applied field for a single sample. The largest anisotropy terms in the 100-nm film are the easy normal-to-plane axis with $K_a = -1.1 \times 10^5$ J/m^3 and the easy in-plane axis at 45° to Mn-O bonds with $K_u = 0.9 \times 10^5$ J/m^3. The perpendicular easy axis anisotropy has been observed in the study of magnetization dynamics in LSMO/NGO (section 5.3), where it has been attributed to the uncertainty in the saturation magnetization that affects H_d and/or to the interface anisotropy. The perpendicular easy axis is not in contradiction with the symmetry of the film and the underlying substrate. The (110) plane of the orthorhombic NGO crystal corresponds to the (001) plane of the pseudo-cubic unit cell, and the LCMO film on (110) NGO grows in the (001) orientation due to the good match of the lattice parameters [129].

Reproduced with permission of the copyright owner. Further reproduction prohibited without permission.

The pseudocubic symmetry of LCMO and NGO and the lattice mismatch of only 0.1% between them suggest that the stress and the stress anisotropy are negligible. Therefore, the observed in-plane uniaxial anisotropy must be magnetocrystalline. To clarify the origin of the uniaxial anisotropy, we perform the TR-MOKE measurements on LCMO/NGO films of different thicknesses with magnetic field applied in the plane of the film. The recorded field dependence of the precession frequency for the films of 60 nm, 100 nm, and 150 nm thickness is shown in Fig. 5.5. The solid lines in the Figure show the calculated frequencies and Table 5.2 displays the deduced fitting parameters. The values in the Table are averages over the measurements with different orientations of the applied field performed on the same sample. The two-fold in-plane symmetry is clearly present in these samples, as evidenced by the different behavior of the precession frequency when the applied field is in the 45° orientation (along the easy axis) and in the 135° orientation (along the hard axis). The magnitude of the anisotropy field is almost the same in the 60-nm and 100-nm films and is diminished significantly in the 150-nm film. Despite the observed variation of the anisotropy field in the films of the same thickness (100 nm), the trend of the decreasing anisotropy field with increasing film thickness is well established. A lower magnetic anisotropy in thicker films is well explained when the anisotropy is strain-induced. In our LCMO/NGO films the amount of strain is negligible. Therefore, the lower anisotropy in the 150-nm film may result from the interfacial origin of the anisotropy. If the surface energy density of the interface uniaxial anistropy is K_s, then the anisotropy enters the expression for the volume energy density as a term proportional to $K_u = K_s/d$, where d is the film thickness [130]. Thus, K_u is reduced in thicker films.

Reproduced with permission of the copyright owner. Further reproduction prohibited without permission.

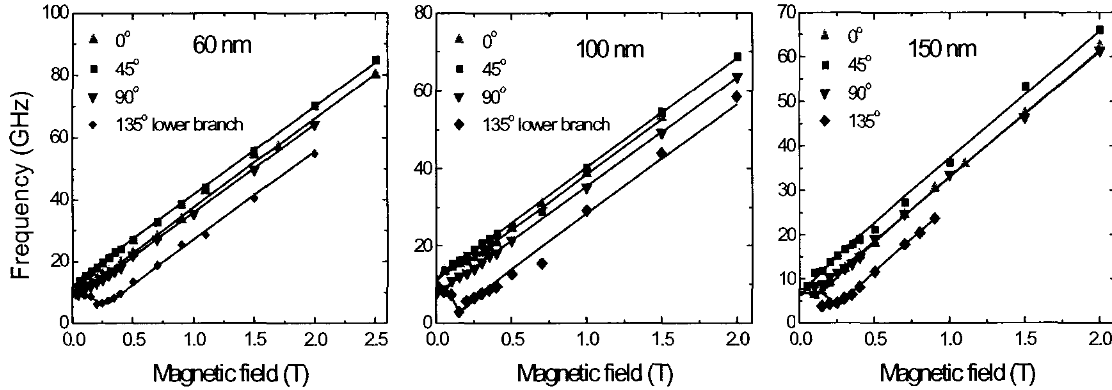

Fig. 5.5: Field dependence of precession frequency in LCMO/NGO, in the 60 nm, 100 nm, and 150 nm samples in Table 5.2. Solid lines are calculated using the expressions given in the Eq. (5.2) and (5.6) with effective fields given in Table 5.2 and *g*-factor of 1.98. Applied magnetic field is in plane. In each panel $\delta = 45^o$, $\delta = 90^o$, and $\delta = 135^o$ orientations correspond to the field along the in-plane uniaxial easy-axis, at 45° to the easy axis, and along the in-plane uniaxial hard axis, respectively. δ is defined in Fig. 5.2.

The in-plane uniaxial anisotropy in LCMO/NGO films was observed by Mathur *et al* [131] in static magnetization measurements. Mathur *et al* measured the anisotropy constant of 0.36×10^5 J/m^3 with the easy direction at 45° to Mn-O bonds, which coincides with the easy axis in our measurements. Mathur and collaborators argue that the anisotropy is substrate-induced and magnetocrystalline, although no specific anisotropy mechanism is described in their report. We believe that our and Mathur's observations document the same phenomenon. The crystallographic structure of NGO [132,133] is orthorhombic with a $GdFeO_3$-type rotation of oxygen octahedra about the pseudocubic [111] direction. The rotation results in the modification of the pseudocubic (001) face of the substrate, causing the pseudocubic [110] diagonal to be different from the [1-10] diagonal. This could result in the described interface uniaxial anisotropy because oxygen environment of the Mn ions at the interface is different from that in the bulk. A similar

Reproduced with permission of the copyright owner. Further reproduction prohibited without permission.

magnetic anisotropy could be anticipated in LSMO/NGO films. The study of magnetization precession in LSMO [section 5.3] does not give any evidence of a uniaxial in-plane anisotropy, although its presence cannot be ruled out because the precession with in-plane magnetic field has not been studied and the thickness of the studied films (160 nm) is higher than the thickness of the LCMO/NGO films.

5.3 Magnetization precession and magnetic anisotropy in LSMO films

The LSMO films are 160 nm thick and grown by pulsed laser deposition on three different substrates: NdGaO3 (110), SrTiO3 (100), and LaAlO3 (100). Resistivity of the films as a function of temperature (T< 300 K) was measured and the metallic behavior of the films confirmed.

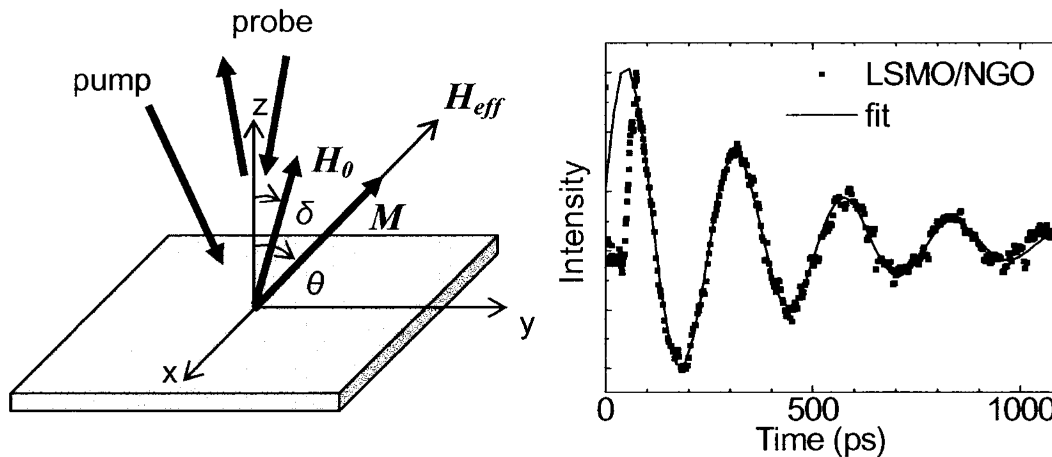

Fig. 5.6: (a) Geometry of the pump-probe measurement in the applied magnetic field. (b) Magnetization precession as seen by TR-MOKE in LSMO/NGO at T = 170 K and B = 0.5 T.

Reproduced with permission of the copyright owner. Further reproduction prohibited without permission.

Magnetization precession is measured in the geometry of perpendicular resonance (Fig. 5.6 (a)) [134]. A typical time evolution of precession dynamics is shown in Fig. 5.6 (b).The solid line indicates a fit that yields the precession frequency ω and the damping rate Γ defined by $M_z \sim \exp(i\omega t - \Gamma t)$. The field dependence of the frequency in LSMO/NGO is shown in Fig. 5.7, which includes a comparison with FMR data of Lyfar *et al* [135] and shows that the precession frequency deduced from TR-MOKE coincides with frequencies observed in FMR. FMR, however, does not allow studying the field dependence of the resonance frequency because those measurements are performed at one or few fixed driving frequencies.

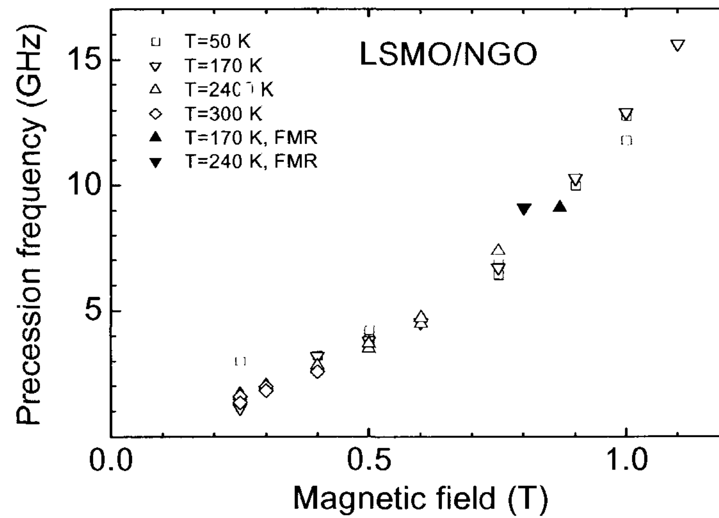

Fig. 5.7: Field dependence of precession frequency in LSMO/NGO for different temperatures.

The magnetic free energy in LSMO film can be described by

$$E = -H_0 M_s \cos(\theta - \delta) + 2\pi M_s^2 \cos^2\theta + K_a \sin^2\theta \tag{5.8}$$

Reproduced with permission of the copyright owner. Further reproduction prohibited without permission.

The first term in the energy E is the Zeeman energy and the second term is the anisotropy energy consisting of the shape anisotropy $2\pi M_s^2 \cos^2\theta$ and the uniaxial anisotropy $K_a \sin^2\theta$. The corresponding phenomenological fields are $H_d = 4\pi M_s$ and $H_a = 2K_a/M_s$. Easy-plane anisotropy corresponds to $H_a < 0$, while $H_a > 0$ for easy normal-to-plane axis. Looking for a solution of the LLG equation in the form $M_z \sim exp(i\omega t - \Gamma t)$, we find that

$$\omega^2 + \Gamma^2 = \frac{\gamma^2 ab}{1+(\alpha/\gamma M_s)^2} \approx \gamma^2 ab, \tag{5.9}$$

where $a = H_0 \cos(\theta-\delta)-(H_d-H_a)\cos 2\theta$, $b = H_0 \cos(\theta-\varphi)-(H_d-H_a)\cos^2\theta$, and assuming $\alpha/\gamma M_s << 1$. The precession relaxation rate Γ is field-dependent and proportional to the Gilbert damping parameter: α

$$\Gamma = \frac{\alpha(a+b)}{2M_s(1+(\alpha/\gamma M_s)^2)} \approx \frac{\alpha(a+b)}{2M_s}. \tag{5.10}$$

The relaxation rates Γ determined from fits to the precessing magnetization (Fig. 5.6(b)) are in the 1 - 10 $\times$ $10^9 s^{-1}$ range for all substrates at different temperatures and fields. Elucidation of the field and temperature dependence of α and of its microscopic origin requires further measurements.

Figure 5.8 shows the field dependence at T=50 K of the quantity $\omega^2+\Gamma^2$ for films grown on different substrates. The solid lines represent a fit using Eq. (5.9) and assuming a demagnetization field of $H_d = 0.72$ T [136]. The field H_a is the only parameter of the calculation and is different for each substrate, indicating a dependence on the strain induced in the film. STO substrate induces tensile strain, LAO - compressive strain, and NGO - almost no strain. The values of H_a deduced from the fits are presented in Table 5.3. The anisotropy has opposite sign for films grown on STO and LAO ($H_a < 0$ and $H_a > 0$, respectively), in agreement with the opposite sign of the induced strain. Qualitatively,

Reproduced with permission of the copyright owner. Further reproduction prohibited without permission.

the observed anisotropy is in agreement with previous studies of the role of strain in the anisotropy of manganite films [120,122,123]. O'Donnel *et al.* [122] and Ranno *et al.* [123] found an easy-plane strain-induced anisotropy in tensile-strained $La_{0.67}Ca_{0.33}MnO_3$/STO and LSMO/STO films. The constant K_a measured by Ranno *et al.* is about 2×10^5 J/m^3 for films thinner than 100 nm. Using $H_d = 0.72$ T based on the bulk magnetization data, we calculate $K_a = 0.6 \times 10^5$ J/m^3, which is within an order-of-magnitude agreement with the value of Ranno *et al.* The discrepancy results from the uncertainty of H_d and from our film being thicker than the critical thickness [123] of 100 nm, above which the strain in the film begins to relax. Although the NGO substrate does not strain the LSMO film, we find a finite field $H_a = 0.16$ T. This non-zero value of H_a may result from a different saturation magnetization in a thin film compared to bulk samples and/or from the surface anisotropy.

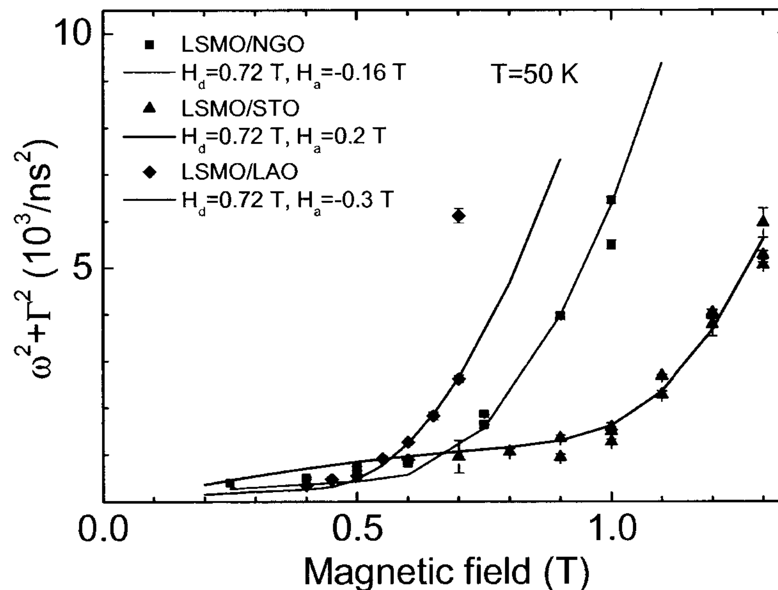

Fig. 5.8: Field dependence of precession frequency in LSMO films on different substrates:NGO (squares), STO (triangles), and LAO (diamonds). Solid lines are the fits to the corresponding data points.

Reproduced with permission of the copyright owner. Further reproduction prohibited without permission.

TABLE 5.3: Anisotropy field values deduced from fits to the field dependence of the precession frequency in LSMO films.

substrate	strain	Anisotropy field H_a
NGO	no strain	0.16 T
STO	tensile	-0.2 T
LAO	compressive	0.3 T

The sign of H_a with respect to strain is determined by the anisotropy energy of the occupied e_g orbital, since the local easy direction on each Mn^{3+} site is along that orbital. When the lattice is compressed, the in-plane distance between the Mn^{3+} and O^{2-} ions gets reduced, while the Mn^{3+}-O^{2-} distance along the plane normal is unchanged. The neighboring in-plane Mn^{3+}-O^{2-} pair can lower its energy when the oxygen p-electron in the orbital pointing toward Mn^{3+} delocalizes into an empty e_g orbital of Mn^{3+}, in which case the occupied e_g orbital is along the film normal. This description is consistent with the easy normal-to-plane axis found in compressively strained LSMO/LAO. In LSMO/STO, the Mn^{3+}-O^{2-} distance along the film normal becomes smaller than the in-plane distance, allowing the p-electron of oxygen to delocalize into an empty e_g orbital pointing along the normal. Therefore, the occupied e_g orbital has a lower energy when being in the plane of the film, in agreement with the easy-plane anisotropy observed in LSMO/STO [134].

Reproduced with permission of the copyright owner. Further reproduction prohibited without permission.

Summary

Optically induced magnetization precession in thin LCMO and LSMO films have been studied by TR-MOKE. The measured field dependence of the precession frequency is used to determine the parameters of magnetic anisotropy.

In tensile-strained LCMO/STO films, the dominant contribution is the strain-induced easy-plane anisotropy. In LCMO/NGO, the measurements reveal a strong in-plane uniaxial anisotropy with its easy direction at 45° to Mn-O bonds. The results suggest that the anisotropy originates from the LCMO/NGO interface, where the MnO_6 octahedra are different from those in the bulk of the film. The modification of the oxygen octahedra results from the $GdFeO_3$-type oxygen octahedron rotation in NGO. The uniaxial anisotropy in the LCMO/NGO system must be taken into account in the fabrication of magnetic tunnel junctions.

The precession frequency in LSMO films depends on the strain state of the films via the uniaxial anisotropy. Strain-induced single-ion anisotropy dominates the intrinsic anisotropy of the bulk LSMO and agrees with earlier static magnetization studies.

Reproduced with permission of the copyright owner. Further reproduction prohibited without permission.

Chapter 6

Band-Offsets at $CdCr_2Se_4$-(AlGa)As and $CdCr_2Se_4$-ZnSe Interfaces

The band discontinuities of $CdCr_2Se_4$–(AlGa)As and $CdCr_2Se_4$–ZnSe heterojunctions are measured to high resolution by internal photoemission using a widely tunable optical parametric amplifier system. The conduction band offsets ΔE_c = 560 meV and 530 meV at the $CdCr_2Se_4$– GaAs and $CdCr_2Se_4$– ZnSe interfaces are determined from the threshold energies of the photocurrent spectrum at room temperature.

6.1 Introduction

Ferromagnetic semiconductors (FMS) possess both semiconducting properties and spontaneous ferromagnetic order, making them attractive as magnetic contacts in spin-based electronics. An n-type FMS which can be epitaxially grown on a substrate relevant to current electronic device technology is especially attractive, since electron transport is the basis for high frequency, low power device operation. In addition, electrons have remarkably long spin lifetimes and spin-scattering lengths in materials such as Si [137], GaAs [7] and GaN [138].

Recently, the epitaxial growth of n-type $CdCr_2Se_4$, a chalcogenide spinel FMS, on GaAs(001) and GaP(001) has been demonstrated [139]. The use of this FMS as a spin

Reproduced with permission of the copyright owner. Further reproduction prohibited without permission.

injecting contact is a promising way to achieve high spin-injection efficiency for electrons at low magnetic field, since $CdCr_2Se_4$ shows strong ferromagnetism below the Curie temperature (T_c = 130 K) [140]. In addition, its semiconducting properties spontaneously circumvent the conductivity mismatch which may significantly reduce spin injection efficiency in diffusive regime.

However, the band discontinuity across the heterojunction interface is also an important parameter for efficient electrical spin injection. For electron injection, the conduction band (CB) offset should facilitate flow of electrons from the contact into the semiconductor. Accurate knowledge of the band discontinuity between $CdCr_2Se_4$ and the semiconductor is important for both design and application of spin injection devices. Internal photoemission (IPE) is a direct method to extract the energy band alignment of semiconductor heterojunctions. The band discontinuities produce thresholds in the photocurrent at photon energies when the carriers are photoexcited over the band offset barrier [45,141-143]. Photocurrent measurements are less sensitive to interface defects than, for example, capacitance–voltage or current–voltage techniques, thus this method is the most reliable for band offset measurements in semiconductor heterostructures [144]. Recently, direct and accurate band discontinuity measurements using the free-electron laser (FEL) IPE technique have been carried out for a variety of semiconductor heterostructures [48,49,145,146]. In this chapter, we investigate the conduction band offset in *n*-type $CdCr_2Se_4$-based semiconductor heterostructures by the internal photoemission technique using a widely tunable optical parametric amplifier (OPA) laser system. No complex model is required to extract the band offset from the experimental data, since the band discontinuity coincides with photocurrent threshold energy.

Reproduced with permission of the copyright owner. Further reproduction prohibited without permission.

6.2 Crystallographic, electronic and magnetic structure of $CdCr_2Se_4$

The semiconductor $CdCr_2Se_4$ is a direct band gap chalcogenide spinel with the AB_2X_4 structure (56 atoms per unit cell), in which the Se anions and Cd cations form interpenetrating face-centered-cubic lattices with the lattice constant of the latter twice that of the former [147]. The Cd cations occupy the tetrahedral sites formed by the Se sublattice, and the Cr cations occupy magnetically active octahedral sites. With a lattice constant of 10.721 Å, it is reasonably lattice-matched to technologically important materials such as Si and GaP (~1.7% tensile mismatch), and to GaAs (5.2% tensile mismatch).

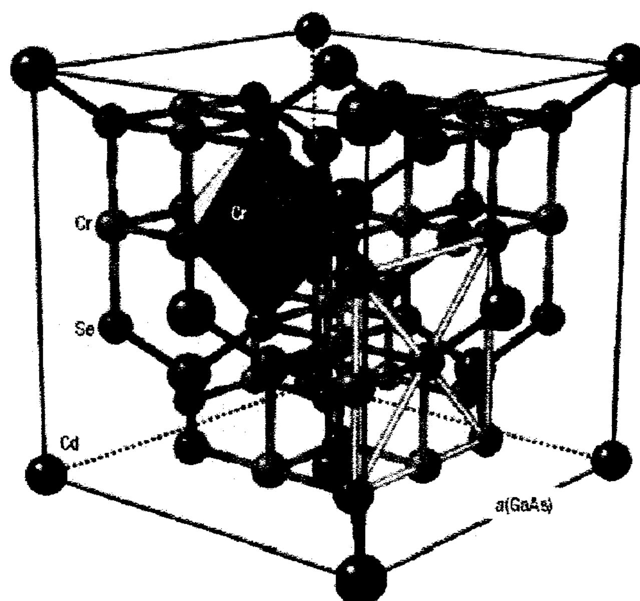

Fig. 6.1: Model of the crystal structure of bulk $CdCr_2Se_4$. Chromium atoms occupy octahedral sites defined by selenium ligands; one such octahedron is explicitly shown. [147]

Above the Curie Temperature T_c = 130 K, $CdCr_2Se_4$ displays paramagnetic properties typical of a nonmagnetic semiconductor, the absorption band edge increases

Reproduced with permission of the copyright owner. Further reproduction prohibited without permission.

with an decreasing temperature, as shown in Fig. 6.2. In contrast, the absorption band edge decreases with decreasing temperature below the T_c when it enters the ferromagnetic state [148].

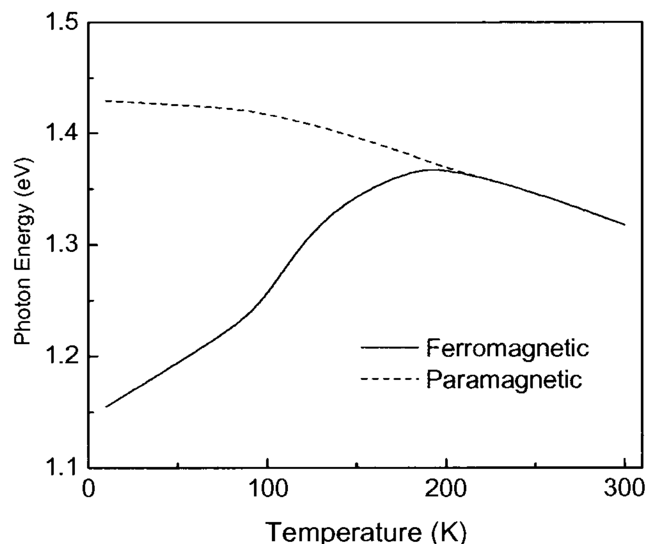

Fig. 6.2 Energy gap of $CdCr_2Se_4$ versus temperature. Dashed line assumed extrapolation for paramagnetic state. [148]

The main contribution to the $CdCr_2Se_4$ valence band is due to the d states of Cr highly hybridized with p states of Se. The s states coming from Cd, with negligible spin polarization, and unoccupied d states of Cr form the conduction band. A noticeable spin polarization is present on the Cr site: the states (i.e., lying below the Fermi level) occupied in the majority component are many more than the occupied states in the minority component. This will result in a large magnetic moment on the Cr site (~2.9 μ_B per atom) [149]. Figure 6.3 shows theoretical densities of states (DOS) calculated within local density approximation (LDA) to density-functional theory [147]. An expanded view

Reproduced with permission of the copyright owner. Further reproduction prohibited without permission.

is shown in the inset, and reveals that the bottom of the conduction band is dominated by minority spin electrons whose moment is antiparallel to that of the net film magnetization.

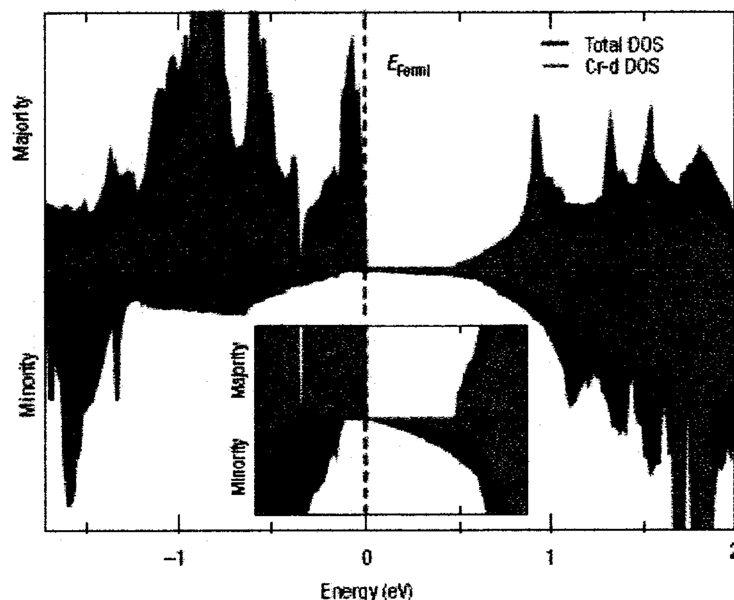

Fig. 6.3 Theoretical densities of states (DOS) of bulk $CdCr_2Se_4$ calculated within LDA. The inset shows the density of states near the bandgap. Minority spin states dominate the conduction-band edge. [147]

6.3 Sample preparation

The samples studied are quantum-well (QW) light emitting diode (LED) structures grown by molecular beam epitaxy. The samples are provided by Dr. Berend Jonker's group at NRL. For the $CdCr_2Se_4$–$Al_{0.09}Ga_{0.91}As$ heterostructure, a highly doped *p*-type AlGaAs layer is first grown on top of a p^+-GaAs substrate. An AlGaAs/GaAs QW is then grown followed by a 250-Å-thick lightly doped *n*-type $Al_{0.09}Ga_{0.91}As$ layer with a 1000-Å-thick *n*-type $CdCr_2Se_4$ layer on top. For the $CdCr_2Se_4$– GaAs heterostructure, an InGaAs QW is grown on a p^+-GaAs buffer layer followed by a 250-Å-thick lightly doped

Reproduced with permission of the copyright owner. Further reproduction prohibited without permission.

n-type GaAs layer with a 1000-Å-thick *n*-type $CdCr_2Se_4$ layer on top. For the $CdCr_2Se_4$–ZnSe heterostructure, a highly doped *p*-type AlGaAs layer is first grown on top of a p^+-GaAs substrate. An AlGaAs/GaAs QW is then grown followed by a 250-Å-thick lightly doped *n*-type $Al_{0.09}Ga_{0.91}As$ layer, a 500-Å-lightly doped *n*-type ZnSe layer, followed by a 1000-Å-thick *n*-type $CdCr_2Se_4$ layer on top. A metallic bullseye pattern is evaporated on top of the $CdCr_2Se_4$ to make ohmic contacts and provide optical access. The LED structure is mounted on a chip carrier and the contacts of the LED are wire bonded to the pads on the chip carrier.

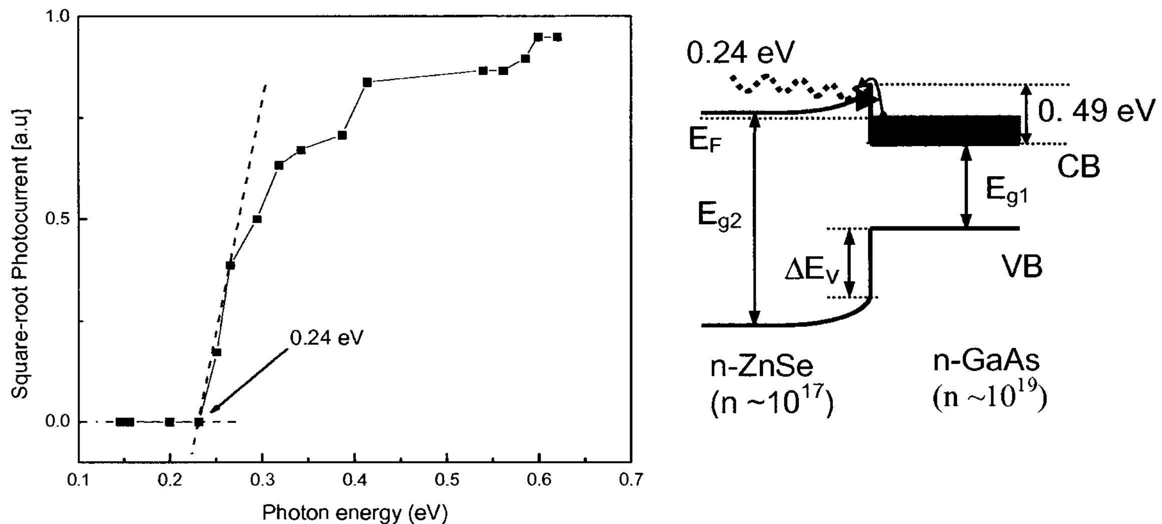

Fig. 6.4: (a) IPE spectra at room temperature from unbiased ZnSe/GaAs heterojunctions. (b) The band alignment across the heterointerface.

A ZnSe/GaAs heterostructure in which the ZnSe growth was initiated by exposure to the Se flux served as a reference sample. We observe the threshold of the photocurrent occurs at 0.24 eV (Fig. 6.4). Since the GaAs is heavily doped ($n=10^{19}$ cm^{-3}), its Fermi

Reproduced with permission of the copyright owner. Further reproduction prohibited without permission.

level is ~0.25 eV above the CB. Thus the CB offset is determined to be 490 meV, consistent with literature values.

6.4 Band-offsets at $CdCr_2Se_4$–(AlGa)As and $CdCr_2Se_4$–ZnSe interfaces

The IPE spectrum from the $CdCr_2Se_4$–$Al_{0.09}Ga_{0.91}As$ heterojunction is shown in Fig. 6.5(a). The incident photons are absorbed in the AlGaAs layer and stimulate electronic transitions from the conduction band to higher energy states. At sufficiently high energy, these electrons can surmount the potential barrier at the $CdCr_2Se_4$–AlGaAs heterointerface and can be collected, generating a measurable photocurrent. The threshold of the photocurrent occurs near the photon energy of 650 meV, and corresponds to the CB offset between $CdCr_2Se_4$ and AlGaAs. The threshold energy is determined with a resolution <10 meV by extrapolation of a power law fit to the data [47]. A square-root dependence of the photocurrent with photon energy is used assuming direct optical excitation with elastic scattering for the photoemission process. However, the threshold energy was found to be rather insensitive to the incident power. A base line on the lower photon energy side is assumed. The threshold energy does not shift under a small forward or reverse bias voltage applied to the heterostructure. This indicates that the band bending formed at the heterostructure interface has no influence on the measured band offset.

In low-temperature electroluminescence (EL) measurements, we note this LED structure shows a broad bulk recombination band but no QW exciton line. This suggests that electrons injected from the $CdCr_2Se_4$ conduction band have a high kinetic energy and therefore overshoot the GaAs QW, consistent with the 650 meV threshold observed in the IPE spectrum. The inset in Fig. 6.5(a) shows the band alignment at the $CdCr_2Se_4$–$Al_{0.09}Ga_{0.91}As$ heterojunction.

Reproduced with permission of the copyright owner. Further reproduction prohibited without permission.

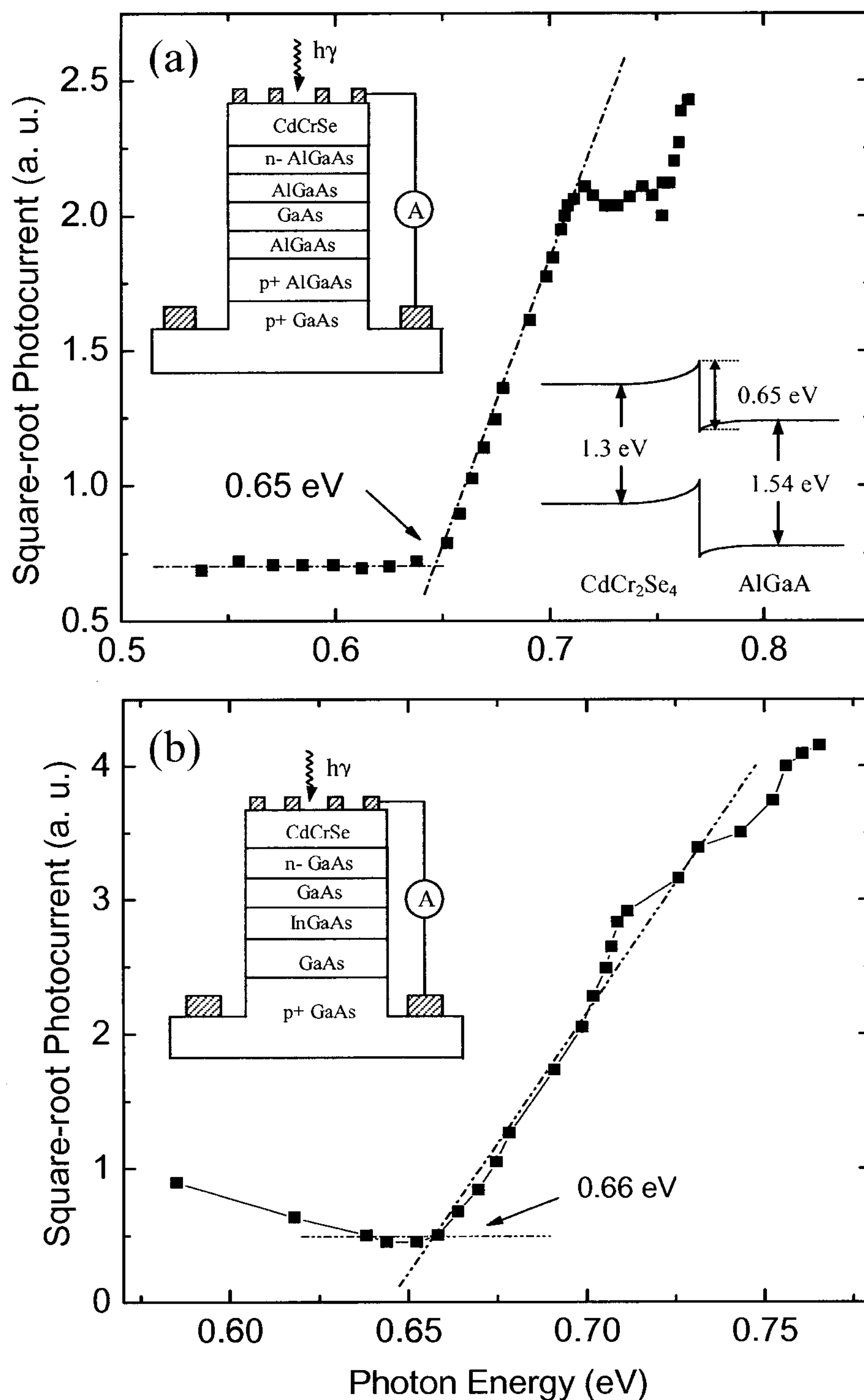

Fig. 6.5: IPE spectra at room temperature from unbiased heterojunctions: (a) $CdCr_2Se_4$/AlGaAs, and (b) $CdCr_2Se_4$/GaAs. The insets show the cross section of the LED and the band alignment.

Reproduced with permission of the copyright owner. Further reproduction prohibited without permission.

Figure 6.5(b) shows the IPE spectrum from the $CdCr_2Se_4$–GaAs heterojunction. A threshold energy and CB offset of 660 meV is obtained, with a corresponding band alignment similar to that shown in Fig. 6.5(a). This result is in excellent agreement with the 650-meV-CB offset at the $CdCr_2Se_4$–$Al_{0.09}Ga_{0.91}As$ heterojunction. The valence band (VB) offset can be determined if the band gaps are known. Various techniques have been used to determine the band gap of $CdCr_2Se_4$. An optical absorption edge is reported around 1.3 eV [150,151]. Using 1.3 eV as the fundamental band gap of $CdCr_2Se_4$ and a well known band gap of 1.42 eV for GaAs at room temperature, we obtain 780 meV for the VB offset between $CdCr_2Se_4$ and GaAs. As before, there is no shift of the threshold energy under small forward or reversed bias voltage applied to the structure.

The use of $CdCr_2Se_4$ as a spin injection contact represents a promising avenue for spin injection devices. Recently, Kioseoglou *et al* reported on electrical spin injection from $CdCr_2Se_4$ into $Al_{0.09}Ga_{0.91}As$ [147]. The magnitude of the injected spin polarization measured in the GaAs quantum well (6%) is much smaller than expected from band-structure calculations which indicate that the $CdCr_2Se_4$ conduction-band spin polarization should be nearly 100%. The band offset and interface defects are two major factors that may reduce spin polarization for transport across such heterointerface. Since the $CdCr_2Se_4$ CB edge lies at least 0.6 eV high above the bottom of the GaAs conduction band, electrons injected into GaAs have high kinetic energy which dissipate by non-spin-conserving mechanism, lowering the spin polarization. Therefore, a smaller energy band offset is desirable to maintain maximum spin alignment of the carriers. Since the conduction band offset of semiconductor heterostructures depends on details of the

Reproduced with permission of the copyright owner. Further reproduction prohibited without permission.

interface bonding and stoichiometry, an additional ZnSe interlayer may provide a smaller conduction band offset in $CdCr_2Se_4$–(AlGa)As heterostructures.

Figure 6.6 shows the photocurrent spectrum from a $CdCr_2Se_4$/ZnSe/ (AlGa)As–GaAs LED structure. The threshold of the photocurrent occurs near a photonic energy of 530 meV corresponding to the CB offset at the CdCr2Se4– ZnSe interface. We note that this CdCrSe-based LED structure showed the QW exciton line indicating that the CB offset has been reduced successfully (Fig. 6.6 (b)).

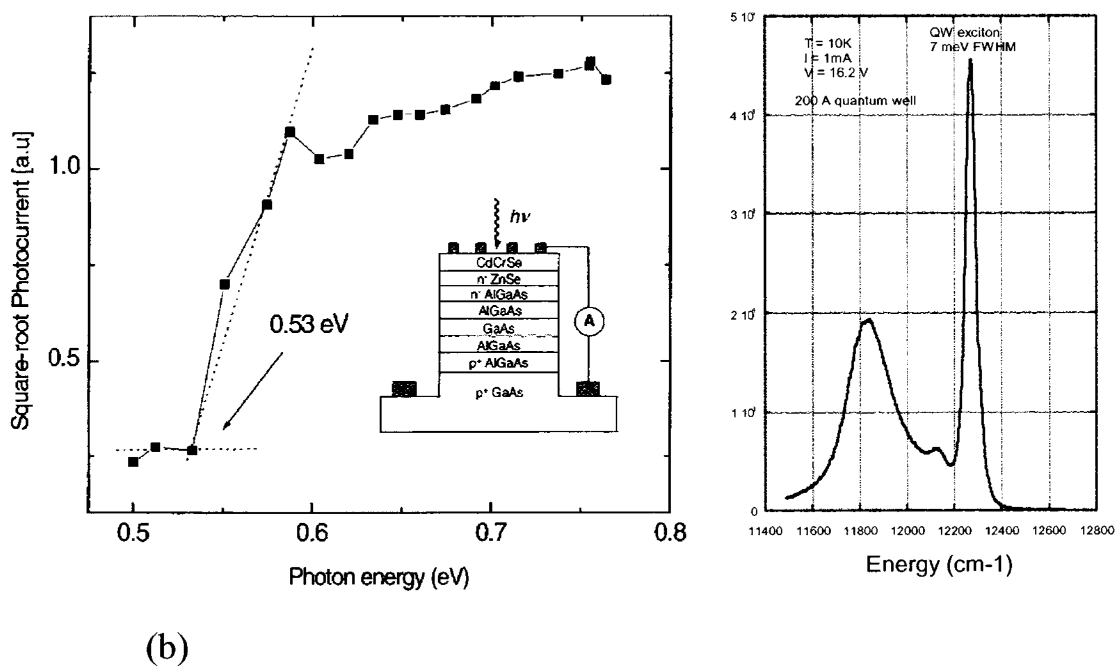

Fig. 6.6: (a) IPE spectrum from the unbiased $CdCr_2Se_4$/ZnSe heterojunction at room temperature. The inset shows the cross section of the LED. (b) QW luminescence spectrum at T=10 K.

Reproduced with permission of the copyright owner. Further reproduction prohibited without permission.

Summary

The band discontinuities of $CdCr_2Se_4$-(AlGa)As and $CdCr_2Se_4$-ZnSe heterojunctions are measured to high resolution by internal photoemission using a widely tunable optical parametric amplifier system. The conduction band offsets $\Delta E_c = 660$ meV and 530 meV at the $CdCr_2Se_4$-GaAs and $CdCr_2Se_4$-ZnSe interfaces, respectively, are determined from the threshold energies of the photocurrent spectrum at room temperature. The large band offset at $CdCr_2Se_4$-AlGaAs may account for the small magnitude of injected spin polarization measured in the GaAs quantum well. The band offset can be reduced by engineering interface bonding and stoichiometry.

Reproduced with permission of the copyright owner. Further reproduction prohibited without permission.

Chapter 7

Conclusions

The interface magnetization in ferromagnetic heterostructures and its ultrafast dynamics play an important role for the development of the next generation of spintronic devices. In this thesis, the MSHG technique is applied for studying the interface magnetic properties in a noncentrosymmetric hybrid structure – Fe/AlGaAs. By judicious selection of polarization combination, a large nonlinear magneto-optical response is obtained from Fe/AlGaAs, leading to high sensitivity of MSHG to the interface magnetization. The reversal process of the interface magnetization is found to be distinctly different from that of the bulk magnetization in Fe/AlGaAs (001) – single step switching occurs at the interface layer, whereas two-jump switching occurs in the bulk Fe. The interface and bulk magnetization is essentially decoupled due to the large difference in the magnetic anisotropy and reduced perpendicular exchange interaction arising from the specific bonding and tetragonal distortion at the interface. In contrast, the interface magnetization in Fe/AlGaAs (110) is rigidly coupled to the bulk, indicating a large exchange interaction between the interface layer and the bulk Fe. The different behavior reveals a strong impact of the electronic structure on the magnetic interaction in this hybrid structure.

The time-resolved MSHG technique is utilized to study the ultrafast magnetization dynamics at the interface. A coherent precession of interfacial electron

Reproduced with permission of the copyright owner. Further reproduction prohibited without permission.

spins is observed in the Fe/AlGaAs (001), implying the feasibility of fast precessional control of interface magnetization. The field dependence of precession frequencies enables us to quantitatively analyze the magnetic anisotropy fields at the interface. Large perpendicular anisotropy fields may contribute to the higher spin precessional frequencies at the interface than in the bulk. This can be utilized to achieve a faster precessional switching in nanostructures where interface properties dominate.

Furthermore, the excitations of uniform precession of bulk magnetization are observed along all the in-plane directions in the Fe film. The time evolution of magnetization precession enables the direct determination of the damping parameters. This presents an obvious advantage compared to the non-time resolved techniques, in which the damping can only be obtained indirectly form the broadened absorption spectra. Moreover, spin wave excitations are observed in the thick Fe film, providing complementary information to describe the low order standing spin waves and the effective exchange coupling.

This thesis also presents a detailed study of photo-induced magnetization precession in half-metallic LSMO and LCMO films grown on different substrates including NGO, STO, and LAO. The interface bonding and strain induce a pronounced effect on the magnetic anisotropy fields and uniform spin precession in the thin magnetic films. The directional bonding at the LCMO/NGO film causes a strong in-plane uniaxial magnetic anisotropy field which results in a finite precession frequency at zero field. The tensile strain in LCMO and LSMO films grown on STO substrates gives rise to an easy-plane magnetic anisotropy field, lowering the precession frequency at high fields. In contrast, the compressive strain induced by the LAO substrate leads to an easy normal-to-

Reproduced with permission of the copyright owner. Further reproduction prohibited without permission.

plane axis, significantly enhancing the precession frequencies. These phenomena must be taken into account in the fabrication of magnetic tunnel junctions.

Moreover, a table top internal photoemission system has been developed to study the conduction band-offset across the heterointerfaces. The widely tunable optical parametric amplifier is used as the bright light source in the IPE setup. A high band-offset across the $CdCr_2Se_4$/AlGaAs interface is observed, which is detrimental to the spin dependent transport. The band offset is successfully reduced by engineering of the interface bonding and stoichiometry.

Reproduced with permission of the copyright owner. Further reproduction prohibited without permission.

BIBLIOGRAPHY

1. S. A. Wolf, D. D. Awschalom, R. A. Buhrman, J. M. Daughton, S. von Molnar, M. L. Roukes, A. Y. Chtchelkanova, D. M. Treger, Science **294**, 1488 (2001).

2. Gary A. Prinz, Science **282**, 1660 (1998).

3. B. T. Jonker, Proc. IEEE **91**, 727 (2003).

4. M. Baibich, J. M. Broto, A. Fert, F. Nguyen Van Dau, F. Petroff, P. Eitenne, G. Creuzet, A. Friederich, and J. Chazelas, Phys. Rev. Lett. **61**, 2472 (1988).

5. J. S. Moodera Lisa R. Kinder, Terrilyn M. Wong, and R. Meservey, Phys. Rev. Lett.**74**, 3273 (1995).

6. S. Datta, B. Das, Appl. Phys. Lett. **56**, 665 (1990).

7. J. M. Kikkawa, and D. D. Awschalom, Phys. Rev. Lett. **80**, 4313 (1998).

8. D. Hagèle, M. Oestreich, W. W. Rühle, N. Nestle, and K. Eberl, Appl. Phys. Lett. **73**, 1580 (1998).

9. J. M. Kikkawa, and D. D. Awschalom, Nature, **397**, 139 (1999).

10. M. Paillard, X. Marie, P. Renucci, T. Amand, A. Jbeli, and J. M. Gerard, Phys. Rev. Lett. **86**, 1634 (2001).

11. D. Gammon, E. S. Snow, B. V. Shanabrook, D. S. Katzer, and D. Park, Science **273**, 87 (1996).

12. R. Fiederling, M. Kelm, G. Reuscher, W. Ossau, G. Schmidt, A. Waag, and L. W. Molenkamp, Nature **402**, 787 (1999).

13. B. T. Jonker, Y. D. Park, B. R. Bennett, H. D. Cheong, G. Kioseoglou, and A. Petrou, Phys. Rev. B **62**, 8180 (2000).

14. H. Ohno, Science **281**, 951 (1998).

15. P. R. Hammar, B. R. Bennett, M. J. Yang, and M. Johnson, Phys. Rev. Lett. **83**, 203 (1999).

Reproduced with permission of the copyright owner. Further reproduction prohibited without permission.

16. G. Schmidt, D. Ferrand, L. W. Molenkamp, A. T. Filip, and B. J. van Wees, Phys. Rev. B **62**, R4790 (2000).

17. D. L. Smith, and R. N. Silver, Phys. Rev. B **64**, 045323 (2001).

18. E. I. Rashba, Phys. Rev. B **62**, R16267 (2000).

19. A. T. Hanbicki, O. M. J. van 't Erve, R. Magno, G. Kioseoglou, C. H. Li, B. T. Jonker, G. Itskos, R. Mallory, M. Yasar, and A. Petrou, Appl. Phys. Lett. **82**, 4092 (2003).

20. X. Jiang, R. Wang, R. M. Shelby, R. M. Macfarlane, S. R. Bank, J. S. Harris, and S. S. P. Parkin, Phy. Rev. Lett. **94**, 056601 (2005).

21. S. H. Chun, S. J. Potashnik, K. C. Ku, P. Schiffer, and N. Samarth, Phys. Rev. B **66**, 100408(R) (2002).

22. R. A. de Groot, F. M. Mueller, P. G. van Engen and K. H. J. Buschow, Phys. Rev. Lett. **50,** 2024 (1983).

23. R. M. Stroud, A. T. Hanbicki, Y. D. Park, G. Kioseoglou, A. G. Petukhov, B. T. Jonker, G. Itskos, and A. Petrou, Phys. Rev. Lett. **89**, 166602 (2002).

24. J. Z. Sun, W. J. Gallagher, P. R. Duncombe, L. Krusin-Elbaum, R. A. Altman, A. Gupta, Yu Lu, G. Q. Gong, and Gang Xiao, Appl. Phys. Lett. **69**, 3266 (1996).

25. M. Bowen, M. Bibes, A. Barthélémy, J.-P. Contour, A. Anane, Y. Lemaître, and A. Fert, Appl. Phys. Lett. **82**, 233 (2003).

26. M. Izumi, Y. Ogimoto, Y. Okimoto, and T. Manako, P. Ahmet, K. Nakajima, and T. Chikyow, M. Kawasaki, and Y. Tokura, Phys. Rev. B **64**, 064429 (2001).

27. R. Meservey and P. M. Tedrow, Phys. Rep. **238**, 173 (1994).

28. J. M. D. Teresa, A. Barthélémy, A. Fert, J. P. Contour, F. Montaigne, and Pierre Seneor, Science **286**, 507 (1999).

29. M. Sharma, S. X. Wang, J. H. Nickel, Phys. Rev. Lett. **82**, 616 (1999).

30. W. H. Butler, X.-G. Zhang, Xindong. Wang, Jan van Ek, and J. M. MacLaren, J. Appl. Phys. **81**, 5518 (1997).

31. D. Nguyen-Mahn *et al.*, Mat. Res. Soc. Symp. Proc. **492**, 319 (1998).

32. Th. Gerrits, H. A. M. Van den Berg, J. Hohlfeld, L. Bär, and Th. Rasing, Nature **418**, 509 (2002).

Reproduced with permission of the copyright owner. Further reproduction prohibited without permission.

33. S. I. Kiselev, J. C. Sankey, I. N. Krivorotov, N. C. Emley, M. Rinkoski, C. Perez, R. A. Buhrman, and D. C. Ralph, Phys. Rev. Lett. **93**, 036601 (2004).

34. L. D. Landau and E. M. Lifshtz, *Electrodynamics of Continuous Media* (Pergamon, London, 1960).

35. Z. Q. Qiu, and S. D. Bader, Rev. Sci. Instrum. **71**, 1243 (2000).

36. J. M. Florczak and E. D. Dahlberg, J. Appl. Phys. **67**, 7520 (1990).

37. C. Daboo, J. A. C. Bland, R. J. Hicken, A. J. R. Ives, and M. J. Baird, and M. J. Walker, Phys. Rev. B **47**, 11852 (1993).

38. Th. Rasing, Appl. Phy. B **68**, 477 (1999).

39. P. N. Argyres, Phys. Rev. **97**, 334 (1955).

40. P. Bruno, Y. Suzuki, and C. Chappert, Phys. Rev. B **53**, 9214 (1996).

41. Ru-Pin Pan, H. D. Wei and Y. R. Shen, Phys. Rev. B **39**, 1229 (1989).

42. U. Pustogowa, W. Hübner, and K. H. Bennemann, Phys. Rev. B **49**, 10031 (1994).

43. B. Koopmans, M. Groot Koerkamp, Th. Rasing and H. van den Berg, Phys. Rev. Lett. **74**, 3692 (1995).

44. S. M. Sze, Metal-Semiconductor Contacts, Physics of Semiconductor Devices (Wiley, New York, 1981), p 288.

45. M. A. Haase, M. J. Hafich, and G. Y. Robinson, Appl. Phys. Lett. **58**, 616 (1991).

46. H. Fowler, PR **38**, 45 (1931).

47. J. I. Pankove, *Optical Process in Semiconductors* (Dover, New York, 1971), p. 287.

48. C. Coluzza, E. Tumcel, J.-L. Staehli, P.A. Baudat, and G. Margaritondo, J. T. Mckinley, A. Ueda, A. V. Barnes, R. G. Albridge, N. H. Tolk, D. Martin, F. Morier-Genoud, C. Dupuy, A. Rudra and M. Ilegems, Phys. Rev. B **46**, 12834 (1992).

49. Kazuhisa Nishi, Hideaki Ohyama, Toshiji Suzuki, Tsuneo Mitsuyu and Takio Tomimasu, Appl. Phys. Lett. **70**, 2171 (1997).

50. A. T. Hanbicki, B. T. Jonker, G. Itskos, G. Kioseoglou, and A. Petrou, Appl. Phys. Lett. **80**, 1240 (2002).

51. S. C. Erwin, S.-H. Lee, and M. Scheffler, Phys. Rev. B **65**, 205422 (2002).

Reproduced with permission of the copyright owner. Further reproduction prohibited without permission.

52. M. Gruyters, T. Bernhard, and H. Winter, Phys. Rev. Lett. **94**, 227205 (2005).

53. J. C. Slonczewski, J. Appl. Phys. **73**, 5957 (1993).

54. E. M. Kneedler, B. T. Jonker, P. M. Thibado, R. J. Wagner, B. V. Shanabrook, and L. J. Whitman, Phys. Rev. B **56**, 8163 (1997).

55. J. J. Krebs, B. T. Jonker, and G. A. Prinz, J. Appl. Phys. **61**, 2596 (1987).

56. E. Kneedler, P. M. Thibado, B. T. Jonker, B. R. Bennett, B. V. Shanabrook, R. J. Wagner, and L. J. Whitman, J. Vac. Sci. Technol. B **14**, 3193 (1996).

57. J. W. Freeland, I. Coulthard, and W. J. Antel, Jr. and A. P. J. Stampfl, Phys. Rev. B **63**, 193301 (2001).

58. J. M. Florczak, and E. D. Dahlberg, Phys. Rev. B **44**, 9338 (1991).

59. C. Daboo, R. J. Hicken, D. E. P. Eley, M. Gester, S. J. Gray, A. J. R. Ives, and J. A. C. Bland, J. Appl. Phys. **75**, 5586 (1994).

60. C. Daboo, R. J. Hicken, E. Gu, M. Gester, S. J. Gray, D. E. P. Eley, E. Ahmad, J. A. C. Bland, R. Ploessl and J. N. Chapman, Phys. Rev. B **51**, 15964 (1995).

61. O. Thomas, Q. Shen, P. Schieffer, N. Tournerie, and B. Lépine, Phys. Rev. Lett. **90**, 17205 (2003).

62. H. B. Zhao, D. Talbayev, Q. G. Yang, G. Lüpke, A. T. Hanbicki, C. H. Li, O. M. J. van 't Erve, G. Kioseoglou, and B. T. Jonker, Appl. Phys. Lett. **86**, 152512 (2005).

63. R. C. O'Handley, *Modern Magnetic Materials: Principles and Applications* (John Wiley & Sons, New York, 1999).

64. R. A. Gordon, E. D. Crozier, D.-T. Jiang, T. L. Monchesky, and B. Heinrich, Phys. Rev. B **62**, 2151 (2000).

65. S. Mirbt, B. Sanyal, C. Isheden, and B. Johansson, Phys. Rev. B **67**, 155421 (2003).

66. Y.Ohno, R. Terauchi, T. Adachi, F. Matsukura, and H. Ohno, Phys. Rev. Lett. **83**, 4196 (1999).

67. R. A. Dragoset, P. N. First, Joseph A. Stroscio, D. T. Pierce, and R. J. Celotta, in *Growth, Characterization and Properties of Ultrathin Magnetic Films and Multilayers*, edited by B. T. Jonker et al., MRS Symposia Proceedings No. 151 (Materials Research Society, Pittsburgh, 1989), p. 193

Reproduced with permission of the copyright owner. Further reproduction prohibited without permission.

68. C. H. Li, G. Kioseoglou, O. M. J. van 't Erve, A. T. Hanbicki, B. T. Jonker, R. Mallory, M. Yasar, and A. Petrou, Appl. Phys. Lett. **85**, 1544 (2004).

69. M. Gester, C. Daboo, R. J. Hicken, S. J. Gray, A. Ercole, and J. A. C Bland, J. Appl. Phys. **80**, 347 (1996).

70. G. A. Prinz, G. T. Rado, and J. J. Krebs, J. Appl. Phys. **53**, 2087 (1982).

71. O. M. J. van 't Erve, G. Kioseoglou, A. T. Hanbicki, C. H. Li, B. T. Jonker, R. Mallory, M. Yasar, and A. Petrou, Appl. Phys. Lett. **84**, 4334 (2004).

72. C. A. F. Vaz, A. Ionescu, T. Trypiniotis, J. A. C. Bland, R. M. Dalgliesh, and S. Langridge, J. Appl. Phys. **97**, 10J119 (2005).

73. C. H. Back, R. Allenspach, W. Weber, S. S. P. Parkin, D. Weller, E. Garwin, and H. C. Siegmann, Science **285**, 864 (1999).

74. E. B. Myers, D. C. Ralph, J. A. Katine, R. N. Louie, and R. A. Buhrman, Science **285**, 867 (1999).

75. I. N. Krivorotov, N. C. Emley, J. C. Sankey, S. I. Kiselev, D. C. Ralph, and R. A. Buhrman, Science **307**, 228 (2005).

76. H. B. Zhao, D. Talbayev, G. Lüpke, A. T. Hanbicki, C. H. Li, M. J. van't Erve, G. Kioseoglou, and B. T. Jonker, Phys. Rev. Lett. **95**, 137202 (2005).

77. G. A. Prinz, Phys. Today **48**, No. 4, 58 (1995).

78. I. Zutic, J. Fabian and S. Das Sarma, Rev. Mod. Phys. **76**, 323 (2004).

79. S. S. P. Parkin, C. Kaiser, A. Panchula, P. M. Rice, B. Hughes, M. Samant, S.-H. Yang, Nature Materials 3, 862 (2004).

80. S. Yuasa, T. Nagahama, A. Fukushima, Y. Suzuki, K. Ando, Nature Materials **3**, 868 (2004).

81. C. Adelmann, X. Lou, J. Strand, C. J. Palmstrøm, and P. A. Crowell, Phys. Rev. B **71**, 121301 (2005).

82. M. van Kampen, C. Jozsa, J. T. Kohlhepp, P. LeClair, L. Lagae, W. J. M. de Jonge, and B. Koopmans, Phys. Rev. Lett. **88**, 227201 (2002).

83. J. S. Claydon, Y. B. Xu, M. Tselepi, J. A. C. Bland, and G. van der Laan, Phys. Rev. Lett. **93**, 037206 (2004).

84. J. Ferré, in *Spin Dynamics in Confined Magnetic Structures I*, Topics Appl. Phys. Vol. **83**, edited by B. Hillebrandt and K. Ounadjela (Springer, Berlin, 2002), pp. 127–165.

Reproduced with permission of the copyright owner. Further reproduction prohibited without permission.

85. I. Bozovic, M. Schneider, Y. Xu, Roman Sobolewski, Y. H. Ren, G. Lüpke, J. Demsar, A. Taylor, and M. Onellion, Phys. Rev. B **69**, 132503 (2004).

86. M. Madami, S. Tacchi, G. Carlotti, G. Gubbiotti, R. L. Stamps, Phys. Rev. B **69**, 144408 (2004).

87. P. Grünberg, M. G. Cottam, W. Vach, C. Mayr, R. E. Camley, J. Appl. Phys. **53**, 2078 (1982).

88. R. D. McMichael, M. D. Stiles, P. J. Chen, and W. F. Egelhoff, Jr. J. Appl. Phys. **83**, 7037 (1998).

89. T. J. Silva, C. S. Lee, T. M. Crawford, and C. T. Rogers, J. Appl. Phys. **85**, 7849 (1999).

90. G. T. Rado, and J. R. Weertman, J. Phys. Chem. Solids **11**, 315 (1959).

91. C. Vittoria, J. J. Krebs, and G. A. Prinz, J. Magn. Magn. Mat. **37**, L111 (1983).

92. C. Vittoria, F. J. Rachford, J. J. Krebs, and G. A. Prinz, Phys. Rev. B **30**, 3903 (1984).

93. M. Grimsditch, Eric E. Fullerton, and R. L. Stamps, Phys. Rev. B **56**, 2617 (1997).

94. M. Sparks, Phys. Rev. B **1**, 3831 (1979).

95. J.-H. Park, E. Vescovo, H.-J. Kim, C. Kwon, R. Ramesh, and T. Venkatesan, Nature **392**, 794 (1998).

96. Moon-Ho Jo, N.D. Mathur, J.E. Evetts, and M.G. Blamire, Appl. Phys. Lett. **77**, 3803 (2000).

97. M. Bowen, M. Bibes, A. Barthelemy, J.-P. Contour, A. Anana, Y. Lemaitre, and A. Fert, Appl. Phys. Lett. **82**, 233 (2003).

98. V. Garcia, M. Bibes, A. Barthelemy, M. Bowen, E. Jacquet, J.-P. Contour, and A. Fert, Phys. Rev. B **69**, 52403 (2004).

99. V. Dedui, M. Murgia, F. C. Matacotta, C. Taliani, and S. Barbanera, Solid State Comm. **122**, 181 (2002)

100. T. Ono, A. Kogusu, S. Morimoto, S. Nasu, A. Masuno, T. Terashima, and M. Takano, Appl. Phys. Lett. **84**, 2370 (2004).

101. C. Zener, Phys. Rev. **82** 403 (1951).

Reproduced with permission of the copyright owner. Further reproduction prohibited without permission.

102. V. Dyakonov, V. Shapovalov, E. Zubov, P. Aleshkevych, A. Klimov, V. Varyukhin, V. Pashchenko, V. Kamenev, V. Mikhailov, K. Dyakonov, V. Popov, S. J. Lewandowski, M. Berkowski, R. Zuberek, A. Szewczyk, and H. Szymczak, J. Appl. Phys. **93**, 2100 (2003).

103. R. Shreekala, M. Rajeswari, S. P. Pai, S. E. Lofland, V. Smolyaninova, K. Ghosh, S. B. Ogale, S. M. Bhagat, M. J. Downes, R. L. Greene, R. Ramesh, and T. Venkatesan, Appl. Phys. Lett. **74**, 2857 (1999).

104. D. L. Lyfar, S. M. Ryabchenko, V. N. Krivoruchko, S. I. Khartsev, and A. M. Grishin, Phys. Rev. B **69**, 100409(R) (2004).

105. S. E. Lofland, S. M. Bhagat, H. L. Ju, G. C. Xiong, T. Venkatesan, and R. L. Greene, Phys. Rev. B **52**, 15058 (1995).

106. S. E. Lofland, S. M. Bhagat, C. Kwon, M. C. Robson, R. P. Sharma, R. Ramesh, and T. Venkatesan, Phys. Lett. A **209**, 246 (1995).

107. A.I. Shames, E. Rozenberg, G. Gorodetsky, A.A. Arsenov, D. A. Shulyatev, Ya. M. Mukovskii, A. Gedanken, and G. Pang, J. Appl. Phys. **91**, 7929 (2002).

108. Y. G. Zhao, J. J. Li, R. Shreekala, H. D. Drew, C. L. Chen, W. L. Cao, C. H. Lee, M. Rajeswari, S. B. Ogale, R. Ramesh, G. Baskaran, and T. Venkatesan, Phys. Rev. Lett. **81**, 1310 (1998).

109. K. Matsuda, A. Machida, Y. Moritomo, and A. Nakamura, Phys. Rev. B **58**, R4203 (1998).

110. A. I. Lobad, R. D. Averitt, C. Kwon, and A. J. Taylor, Appl. Phys. Lett. **77**, 4025 (2000).

111. A. I. Lobad, R. D. Averitt, and A. J. Taylor, Phys. Rev. B **63**, 060410(R) (2001).

112. R. D. Averitt, A. I. Lobad, C. Kwon, S. A. Trugman, V. K. Thorsmølle, and A. J. Taylor, Phys. Rev. Lett. **87**, 17401 (2001).

113. Y. H. Ren, H. B. Zhao, G. Lüpke, Y. F. Hu, and Qi Li, J. Appl. Phys. **91**, 7514 (2002).

114. T. Ogasawara, M. Matsubara, Y. Tomioka, M. Kuwata-Gonokami, H. Okamoto, and Y. Tokura, Phys. Rev. B **68**, 180407(R) (2003).

115. S. A. McGill, R. I. Miller, O. N. Torrens, A. Mamchik, I-Wei Chen, and J. M. Kikkawa, Phys. Rev. Lett. **93**, 47402 (2004).

116. S. A. McGill, R.I. Miller, O. N. Torrens, A. Mamchik, I-Wei Chen, and J.M. Kikkawa, Phys. Rev. B **71**, 75117 (2005).

Reproduced with permission of the copyright owner. Further reproduction prohibited without permission.

117. G. Ju, A.V. Nurmikko, R. F. C. Farrow, R. F. Marks, M.J. Carey, and B.A. Gurney, Phys. Rev. Lett. **82**, 3705 (1999).

118. B. Koopmans, M. van Kampen, J. T. Kohlhepp, and W.J.M. de Jonge, Phys. Rev. Lett. **85**, 844 (2000).

119. Q. Zhang, A. V. Nurmikko, A. Anguelouch, G. Xiao, and A. Gupta, Phys. Rev. Lett. **89**, 177402 (2002).

120. Y. Suzuki, H. Y. Hwang, S-W. Cheong, and R. B. van Dover, Appl. Phys. Let. **71**, 140 (1997).

121. K. Steenbeck and R. Hiergeist, Appl. Phys. Let. **75**, 1778 (1999).

122. J. O'Donnel, M. S. Rzhowski, J. N. Eckstein, and I. Bozovic, Appl. Phys. Let. **72**, 1775 (1998).

123. L. Ranno, A. Llobet, R. Tiron, and E. Favre-Nicolin, Appl. Surf. Sci. **188**, 170 (2002).

124. C. M. Xiong, J. R. Sun, and B. G. Shen, Silid State Comm. **134**, 465 (2005).

125. C. Kwon, M. C. Robson, J. Y. Gu, S. E. Lofland, S. M. Bhagat, Z. Trajanovic, M. Rajeswari, T. Venkatesan, A. R. Kratz, R. D. Gomez, and R. Ramesh, J. Magn. Magn. Mater. **172**, 229 (1997).

126. H. S. Wang, Q. Li, K. Lui, and C. L. Chien, Appl. Phys. Lett. **74**, 2212 (1999).

127. H.S. Wang, and Qi Li, Appl. Phys. Lett. **73**, 2360 (1998).

128. H.S. Wang, E. Wertz, Y.F. Hu, and Qi Li, J. Appl. Phys. **87**, 7409 (2000).

129. B. Vengalis, A. Maneikis, F. Anisimovas, R. Butkute, L. Dapkus, and A. Kindurys, J. Magn. Magn. Mat. **211**, 35 (2000).

130. S. Zoll, H.A.M. Van den Berg, K. Ounadjela, D. Stoeffler, and A. Dinia, J. Appl. Phys. **79**, 2601 (1996).

131. N.D. Mathur, M.-H. Jo, J.E. Evetts, and M.G. Blamire, J. Appl. Phys. **89**, 3388 (2001).

132. M. Sasaura, S. Miyazawa, and M. Mukaida, J. Appl. Phys. **68**, 3643 (1990).

133. M.L. Sanjuan, V.M. Orera, R.I. Merino, and J. Blasco, J. Phys.: Cond. Mat. **10**, 11687 (1998).

134. D. Talbayev, H. Zhao, G. Lüpke, J. Chen, and Qi Li, Appl. Phys. Lett. 86, 182501 (2005).

Reproduced with permission of the copyright owner. Further reproduction prohibited without permission.

135. D. L. Lyfar, S. M. Ryabchenko, V. N. Krivoruchko, S. I. Khartsev, and A. M. Grishin, Phys. Rev. B **69**, 100409 (2004).

136. M. C. Martin, G. Shirane, Y. Endoh, K. Hirota, Y. Moritomo, and Y. Tokura, Phys. Rev. B **53**, 14285 (1996).

137. G. Feher, E. A. Gere, Phys. Rev. **114**, 1245 (1959).

138. B. Beschoten, E. Johnston-Halperin, D. K. Young, M. Poggio, J. E. Grimaldi, S. Keller, S. P. DenBaars, U. K. Mishra, E. L. Hu, and D. D. Awschalom, Phys. Rev. B, **63**, 121202(R) (2001).

139. Y. D. Park, A. T. Hanbicki, J. E. Mattson, and B. T. Jonker, Appl. Phys. Lett. **81**, 1471 (2002).

140. P. K. Baltzer, H. W. Lehmann, and M. Robbins, Phys. Rew. Lett. **15**, 493 (1965).

141. G. Margaritondo, J. T. McKinley, D. Rioux, and D. W. Niles, Appl. Surf. Sci. **56–58**, 713 (1992).

142. H. K. Yow, P. A. Houston, and M. Hopkinson, Appl. Phys. Lett. **66**, 2852 (1995).

143. M. Dahmen, U. Rau, M. Kawanaka, J. Sone, and J. H.Werner, Appl. Phys. Lett. **62**, 261 (1993).

144. D. K. Schröder, *Semiconductor Material and Device Characterization* (Wiley, New York, 1998), pp. 171–177

145. K. Nishi, H. Ohyama, T. Suzuki, T. Mitsuyu, and T. Tomimasu, Appl. Phys. Lett. **70**, 3585, (1997).

146. J. T. McKinley, R. G. Albridge, A. V. Barnes, A. Ueda, N. H. Tolk, C. Coluzza, F. Gozzo, G. Margaritondo, D. Martin, F. Morier-Genoud, C. Dupuy, A. Rudra, and M. Ilegems, J. Vac. Sci. Technol. B **11**, 1614 (1993).

147. George Kioseoglou, Aubrey T. Hanbicki, James M. Sullivan, Olaf M. J. van 't Erve, Connie H. Li, Steven C. Erwin, Robert Mallory, Mesut Yasar, Athos Petrou, Berend T. Jonker, Nature Materials **3**, 799 (2004).

148. G. Harbeke, and H. Pinch, Phys. Rev. Lett. **17**, 1090 (1966).

149. Alessandra. Continenza, Teresa de Pascale, Franco Meloni, and Marina Serra, Phys. Rev. B **49**, 2503 (1994).

150. I. Balberg and A. Maman, Phys. Rev. B **16**, 4535 (1977).

151. L. L. Golik, Z. E. Kun'kova, and C. Heide, J. Appl. Phys. **87**, 6472 (2000).

Reproduced with permission of the copyright owner. Further reproduction prohibited without permission.

VITA

Haibin Zhao

Haibin Zhao was born in Shaoxing, China on December 5, 1974. Haibin Zhao received his B.A. in Physics at Fudan University in 1997. He received his M.S. degree at Fudan University in 2000, with a concentration in Condensed Matter Physics.

In August 2000, the author entered the College of William and Mary as a research assistant in the Department of Applied Science. With the completion of the thesis and satisfaction in all other degree requirements, the author received his Ph. D degree in Applied Physics in February 2006.

Reproduced with permission of the copyright owner. Further reproduction prohibited without permission.